THE UNIVERSITY OF MICHIGAN
COLLEGE OF ENGINEERING
Department of Aerospace Engineering

Interim Technical Report

AN EXPERIMENTAL INVESTIGATION OF THE UNSTEADY FLOWS ABOUT SPHERES AND DISKS

Frederick W. Roos
William W. Willmarth

ORA Project 01954

DEPARTMENT OF THE ARMY
U. S. ARMY RESEARCH OFFICE—DURHAM
GRANT NO. DA-ARO-D-31-124-G711, PROJECT NO. 5590-E
DURHAM, NORTH CAROLINA

administered through:

OFFICE OF RESEARCH ADMINISTRATION   ANN ARBOR

December 1968

This report was also a dissertation submitted by the first author in partial fulfillment of the requirements for the degree of Doctor of Philosophy in The University of Michigan, 1968.

TABLE OF CONTENTS

Page

LIST OF FIGURES

NOMENCLATURE

a_{max}	maximum value of unsteady acceleration, ft/sec^2
a	acceleration, ft/sec^2
A	acceleration modulus, $A = ad/U^2$
C_D	drag force coefficient, $C_D = D/(\pi/8)\rho U^2 d^2$
$C_{F_{PP}}$	peak-to-peak coefficient of total transverse force, $C_{F_{PP}} = F_{PP}/(\pi/8)\rho U^2 d^2$
C_L	lift force coefficient, $C_L = L/(\pi/8)\rho U^2 d^2$
$\overline{C}_L$	mean value of C_L
$\sqrt{\overline{C_L^2}}$	root-mean-square value of C_L
$C_{M_{PP}}$	peak-to-peak coefficient of total moment, $C_{M_{PP}} = M_{PP}/(\pi/8)\rho U^2 d^3$
C'_M	coefficient of disk moment about fixed axis in wind tunnel tests, $C'_M = M'/(\pi/8)\rho U^2 d^3$
$\sqrt{\overline{C'^2_M}}$	root-mean-square value of C'_M
d	sphere or disk diameter, ft
D	drag force, lb
f	frequency of force or moment fluctuation, Hz
f^*	dimensionless frequency, $f^* = fd/U$
F	total transverse force, lb
F_{PP}	peak-to-peak magnitude of unsteady total transverse force, lb
I^*	dimensionless moment of inertia of disk $I^* = \pi \rho_d \tau/64\rho d$

ℓ	characteristic dimension of arbitrary flow, ft
L	lift force, lb
m	mass of sphere or disk, sl
m_a	apparent mass, sl
M	total moment on disk, ft-lb
M'	moment on disk about fixed axis in wind tunnel tests, ft-lb
n	oscillation frequency of freely falling disk, Hz
P	pitching moment, ft-lb
R	force resisting acceleration, lb
Re	Reynolds number for arbitrary flow, $Re = U\ell/\nu$
Re_d	Reynolds number based on sphere or disk diameter, $Re_d = Ud/\nu$
$Re_{d_{min}}$	minimum Reynolds number for wake fluctuations
S	side force, lb
t	time, sec
T	fluid temperature, ^{o}C
U	steady relative velocity between fluid and sphere or disk, ft/sec
x	distance along track, ft
Y	yawing moment, ft-lb
Γ	unsteady circulation about sphere
λ	wavelength of periodic sphere or disk motion, ft

μ	fluid viscosity, sl/ft-sec
ν	kinematic viscosity of fluid, ft^2/sec
ρ	fluid density, sl/ft^3
ρ_d	uniform density of freely falling disk, sl/ft^3
τ	disk thickness, ft

ABSTRACT

Several recent aerodynamic problems, e.g., the use of freely-rising balloons to measure atmospheric wind profiles and the unsteady cross-axis loads acting on tall launch vehicles, have prompted renewed interest in unsteady separated flows over bluff bodies. The quantitative features of three-dimensional bluff body flow fields are quite well known, however, very little quantitative data exists describing the unsteady loads and nothing is known concerning the relationship of the flow field geometries to the unsteady loads.

An experimental program was undertaken to provide some of this information. A large part of the research effort was spent in the development of a towing channel facility equipped with an air bearing supported model carriage suitable for making measurements in glycerol-water mixtures of the unsteady drag and pitching moment on a circular disk and the unsteady drag and side force on a sphere. The measurements were made with strain gage balances over a wide Reynolds number range ($5 < Re_d < 120{,}000$). The hydrogen bubble flow visualization method was adapted to these glycerol-water mixtures to permit correlation of wake configurations with the unsteady loads.

Steady drag coefficients for the sphere and disk agreed with existing data except for the disk in the range $100 < Re_d < 1000$, where the experimental C_D was as much as 50% lower than previous results. Drag force unsteadiness during steady motion was always < 5% for the sphere and < 3% for the disk.

Sphere drag measurements under constant acceleration from rest proved the apparent mass concept to be valid at high Re_d until the sphere had travelled approximately one diameter.

Nondimensional frequencies of disk pitch and yaw were in the range 0.10-0.14 for $100 < Re_d < 500$. Although previous data indicates that vortex shedding normally begins at $Re_d \approx 100$, the sting support in these tests stabilized the wake to the extent that shedding did not occur for $Re_d < 160$. Peak-to-peak moment coefficients were found to be of the order of .007 over this Re_d range.

It was learned that reliable unsteady force data cannot be obtained with a sting supported sphere because the delicate vortex shedding process is seriously disturbed by the sting, however, based on the data gathered, an order of magnitude estimate of the peak-to-peak unsteady force coefficient is 0.02-0.10 for $270 < Re_d < 560$.

Flow visualization studies revealed that the unsteady transverse force on a sphere can be related to the concept that unsteady bound vorticity exists about the body in connection with the vortex-shedding process while the un-

steady moment on a disk results from the upstream flow in the wake being deflected when vortices are shed.

I. INTRODUCTION

Bodies as geometrically simple as the sphere and the circular disk can exhibit exceedingly complex aerodynamic characteristics. Anyone who has observed the tumbling fall of a coin through water or the swerving flight of a tennis ball can attest to this fact. The unsteady motion of such objects results from the fact that they are aerodynamically bluff bodies.

The characteristic feature of bluff body flows is the separation of the flow from the surface of the body. A shear layer exists between the main flow past the body and the "dead fluid" in the space behind the body. Instability of this shear layer produces fluctuations in the pressure and shear stress distributions over the surface of the body. The resultant unsteady forces on the body cause it to move erratically. The situation is further complicated by the fact that the erratic motion of the body alters the flow field; hence a complex interaction of body and fluid dynamics occurs.

The existence of this unsteady behavior has long been known. However, the mathematics of the problem are so difficult that prediction of the unsteady motions is impossible. In fact, the much simpler problem of steady separated flow about a body has yet to be solved analytically. Consequently, insight into the nature of bluff body flows must be obtained through experimentation.

This paper describes an experimental investigation of the unsteady aerodynamics of spheres and disks which was conducted in the Gas Dynamics Laboratories of the University of Michigan.

The remainder of Section I contains a discussion of the past and current interest in sphere and disk flows. An outline of the research program concludes this Section.

A study of the existing literature on sphere and disk aerodynamics revealed that the general features of sphere and disk flows are quite well understood, but very little quantitative work has been done on the unsteady flow problems. The available information on sphere and disk flows that is pertinent to the present study is presented in Section II.

Section III consists of a detailed description of the equipment used in obtaining the experimental measurements. The factors influencing the design of the experiment are also noted.

The experimental results obtained in this investigation are presented in Section IV. Significant features of these results are discussed; where possible, the measurements are compared with existing published data.

Finally, the conclusions that can be drawn from the results of this research are given in Section V.

A. INTEREST IN SPHERE AND DISK AERODYNAMICS

Interest in the behavior of a sphere or disk moving relative to a fluid goes back many years. In fact, the first recorded sphere drag measurements were published by Sir Isaac Newton, who determined the times of fall of spheres descending in columns of water and later timed the fall of various spheres dropped from the dome of St. Paul's Cathedral in London[1, pp. 353-366]. Since then, a multitude of studies of the aerodynamics of spheres and disks has been undertaken. Many of these have been noted by Torobin and Gauvin[2-7] in their comprehensive review of the sphere problem.

The first such investigations were prompted primarily by curiosity regarding the nature of fluids and their behavior in the presence of solid bodies. Nevertheless, there were applications for the results of such studies. For example, artillery officers were interested in the behavior of spheres moving through air in order to predict the ballistics of their cannon balls. Also, the rate of fall of a small sphere provided a convenient measurement of the viscosity of a fluid once the limits of validity of Stokes'[8] sphere drag relation,

$$D = 3\pi d \mu U$$

had been established.

Academic interest in the fundamental characteristics of body-fluid interactions is as keen as ever; moreover, engineering situations abound today in which the nature of the flow of a fluid past a sphere or disk is significant. In fact, in the past ten years or so, several important new sphere and disk flow problems have arisen.

One of these problems, that of rocket motor performance losses resulting from the entrainment of solid and liquid particles in the exhaust gases, was reviewed recently by Hoglund[9]. These entrained particles are composed chiefly of metal oxides and, therefore, are much more dense than the surrounding gas. As a result, they lag behind the exhaust gas as the gas-particle mixture accelerates through the rocket nozzle. The resultant relative flow of the gas past the particles contains a momentum-loss mechanism in that the drag of the particles absorbs momentum from the gas; this mechanism can often produce losses of rocket motor specific impulse greater than 10%. The significance of this problem is that the metallic oxide particles result from the burning of metals which are incorporated into rocket fuels for their potential ability to increase specific impulse. As Hogland noted, attempts to calculate these losses have been severely limited by a lack of knowledge of particle drag in the presence of acceleration and high-intensity turbulence effects.

Another important sphere-flow problem exists in the meteorological use of freely rising balloons to measure the vertical profile of the horizontal component of the atmospheric wind. Although spherical balloons have been employed in this manner for many years, Scoggins [10] points out that most of the data so obtained are averaged over at least 600 meters altitude. However, with the advent of large ballistic missiles and launch vehicles which must rise vertically through the atmosphere, much more detailed measurements of wind profiles are needed.

A system to provide these measurements was devised wherein a precision radar was used to track a superpressure constant volume Mylar sphere rising through the atmosphere at a rate of about 25 feet per second. Careful analysis of the high-resolution profiles obtained with this system revealed small scale features that were not truly representative of atmospheric winds. Further tests led Scoggins to conclude that "spherical balloons do not rise vertically in a calm atmosphere." The small-scale horizontal balloon motions were found to be caused by the aerodynamics of the balloon itself. These balloons typically operated in the critical range of Reynolds numbers, 50, 000 to 800, 000 [11]; the significance of this point will be made apparent below. Becuase of the discovery of these aerodynamically-induced balloon oscillations, the past few years have seen considerable effort put into the study of unsteady sphere aerodynamics[11-15] and attempts to minimize the spurious balloon motions. [10, 11, 13, 14, 16]

Still another need for knowledge of the behavior of spherical particles in a fluid exists in many areas within the chemical industry.

In the first article of their series, Torobin and Gauvin[2] note many processes wherein relative motion between particles and a fluid plays an important part: evaporation, drying, crop-spraying, and fluidized-bed reactions, to name but a few.

Although the flow field about a disk has not received the great attention given to the sphere flow field, nevertheless, there do exist some situations where such flows are important. A common example is the ubiquitous post-mounted traffic sign, which can oscillate violently, even to destruction, in a strong wind. This oscillation is due simply to the vortex-shedding which occurs in the wake of the sign. Willmarth, Hawk, Galloway, and Roos[17] recently investigated this phenomenon.

Another reason for studying the aerodynamics of a circular disk is that the disk flow field provides a valuable comparison for the sphere flow, particularly in the case where the respective bodies are rigidly fixed. Several features are common to both bodies, notably axial symmetry and the occurrence of a large region of separated flow. However, one significant difference between the two exists. The flow separation line is free to shift about on the sphere, since the surface curvature is uniform. On the other hand, the disk geometry is such that separation always occurs at the rim.

B. THE RESEARCH PROGRAM

The principal goals set for this research program were the quantitative analysis of the unsteady forces and moments acting on a translating sphere or circular disk, and the elucidation of the manner in which the fluctuation of the separated flow produces these loads. To eliminate the coupling between body dynamics and flow unsteadiness, the sphere and disk were constrained to move in a straight line, without rotation.

Two categories of unsteady flows were investigated. In one, the velocity of the body relative to the fluid was held constant while the unsteady forces superimposed on the steady drag were studied. In the other, the velocity of the body was varied, i. e., the motion involved acceleration effects.

The research effort was focused on the range of Re_d from 100 to 10,000. This range was selected because it encompasses a wide variety of wake types, from the steady laminar wake to the fully turbulent wake.

The delimitation of the research was completed with the decision that the influence of such variables as compressibility, free stream turbulence level, and surface roughness would not be studied.

II. EXISTING KNOWLEDGE OF SPHERE AND DISK AERODYNAMICS

A. INTRODUCTION

The characteristics of the flow of an unbounded, viscous, incompressible, turbulence free fluid about a smooth, rigid sphere or disk are summarized in this Section. With this set of restrictions, the flow field depends primarily on the Reynolds number Re_d. Consequently the discussion in this chapter will focus on the variation with Re_d of the characteristic features of sphere and disk flows. The influence of other parameters, e. g., acceleration, will also be discussed.

Most of the experimental results noted here contain one of two flaws. Wind tunnel and towing channel tests suffer from flow interference produced by the structure used to support the sphere or disk. On the other hand, experiments with freely rising or falling bodies often involve relatively short trajectories, which preclude the study of long wavelength fluctuations and, in some cases, even prevent full development of the flow field. In addition, the coupling between body and wake motions during free flight tests does not permit the study of flow instability alone. This is particularly important in the case of the disk, as will be noted below.

Hopefully, the advent of magnetic wind tunnel model suspensions will eventually lead to interference-free studies of the flow about a rigidly held sphere. The same does not appear to be possible with a disk, as the disk geometry precludes incorporation of a magnetic dipole aligned with the disk axis. Since such a dipole is a necessary part of a magnetic suspension system, there seems to be no way to magnetically support a disk without significantly altering its shape.

One further point should be mentioned. Because the experimental results included in the following discussion have been obtained with myriad different test setups and conditions, the Re_d ranges specified and even some of the details of the various flow phenomena may not be completely accurate.

B. AERODYNAMICS OF A SPHERE

1. Flow Regimes

As Re_d is varied, the flow about a sphere passes through a wide variety of configurations. In the following outline, an attempt has been made to piece together a coherent picture of the development of the sphere flow field with increasing Re_d from the results of many experimental investigations.

a. $0 < Re_d < 0.1$: In this regime, the flow in the vicinity of a sphere is completely dominated by viscous effects. Streamlines near the sphere are essentially symmetrical fore and aft of the sphere (Fig. 1). However, this symmetry can not exist far from the sphere. As Lamb[18, pp. 608-614] shows, the ratio of inertial forces to viscous forces in the sphere flow field is of the order of Ur/ν, where r is the distance from the center of the sphere. Thus, no matter how great the ratio of ν to U may be, inertial forces will become dominant at very large r.

b. $\underline{0.1 < Re_d < 24}$: The flow in this range of Re_d is still dominated by viscous effects, but fluid inertia exerts an increasing influence. The streamline pattern near the sphere is no longer symmetrical fore and aft. As indicated in Fig. 2, comparison of streamlines equal distances upstream and downstream of the sphere discloses that the point of maximum transverse deflection of a streamline shifts downstream from the equatorial plane of the sphere, the magnitude of the shift increasing for streamlines farther from the stagnation streamline. The flow pattern in Fig. 2, it should be noted, is taken from the numerical solution by Jenson[19] for this flow regime. His results, although obtained for a confined flow*, are qualitatively similar to observed flows with boundaries far removed from the sphere.

---

*Jenson assumed that the flow was contained in a cylindrical stream tube of diameter equal to six sphere diameters.

c. $\underline{24 < Re_d < 130}$: At $Re_d \approx 24$, a closed region of separated flow appears at the rear stagnation point[20]. Primarily because of the difficulty in observing the onset of separation, considerable disagreement exists as to the value of Re_d at which this occurs. However, the value noted above is thought to be very close. As is pointed out in most textbooks on fluid mechanics, Schlichting[21, pp. 27-29] for example, the separation is caused by the inability of the fluid adjacent to the surface to work against an adverse pressure gradient all the way to the rear stagnation point owing to loss of momentum through surface friction. As Re_d increases in this range, the separation circle moves upstream and an annular vortex forms within the separation bubble; this is indicated in Fig. 3.

d. $\underline{130 < Re_d < 210}$: As Re_d increases above 130, the separation bubble continues to grow, but now the downstream end of the bubble pulsates faintly with a very low frequency[20]. This pulsation becomes more conspicuous as Re_d increases, but the laminar wake downstream of the wake stagnation point remains stable.

e. $\underline{210 < Re_d < 270}$: For Re_d in this range, Magarvey and Bishop[22] noted a double laminar wake indicated by two parallel dye threads combined with an asymmetrical separation bubble. Because they were studying wakes produced by a liquid drop falling through an immiscible field liquid, it is not certain that this phenomenon occurs in the case of a rigid sphere. However, it seems reasonable to expect that the same flow would occur for a solid sphere. This expectation was verified in this laboratory by Hawk[23], who observed a twin wake behind a dyed steel sphere falling in water at $Re_d \approx 250$.

According to Magarvey and MacLatchy[24], this twin-wake situation arises when the rate of vorticity production in the sphere boundary layer can not quite be balanced sufficiently by diffusion and convection into the single laminar wake. Hence the separation bubble grows with accumulated vorticity until it becomes unstable. When this happens, the vortex ring within the bubble becomes distorted and eventually a segment of it becomes pulled out behind the sphere by the flowing fluid (see sequence sketched in Fig. 4). Once this occurs, the pair of stretched vortex filaments linking the discharged loop with the portion of the ring remaining in the separation bubble provide a mechanism for discharging additional vorticity into the wake. Apparently this mechanism carries away sufficient vorticity for the configuration to remain stable until Re_d approaches 270. It would be expected that the asymmetry associated with this wake arrangement should produce a transverse force on the sphere; Magarvey and Bishop[22] did, in fact, observe that the sphere followed an inclined path, indicating the action of a transverse force.

f. <u>$270 < Re_d < 290$:</u> Once Re_d reaches approximately 270, the twin vortex mechanism is no longer capable of discharging enough vorticity to maintain equilibrium and waves begin to appear in the wake [22]. These undulations amount to slight additional discharges of vorticity.

g. $\underline{290 < Re_d < 700}$: The undulations which occur for Re_d just below 290 become discrete vortex loops in this Re_d range. These loops are shed from opposite sides of the separation bubble with a definite periodicity[22, 25]. As Re_d increases in this range, the discharge of vortex loops becomes more random. The flow is sketched in Fig. 5.

h. $\underline{700 < Re_d < 10,000 \text{ (est.)}}$: With Re_d above 700, the vortex loops, which have become quite random in size and orientation, are discharged with increasing frequency[22]. Above $Re_d \approx 1500$, the shed vortex loops tend to cluster in clumps or "vortex balls" as Möller [26] termed them. Measurements by Cometta[27] in this Re_d range also seem to show these vortex clumps. Hot wire investigations of sphere wakes in this range of Re_d by Kendall[28] and wind tunnel flow observations by Winny[29] appear to indicate that an overall helical pattern exists in the wake, possibly produced by a progression about the wake axis of the location of the clustering vortex balls. Photographs by Möller[26] and Schmiedel[30] also seem to show a helical wake configuration. This helical wake, if it does exist, may well occur far into the next Re_d range.

In the course of his hot wire experiments, Kendall[28] noted that the free shear layer of the separated flow near the sphere surface oscillated with a frequency apparently unrelated to the frequency of the wake helix. In the range $3000 < Re_d < 10,000$, he found that the shear layer frequency scaled with U^2, whereas the frequency in the helical wake was 0.18U/d (for $Re_d > 400$).

Winny[29] also reported hot wire measurements, noting a periodicity in the sphere wake at an average frequency of 0.24U/d for $Re_d = 47,000$. In addition, he measured unsteady surface pressure at various points around the sphere. At $Re_d = 130,000$, he found that pressure impulses occurred near the separation point with two frequencies. The overall frequency of these pulses was 0.91U/d, but on the average, every fifth pulse was much larger, giving a frequency of approximately 0.20U/d for the large impulses.

The above indicates that there are two types of instability in the sphere wake. One of these leads to the overall spiraling motion of the wake. The other is a higher-frequency local rolling up of the separated shear layer into vortices. In this connection, a most interesting discussion of similar processes occurring in the wake of a cylinder was recently given by Morkovin[31].

i. <u>$10,000 < Re_d < 200,000$:</u> In this range the vortex loop shedding becomes so rapid that it is nearly a continuous process and the sphere wake takes on a turbulent appearance. The separation circle continues to move upstream on the sphere as Re_d increases, approaching a point about 80^o from the front stagnation point[32]. Fluctuation of the wake exists throughout this regime, corresponding to the shedding of vorticity clumps.

j. $\underline{200,000 < Re_d < 400,000}$: This is the Re_d range commonly termed the "critical range". At $Re_d \approx 200,000$, the sphere boundary layer begins to undergo natural transition from laminar to turbulent flow before separation. When this occurs, the enhanced mixing of the turbulent boundary layer adds momentum to the fluid layer adjacent to the sphere surface and thereby permits it to proceed farther against the adverse pressure gradient than could the laminar layer. This delay of separation significantly reduces pressure drag and is responsible for the well-known dip in the sphere C_D versus Re_d curve. In fact, over a portion of this Re_d range not only C_D but the drag itself decreases with increasing Re_d.

In this critical range of Re_d, the transition process is neither uniform nor steady, with the result that large changes can occur in the position of separation. Since the separation can shift up- and downstream at any given point around the sphere, significant random fluctuations of the wake occur. Because the boundary layer transition process is highly sensitive to sphere surface condition and steadiness of the free stream, the actual range of Re_d for transition varies widely in different situations. For comparison, flow configurations before and after transition are sketched in Fig. 6.

k. $\underline{Re_d > 400,000}$: When Re_d has reached 400,000, the transition process is well established and has begun to move forward in the sphere boundary layer. The consequent thickening of the turbulent portion of the layer causes the separation circle to begin shifting upstream again, gradually increasing the pressure drag as Re_d increases.

Because boundary layer transition is a result of flow instability, it is highly sensitive to many factors, e. g., surface imperfections and unsteadiness of the pressure field about the sphere. As a result, the flow separation line and the wake at supercritical Re_d continue to fluctuate strongly, especially at very low frequencies[33]. These fluctuations are particularly pronounced with freely moving spheres such as balloons, which generally have surface irregularities, owing to the ease with which the low-mass balloon can rotate and move transversely in response to unsteady forces.

2. Steady Drag

Many investigators have used a wide variety of techniques to measure the aerodynamic drag on a sphere and its dependence on Re_d, surface roughness, and free stream turbulence. Consequently, a great deal of data on sphere drag has accumulated. In spite of all this effort, however, the relationship between sphere C_D and Re_d is not very accurately known, as can be seen in Fig. 7, which is a plot of selected representative sphere drag data for steady sphere motion.

The scatter in this C_D versus Re_d data is believed to arise from five principal causes. Perhaps the most significant of these is the difficulty in accurately determining the kinematic viscosity ν and temperature T of a fluid. This is especially important in much of the sphere drag data because many of the experiments were performed early in this century, when viscosity and temperature measurement techniques were not nearly as precise as those used today.

Because most of the low Re_d data was obtained with very small spheres, problems involved in measuring and weighing these small particles are believed to be partly responsible for the variation in the C_D versus Re_d data at low Re_d.

Another problem involved in many of the low Re_d experiments was the inability to accurately account for the effect produced by the walls of the fluid container. Several correction factors had been proposed*, but no means existed for determining a priori which, if any,

---

*A brief discussion of these correction factors is given in reference 34.

was appropriate. The dilemma arose, of course, from the fact that all the corrections were based on approximate solutions of the flow equations. The recent experimental work of Maxworthy[35] has shed some important light on this problem; his results indicate that, as one might expect, none of the theoretical wall-correction factors is correct.

A fourth source of scatter in the drag data is the unsteadiness in the sphere flow field for Re_d above a few hundred. Since almost all the available data for Re_d below approximately 100,000 was obtained from tests of freely falling or rising spheres, this data suffers from the fact that the spheres were able to deviate from a straight vertical path when the wake fluctuated. The path fluctuations tend to depend on the ratio of sphere density to fluid density and, as noted above, are fairly random.

The shape of the C_D - Re_d curve in the critical range of Re_d has been studied by many investigators. Because of the sensitivity of the sphere flow field to many factors in this transition regime, as described above, there have resulted almost as many different drag coefficient curves as there have been experiments.

In the remainder of this section, the characteristics of the C_D - Re_d curve will be discussed. In addition, brief mention will be made of the various experiments which provided the data given in Fig. 7.

a. $0 < Re_d < 0.1$: For Re_d below 0.1, the C_D - Re_d relationship is in very close agreement with the prediction of Stokes' Drag Law, which is, in coefficient form,

$$C_D = \frac{24}{Re_d}.$$

Stokes obtained his result by omitting the inertia terms from the Navier-Stokes equation and solving the resultant linear differential equation[8]. As was noted in the above discussion of the sphere flow field, Stokes' calculation is incorrect far from the sphere. However, the close agreement of his expression for sphere drag with the experimental results indicates that the flow far from the sphere has negligible influence on the drag in this Re_d regime.

The flow near the sphere is dominated by pressure and viscous forces; 2/3 of the drag calculated by Stokes is caused by skin friction, the remaining 1/3 of the sphere drag resulting from the distribution of pressure about the sphere.

The data plotted in this range comes from experiments by Arnold [36], who dropped rose metal spheres in a cylindrical tube filled with colza oil, and Möller[26], who used steel spheres in glycerol. The results of Möller are believed to be more reliable, primarily because of the smaller sphere diameter to tube diameter ratio in his experiments.

b. $0.1 < Re_d < 1$: As Re_d increases above 0.1, C_D becomes increasingly greater than the value predicted by Stokes' Law. This is, of course, caused by the fact that the contribution of pressure to the sphere drag is increasing because of the rising influence of fluid inertia, which Stokes omitted in his calculation. This behavior is also indicated by the streamline asymmetry mentioned above and shown in Fig. 2. Further, the skin friction itself becomes greater than Stokes' value owing to the increasing tendency, as Re_d increases, of the vorticity to be concentrated in a thin boundary layer.

Drag data in this range agrees satisfactorily with the theoretical expression obtained by Oseen[37], which is expressed nondimensionally as

$$C_D = \frac{24}{Re_d} + 4.5.$$

Oseen's result was calculated from an approximate form of the Navier-Stokes equation in which fluid inertia was partially accounted for through linearized inertia terms. The solution of Oseen's equation takes the form of a series; Oseen computed the first two terms, as indicated in the above C_D expression. Goldstein[38] later calculated further terms in the series, but agreement between experimental and theoretical results was not materially improved.

Experimental data for $0.1 < Re_d < 1$ was obtained by Arnold[36], Möller[26], Liebster[39], Schmiedel[30], and Maxworthy[40]. The recent experiment by Maxworthy, very carefully performed using sapphire spheres falling in a temperature-controlled glycerol-water mixture, has yielded the most accurate low Re_d drag data obtained to date. Liebster tested steel spheres falling in glycerol, sugar solutions, and water, while Schmiedel studied the fall of steel and aluminum spheres in glycerol-water mixtures.

c. <u>$1 < Re_d < 2000$</u>: With increasing Re_d in this range, the drag on a sphere undergoes a gradual transition from domination by viscous effects to pressure drag resulting from flow separation. An interesting feature of the C_D - Re_d curve is the absence of any indication of the separation bubble formation. In other words, there is no noticeable change in the curve in the vicinity of $Re_d = 24$, where separation commences. Evidently the pressure distribution of the outer flow is not perceptibly altered by the separation bubble, which is very thin when it first forms. Furthermore, very little skin friction is lost because the sphere surface from which the flow has separated is nearly perpendicular to the mean flow, and consequently friction on this surface contributes essentially nothing to the drag force even when there is no separation.

Apparently the pressure drag produced by separation is only slightly greater than the loss of skin friction drag as the separation bubble grows, resulting in a smooth C_D - Re_d curve of gradually increasing (though negative) slope as Re_d increases.

Drag coefficient data for $1 < Re_d < 2000$ was provided by many sources. In addition to the tests of Arnold, Möller, Liebster, Schmiedel, and Maxworthy, which have already been cited, experiments in this range were performed by Allen[41], Hawk[23], and Wieselberger[42]. Allen measured the rate of fall of amber spheres in water, while Wieselberger determined the drag on spheres mounted in a wind tunnel.

The only experiments with buoyant spheres at Re_d below 1000 were performed by Hawk, who studied the free rise of hollow aluminum spheres in glycerol-water mixtures. The discrepancy between his data and that of others in this range is believed to result from the low ratio of sphere density to fluid density, and also may involve inaccurate determination of fluid properties.

d. <u>$2000 < Re_d < 200,000$:</u> When Re_d has reached approximately 1000, the separation circle has advanced nearly to the equator of the sphere[20]. For Re_d above this value, skin friction drag is much smaller than the drag created by the low pressure in the separation region, so that the drag is almost entirely pressure drag. Although the separation circle continues to move upstream gradually as Re_d increases, the net pressure force on the sphere is quite insensitive to such shifting (as the surface near the sphere equator is nearly parallel to the drag direction and, therefore, C_D remains nearly constant, increasing very slightly as Re_d is increased up to the critical range. Because C_D is almost constant, the drag force increases as Re_d^2; for this reason the range $2000 < Re_d < 200,000$ is known as the quadratic drag range.

Experiments covering this range of Re_d have been reported by Wieselberger[42], Shafrir[43], Lunnon[44], Allen[45], and Shakespear[46]. Shafrir, in his recent work, observed spheres of various materials falling in water, as Lunnon had done earlier. Allen's tests were performed with steel spheres dropped in water. Shakespear performed his experiments by dropping weighted celluloid spheres through air in a tower.

e. <u>$200,000 < Re_d$</u>: Available sphere drag data for $Re_d >$ 200,000 has been generated primarily by wind tunnel experiments, although a number of other techniques have been employed. The four sets of critical range data plotted in Fig. 7 plainly show the extremely wide variety of C_D - Re_d behavior existing in this regime.

Millikan and Klein[47] obtained their data with a sphere mounted on an airplane. They actually obtained 291 data points; only the spread of these points is indicated on the plot. This curve is the best representation known of the C_D - Re_d relationship for a smooth, rigidly mounted sphere in a turbulence-free wind stream.

For comparison, Flachsbart's[48] wind tunnel results are also shown in Fig. 7. The situation is the same as for the Millikan-Klein data (smooth, fixed sphere) except for the low but finite turbulence level in the wind tunnel stream. The only noteworthy difference between the two sets of data is the shift to lower Re_d produced by the turbulence.

The other two sets of data in this regime resulted from free-flight tests. The Bacon and Reid[49] data was obtained by dropping wax, rubber, and wooden spheres from an airplane into still air and tracking their fall with a recording theodolite. Radar tracking of freely rising balloons provided the data given by Scoggins[11]. In both these cases the spheres were free to rotate, alter direction, and change speed. These effects were, of course, much more pronounced in the case of the balloons, due to their much lower density. The influence of the removal of rigid constraint is plainly evident in both sets of data and clearly increases with increasing ability of the sphere to respond to wake fluctuations.

3. Unsteady Behavior During Quasi-Steady Motion

Although studies of the unsteady behavior of freely-moving spheres have only recently been undertaken, the fact has long been known that a freely rising or falling sphere does not always follow a precisely vertical path at uniform speed. For example, Newton[1, p. 364] noted that light weight spheres "did not always fall directly down, but sometimes fluttered a little in the air, and waved to and fro." In 1920 Schmidt[50] reported observing periodic changes in the speed and direction of a wax sphere dropped in water as vortex loops were released in the wake. Bacon and Reid[49] mentioned unusual irregularity in C_D measurements performed with balloons rising in very still air. Liebster's[39] measurements of falling spheres showed that lateral movements occurred simultaneously with periodic changes in the vertical velocity. And in 1928 Lunnon[44] mentioned "the slightly curved and spiral path which is always followed by a sphere falling through liquid."

More recently, Jones, Peterson, Schaefer, and Schulte[51], in the course of measuring upper atmosphere density with a freely falling accelerometer-equipped sphere, discovered that under certain conditions excessive scatter appeared in their data, produced by lateral accelerations of the sphere. In his recent thesis, Sivier[52] reported that he was unable to obtain drag data for smooth spheres with his magnetic suspension equipped wind tunnel for Re_d between 300 and 550. The reason for this, he noted, was excessive transverse motion of the sphere.

The greatest impetus to the study of unsteady motions of free-flight spheres has come from the realization that spherical meteorological balloons do not accurately measure wind profiles. The need for high resolution wind profiles has been great enough that several research programs have been initiated to analyze the unsteady behavior of spheres.

Most noteworthy of these studies is the work reported by MacCready and Jex[13]. They present an enlightening discussion of the sphere flow problem in general and, in particular, they give a very informative fluid dynamical analysis of the behavior of freely moving spheres in the vicinity of the critical Re_d regime. For example, they point out that a rising or falling sphere cannot have the same C_D - Re_d relationship in the critical regime as an identical sphere rigidly held in a wind tunnel. This is so because the portion of the C_D - Re_d curve with slope less than -2 is a region of instability for an ascending or descending sphere. Another significant point brought out is the importance of the relative mass (= ratio of sphere mass to displaced fluid mass) in determining the unsteady motion of a sphere.

Data presented by MacCready and Jex, gleaned from balloon ascent tests and experiments with rising and sinking balls in a swimming pool, covers the range $10,000 < Re_d < 1,000,000$. In general, this data shows that average C_D values (based on average vertical velocity) are greater for low relative mass spheres at any Re_d. Also, a very rough correlation is shown between a "motion magnitude" factor (essentially the ratio of lateral excursion amplitude to the excursion wavelength) and relative mass, the motion magnitude factor being generally greater for lower relative mass spheres. The balloon data corroborates their prediction regarding "forbidden" segments of the C_D - Re_d curve by showing jumps from supercritical to subcritical Re_d along C_D-Re_d lines with slopes of precisely -2. *

Commenting on the general features of the motions observed in the swimming pool tests, MacCready and Jex point out that coupling between lateral and rotational spheres motions often occurred. They summarize by stating that lateral motions at subcritical Re_d were regular spirals or zigzags, with a wavelength on the order of twelve diameters, while motions at supercritical Re_d appeared to be "wandering spirals."

---

*It should be noted that most light-gas filled balloons with diameters of a few feet will, in the course of rising several miles through the atmosphere, pass through the critical range of Re_d, going from high Re_d to low Re_d.

Mac Cready and Williamson[14], in a continuation of the work just described, showed that most of the differences between C_D - Re_d curves for freely moving spheres of large and small relative mass were eliminated when C_D was based on true velocity rather than average vertical velocity. In fact, C_D data obtained this way all fell below the "standard" sphere drag curve (corresponding to Fig. 7 in this paper). However, MacCready and Williamson used the buoyancy force, assuming it to be equal to the average drag force, in calculating their values of C_D. Since the true value of C_D must be computed from the instantaneous velocity and drag in an unsteady situation, data such as that presented by MacCready and Williamson must be evaluated with some caution.

MacCready and Williamson also showed that the average wavelength of lateral motion for $100,000 < Re_d < 1,000,000$ was approximately eleven sphere diameters for low relative mass spheres.

A very extensive set of tests and data analyses was performed by Rogers and Camitz[15], who used a high precision pulse Doppler radar to track rising helium-filled superpressure Mylar balloons in order to obtain power spectra of the random unsteady motions. They determined that at supercritical Re_d appreciable spectral content exists in the wavelength range from 12 to 44 diameters (for two meter diameter balloons) with a peak in the spectrum consistently occurring at a non-dimensional wavelength (λ/d) of approximately 24, and that these fluctuations arise primarily from horizontal random velocity perturbations having a dimensionless root-mean-square value of about 0.37. They note a considerable variation in spectral shapes and caution that one spectral shape may not be sufficient for adequately describing smooth sphere behavior. Finally, they mention that in the supercritical regime balloons appear to rise with essentially constant vertical speed and fluctuating horizontal velocity components, while the velocity fluctuations in the subcritical regime seem to be of equal intensity in all directions.

Unsteady sphere motion data has been obtained by Shafrir[43] in the range $1000 < Re_d < 50,000$. These tests were all conducted by photographing stroboscopically illuminated spheres of relative mass from 1.15 to 8.47 as they fell through water. No fundamental relationships were obtained, but several features of the data deserve mention.

Non-dimensional amplitudes of lateral motion were found to increase with Re_d; they also tended to increase with relative mass, contrary to the prediction of MacCready and Jex[13]. Non-dimensional wavelengths of the unsteady lateral motions increased from a minimum of 25 for spheres with a relative mass of 1.15 to as high as about 80 for the large relative mass spheres. Dimensionless wavelengths displayed a slight tendency to decrease with Re_d. Finally, the motion magnitude factors, while exhibiting considerable scatter, showed a decrease with relative mass and displayed an increase with Re_d up to $Re_d \approx 10,000$ followed by a decrease for higher Re_d.

Preukschat[53] also studied freely moving spheres in water. On the basis of free fall tests over the range $500 < Re_d < 42,000$, he concluded that no oscillations exist for spheres with relative mass greater than unity. This contradicts Shafrir's results, but the more refined technique used by the latter probably produced more accurate results.

Oscillations were evident in Preukschat's experiments with buoyant spheres for Re_d between 800 and 9400 and relative masses from from 0.526 to 0.875. He determined that the unsteady motion was two dimensional, sometimes becoming helical after a few cycles. Dimensionless wavelengths of the transverse motion increased with relative mass from approximately 12 to 26. Amplitude data was too scattered to reveal any dependence on relative mass or Re_d.

One other significant result reported by Preukschat was that C_D values based on local velocity (rather than average vertical speed) were independent of the extent of the lateral motions.

Fluctuating lift forces on a sphere at supercritical Re_d were measured recently by Willmarth and Enlow[33]. They found that neither the power spectrum nor the root-mean-square value of the lift coefficient C_L varied with Re_d in the range $484,000 < Re_d < 1,667,000$. The value of $\sqrt{C_L{}^2}$ was approximately constant at 0.062.

No dominant frequencies appeared in the spectra of the fluctuating lift; the greatest spectral densities occurred at the lowest frequencies measured. During the experiment, a large-scale low frequency fluctuation was observed in the lift force; this fluctuation appeared to be almost a square wave with nearly constant amplitude but random period. The amplitude of this low frequency fluctuation was at least as large as the amplitude of the higher frequency fluctuations superimposed on it. However, the cause of the phenomenon was not determined because the wake behavior could not be studied (flow visualization equipment was not available)[54].

4. Accelerated Motion

Relative acceleration between a sphere and a fluid occurs in many situations and has therefore been a matter of considerable interest to fluid dynamicists. Examples of situations in which such accelerations are involved are the atomization of fuel sprays and the currently very important problem discussed above, of particle entrainment in rocket motor exhaust gases.

In their review of particle-fluid interaction problems, Torobin and Gauvin[4] discuss a number of experimental investigations of sphere acceleration. Although they point out that knowledge of accelerated sphere motion is cruder and much less extensive than in the case of steady motion, several conclusions can be drawn on the basis of existing data.

One important observation is that the "apparent mass" concept is totally inapplicable beyond the initial stage of relative motion between the sphere and fluid. The apparent mass concept arises from potential flow theory, since it can be shown that the resistance to acceleration of a body in an inviscid fluid of infinite extent is simply

$$R = (m + m_a)\, a,$$

where R is the resisting force, a is the acceleration, m is the mass of the body, and m_a is the apparent mass, which depends only on the body geometry and the fluid density . For a sphere, m_a is just half the mass of the displaced fluid[18, p. 124].

Early efforts at assessing the effect of acceleration on particle drag in a viscous fluid involved an attempt to include the influence of fluid inertia by straightforward application of the apparent mass concept. As Goldstein[55] shows, however, the flow about a body is irrotational only at the instant of initiation of the motion. The vorticity generated at the body surface immediately begins diffusing into the fluid and is convected into a wake. If the motion is such that large Re_d is reached very rapidly, the vorticity will remain confined to a thin boundary layer adjacent to the body surface and a thin laminar wake, and the flow about the body will closely approximate potential flow until separation occurs. Schlichting[21, pp. 222-223] presents flow field photographs and pressure measurements illustrating this behavior for a circular cylinder. In such cases, it is reasonable to expect that the apparent mass concept will be approximately valid until boundary layer separation becomes significant. More will be said on this matter in a later Section.

Torobin and Gauvin also concluded that sphere acceleration phenomena are correlated by the acceleration modulus $A = ad/U^2$, citing the sphere results of Bugliarello[56] and the works of several other authors who studied disks and cylinders for support of their statement. Although Lunnon[57] states that his results, which were obtained in an extensive series of measurements on steel spheres dropped in mine shafts, definitely do not scale with A, his data falls in the Re_d range from 10,000 to nearly critical values and may very well have suffered from critical Re_d effects owing to sphere roughness and/or air currents in the mine shafts.

Since the apparent mass concept has clearly failed to account for the changes in drag produced by acceleration, it has become normal practice to present results of acceleration tests in terms of functional relationships among Re_d, A, and C_D, with C_D defined in the traditional manner. Existing data indicates that C_D increases with A, for $A > 0$ and Re_d constant, and that for fixed positive A, the difference between C_D and $C_D(A=0)$ diminishes as Re_d is increased.

For negative acceleration, $A < 0$, the situation is somewhat unclear. Ingebo[58] found a unique C_D - Re_d relationship for clouds of solid spheres and evaporating liquid droplets at values of $A = O(-10^{-5})$. His values of C_D faired into the standard sphere drag curve at Re_d = 6 but fell increasingly below the $C_D(A=0)$ curve as Re_d increased to 400. In a more recent experiment which was free from the interactions that may have occurred in Ingebo's clouds of particles, Selberg and Nicholls[59] used a shock tube operating at low Mach numbers to accelerate solid spheres (deceleration relative to the gas) and concluded that the low values of A ($-A \approx 10^{-4}$ to 10^{-3}) had negligible effect on C_D in the range $200 \leq Re_d \leq 1500$.

The latter data is believed to be correct, because the experimental arrangement used by Ingebo appears to have produced large flow disturbances. However, the matter could certainly bear further investigation, particularly in light of its relevance to the particle entrainment problem.

Another point regarding sphere deceleration ($A < 0$) deserves discussion. It has been suggested by Lunnon[57] and by Torobin and Gauvin[4] that $C_D(A \neq 0)$ should be greater than the steady state value regardless of the sign of A. This view can not be correct for all - A. Consider, for example, a sphere moving through a still fluid at constant velocity and with a fully-developed wake. The fluid entrained in the wake moves, relative to the undisturbed fluid, in the direction of sphere motion, but with a lower velocity. If the sphere is brought rapidly to rest, corresponding to large, negative A, the momentum of the wake flow will cause it to wash over the rear surface of the sphere, exerting a force on the sphere in the upstream direction (i. e., a negative drag force). Relating this argument to the case of a sphere entrained in a fluid stream, it is clear that for large -A the C_D can be significantly lower than C_D $(A=0)$ owing to the sphere being accelerated into its own wake.

C. AERODYNAMICS OF A DISK

The characteristic features of the flow of an unbounded fluid past a circular disk nominally oriented with its face perpendicular to the stream will be outlined in this section. The fluid is considered to be viscous, incompressible, and free of turbulence; the disk is thin and sharp-edged. As in the case of a sphere, these limitations imply that the nature of the flow about a disk is primarily a function of Re_d.

1. Flow Regimes

The flow field about a circular disk does not assume as wide a variety of configurations as does the sphere flow field. Principally, this is a result of the separation line being fixed at the disk rim. Because of this, the well-known rapid decrease in C_D that occurs with separation line shift on spheres and cylinders does not occur with the disk. For this reason, and also because the disk shape does not appear as frequently as the sphere in engineering applications, the disk flow has been less extensively studied than the sphere flow. Nevertheless, it is believed that the changes in the flow past a disk that occur as Re_d is varied are well understood in general, although several details are still lacking.

The following is an outline of the development of the disk flow field as Re_d is increased. The discussion is primarily concerned with the flow past a fixed disk, but effects that occur when the disk is free to oscillate and translate are also noted.

a. $0 < Re_d < 0.1$: The flow field about a disk in this regime of Re_d is controlled by a balance between pressure and viscous forces. This does not imply, however, that the forces acting on a disk are viscous. In fact, skin friction can not contribute to the net force acting on a disk oriented with its axis aligned with the flow direction, so the force on the disk is entirely due to the pressure distribution about the disk.

When $Re_d < 0.1$, the near-field streamlines of the flow past a disk exhibit complete symmetry about the plane of the disk.

b. $0.1 < Re_d < 1$: As Re_d increases above 0.1, fore-and-aft asymmetry begins to appear in the streamlines, indicating that inertial effects near the disk are growing to a significant level.

c. $1 < Re_d < 100$: Separation of the flow from the rear face of the disk occurs at $Re_d \approx 1$. Experimental evidence on this point is very sketchy. Stanton and Marshall[60] injected dye through the rim of a disk supported by a sting in a water tunnel and, by observing the flow of the dye, estimated that formation of the separation bubble with enclosed vortex ring occurred at $Re_d \approx 4.5$. They point out, however, that the difficulties in obtaining uniform flow at this low Re_d and in observing the details of the dye flow near the disk make their estimate of the separation Re_d rather uncertain. In addition, they mention elsewhere in their paper that the velocity profile in their test channel was nearly parabolic, throwing considerable doubt on all their results.

The value $Re_d = 1$ suggested above for the onset of flow separation was estimated from the results of Michael's[61] computer calculation of disk flow fields for Re_d of 2, 8, and 30, although some features of this work raise questions. His streamline plot for $Re_d = 2$ shows separation occurring on a circle of diameter about half that of the disk, the maximum thickness of the separation bubble being only about 5% of the disk diameter. However, there is some doubt in this author's mind that flow separation from a thin disk would begin at the rear stagnation point rather than at the disk edge, where the flow must execute an abrupt reversal in direction. This doubt is not diminished by the fact that Michael's solutions seem to indicate a slow asymptotic approach of the separation circle toward the disk edge. His streamlines for $Re_d = 30$, while showing a separation bubble whose length is nearly equal to the disk diameter, indicate that the diameter of the separation circle is still about 10% smaller than the disk diameter. In apparent contrast with this is a photograph by Schmiedel[30] showing clearly that the flow is separating at the rim of disk at $Re_d = 48.6$. Experiments to answer this question have yet to be made.

As Re_d increases from 1 to 100, the separation bubble grows until it is more than 1 1/2 disk diameters long at $Re_d = 100$. Vorticity tends to concentrate in a boundary layer on the disk face and in the separated sheet springing from the edge of the disk and is convected and diffused into the surrounding fluid through a steady laminar wake.

d. $\underline{100 < Re_d < 250}$ (est.): According to Simmons and Dewey[62], the separation bubble of a disk held perpendicular to the flow becomes unstable at $Re_d \approx 100$ and the process of shedding vortex loops commences. In this Re_d regime, the loops all appear to be shed from the same location on the rear face of the disk, analogous to the early stages of sphere vortex-loop shedding described above. Evidence of this behavior is given in wind tunnel flow photographs by Simmons and Dewey and by Stanton and Marshall's[60] water tunnel flows.

The flow field is very different in the case of a freely falling disk. The ability of such a disk to pitch about a diameter in response to pressure variations produced by asymmetry in the separation bubble allows a complex coupling between disk orientation and wake generation to ensue. The resulting oscillatory character of the motion of the disk-plus-wake system was extensively investigated by Willmarth, Hawk, and Harvey[63] and will be discussed below.

e. $\underline{250 < Re_d}$: The details of the remainder of the Re_d range for fixed disks are not clear, but a few important features can be noted. At $Re_d \approx 250$, the vortex loop shedding begins to alternate, that is, successive loops are shed from diametrically opposed sites on the rear face of the disk. For $250 < Re_d < 350$ (roughly), the loop shedding is essentially confined to a plane. As Re_d increases above 350, loops tend to be shed from random positions about the disk circumference. The frequency of loop shedding increases with Re_d and the appearance of discrete vortex loops gradually disappears.

The disappearance of discrete vortex loops in the disk wake may be explained by the rolling up, because of instability, of the separation layer into small-scale vortex filaments which are carried directly into the wake by the main flow. As Re_d increases the shear layer instability increases and increasingly smaller vortex filaments are cast into the wake which thereby gradually acquires a truly turbulent character. The wake may be considered fully turbulent when $Re_d > 10,000$.

Despite the changes occurring in the disk wake, the geometry of the separated shear layer near the disk remains essentially constant for $Re_d > 1000$ (approximately).

2. Steady Drag

Disk drag data is not nearly as abundant as that for spheres. However, the existing data is consistent enough so that the C_D - Re_d relationship for disks may be considered as definitely established. It should be noted, though, that one segment of this data, between

$Re_d \approx 100$ and $Re_d \approx 1000$, will receive critical comment in a later Section. All available C_D data for disks has been plotted in Fig. 8.

In the following, the features of the C_D - Re_d curve will be noted along with brief discussion of the experiments from which the data of Fig. 8 was obtained.

a. $\underline{0 < Re_d < 1}$: When $Re_d < 1$, C_D is very adaquately represented by the relation

$$C_D = \frac{20.37}{Re_d} + 3.242,$$

which was obtained by Oseen[64] in a manner similar to his calculation for sphere drag. Again, the solution of Oseen's equation is an infinite series, only the first two terms of which were calculated. The first term reproduces the earlier result of Oberbeck[18, pp. 604-605], whose computation paralleled Stokes' sphere drag calculation.

The experimental C_D data for this Re_d range was obtained by Schmiedel[30], with aluminum, gold, silver, and steel disks which were dropped in mixtures of glycerol and water.

b. $\underline{1 < Re_d < 100}$: Drag data for this range has been taken from the results of Schmiedel and of Willmarth *et. al.* [63], who also dropped disks made of various materials in glycerol-water solutions. Fluid inertia plays an increasingly important part in determining the flow in this range of Re_d, causing the C_D curve to deviate increasingly from the Re_d^{-1} behavior characteristic of purely viscous flows. C_D values calculated by Michael[61] in the course of his computer work are also plotted and indicate excellent agreement with the experimental data.

c. $100 < Re_d < 250$: For these Re_d, the experimental C_D values display a great deal of scatter. This is explained by the fact that the data in this range was all taken from the free fall tests by Schmiedel and Willmarth *et. al.* in which the disks executed pitching motions and lateral excursions. The C_D values here were based on average vertical velocity. However, as Willmarth *et. al.* pointed out, the concept of a simple drag coefficient loses meaning when this unsteady disk motion occurs because of the complicated set of unsteady forces that actually act on the disk.

d. $250 < Re_d < 1000$: The data in the next range, $250 < Re_d <$ 1000, was obtained during the wind tunnel experiments performed by Simmons and Dewey[62]. This author believes the apparent agreement between these C_D values and the previously-discussed data ($Re_d < 250$) to be accidental. These disks were mounted in the wind tunnel in such a way that they were free to oscillate. Had they been rigidly mounted, it is probable that the resulting C_D values would have been considerably lower, close to unity. It might also be noted that Simmons and Dewey estimate their accuracy at ±20% for the lowest Re_d.

e. $\underline{Re_d > 1000}$: Wind tunnel disk drag measurements by Wieselberger[42], Knight[65], Prandtl[66], Shoemaker[66], and Simmons and Dewey[62] produced the C_D data for $Re_d > 1000$. The apparent constancy of C_D in this range results from the fixed geometry of the separated layer, as mentioned above.

3. Unsteady Behavior During Quasi-Steady Motion

The fact that freely falling disks oscillate and translate laterally when vortex loop shedding occurs has already been mentioned. The interaction of the disk dynamics and the wake fluctuations is in some respects a more complex phenomenon than the sphere-wake interaction. Basically, this results from the ability of pressure to rotate a disk about a diameter, the variation of disk C_D with orientation, and the ability of the disk to generate lift when its axis is not coincident with the direction of motion.

A detailed study of the unsteady motions of freely falling disks has been made by Willmarth *et. al.*[63] for Re_d up to approximately 10,000. They have been able to map out the boundary between stable (non-oscillating) and unstable (steadily oscillating) disk fall situations in terms of Re_d and I^*, the latter being the ratio of the moment of inertia of the disk about a diameter to the moment of inertia of a fluid sphere of the same diameter. The boundary occurred at $Re_d \approx 100$ except for I* in the range 10^{-4} to 4×10^{-3}, where it curved into higher values of Re_d, peaking at $Re_d \approx 170$ for $I^* = 10^{-3}$. At the larger I* values, where the disks tend to behave more like fixed disks owing to the greater inertia, the onset of oscillation at $Re_d \approx 100$ correlates with the initiation of vortex loop shedding observed in wind tunnel tests. The increase in Re_d on the stability boundary with decreasing I* was thought to be caused by changes in the phase relationship between the disk pitching motion and the vorticity generation and shedding processes.

The unsteady disk motions occurring for $Re_d > 100$ were found to fit into three general categories. Disks with large I* ($> 10^{-2}$) tumbled; that is, after executing two or three pitching oscillations with growing amplitude, the disks would overturn and fall away in a random manner. Small amplitude lateral motions and large amplitude pitching oscillations characterized the behavior of disks with I* slightly below 10^{-2}; decreasing I* brought a decrease in pitch amplitude and an increase in the amplitude of the lateral excursions.

Near the stability boundary (specifically, for Re_d between 100 and 1000) the dimensionless frequency of disk oscillation nd/U, where n is the cyclical frequency, was a function of both I* and Re_d, but for

$Re_d > 1000$ the dependence on Re_d vanished and nd/U became a linear function of I* given roughly by

$$\frac{nd}{U} = 0.62 - 470\, I^*.$$

Lateral motion amplitudes were not recorded.

Willmarth, Hawk, Galloway, and Roos[17] reported a series of experiments involving disks mounted in a wind tunnel. Two basic cases were studied: a rigidly held disk and disks fixed in place but free to rotate on a diametrical axis perpendicular to the wind stream. A large quantity of data, much of it statistical, was generated by the experiments. Just a few of the more pertinent results will be discussed here.

The pivoted disks, which were tested in the Re_d range from 68,000 to 636,000, all were found to oscillate continuously with randomly varying amplitude and phase. Dimensionless frequencies of these oscillations scaled with $(I^*)^{-0.44}$ independently of Re_d. In no case did the oscillations tend to diverge nor did auto-rotation occur.

The rigidly held disk was equipped with a moment balance designed to measure the moment acting on the disk about a diametrical axis normal to the free stream. Root-mean-square values of the coefficient of unsteady aerodynamic moment in the range $10^5 < Re_d < 10^6$

displayed no Re_d dependence. The constant value of $\sqrt{\overline{C_M'^2}}$, where

$$C_M' = \frac{M'}{\frac{\pi}{8}\rho U^2 d^3},$$

M' being the randomly-fluctuating aerodynamic moment, was 0.0047.

Dimensionless power spectra of the fluctuating aerodynamic moment were also obtained for several Re_d between 187,000 and 1,050,000. These, too, demonstrated a lack of dependence on Re_d, scaling completely with dimensionless frequency. This implies that there exists no significant variation in the character of the unsteady wake, which is responsible for the fluctuating moment, in the Re_d range from 10^5 to 10^6.

III. EXPERIMENTAL APPARATUS

A. INTRODUCTION

This Section deals with the design, construction, and operation of the equipment used in the experimental study of sphere and disk flows. The factors considered in the overall design of the experimental apparatus are explained first. This is followed by a discussion of the details of the mechanical and electrical equipment and the manner in which this equipment was used to obtain the experimental measurements.

B. DESIGN CONSIDERATIONS

The first design question to be settled involved the selection of a working fluid for the experiment. Since rather low Reynolds numbers were to be encountered, the objective was to obtain relatively large, and therefore easily measureable, forces at these low Re_d. To accomplish this it was necessary to operate with a fluid having a large $\mu\nu$. To see this, consider the expression for sphere or disk drag:

$$D = C_D \frac{\pi}{8} \rho U^2 d^2.$$

Now

$$\mathrm{Re}_d = \frac{Ud}{\nu}, \quad \nu = \frac{\mu}{\rho},$$

so that

$$U^2 = \frac{\nu^2}{d^2}\,\mathrm{Re}_d^{\,2} = \frac{\mu\,\nu}{\rho d^2}\,\mathrm{Re}_d^{\,2}$$

and therefore

$$D = \frac{\pi}{8}\,\mu\nu\,\mathrm{Re}_d^{\,2}\,C_D.$$

Since the drag coefficient C_D is a unique function of Re_d, it is clear that at a fixed Reynolds number the magnitude of D depends only on the product $\mu\nu$ of the fluid.

While ν of air is comparable to ν of a number of liquids, e. g., ethylene glycol, the density of air is much less than the density of any liquid. Consequently, $\mu\nu$ of air is considerably smaller than $\mu\nu$ of most liquids and therefore wind tunnel testing (in air) was eliminated from consideration, at least for low Re_d. Because all usable liquids possess a specific gravity within about 50% of unity, the problem was reduced to one of selecting a suitable liquid with as large a μ as possible. Several liquids were considered, notably ethylene glycol, propylene glycol, glycerol, and various oils. Glycerol was finally chosed for its stability, safety (it is non-toxic and non-flammable), clarity (to permit use of flow visualization) and complete miscibility with water.

This last characteristic was desirable because it permitted adjustment of μ by dilution with appropriate quantities of distilled water.* It was necessary to have this capacity because the strain gage transducers which were used in this experiment had a useful force-sensing range covering a factor of no more than 1000. Referring to the above expression for D, it is seen that at a fixed μ (and ν) this limitation on the magnitude of D permitted investigation of a Re_d range over a factor of about 35 or so, assuming an approximately constant C_D. Hence, coverage of a broad range of Re_d required either several strain gage transducers or adjustment of μ.

The next matter to be decided was how the relative motion between test body and fluid was to be achieved, i. e., whether to move the fluid past the body or the body through the fluid. A number of practical considerations supported the choice of the latter method.

From a mechanical standpoint, the design and construction of a suitable fluid tunnel would have been much more complicated than was the establishment of a towing apparatus. The power necessary to move

---

*An additional advantage of this fluid system was the availability of tabulated density and viscosity data, e. g., reference 67. Using these tables, ρ and ν could be determined simply by measurement of fluid temperature (assuming a mixture of known proportions).

a large quantity of high viscosity liquid through a tunnel would have been enormous compared with that required to tow the test body through the fluid. Also, the large quantity of energy dissipated in the moving viscous fluid would have produced time variation of fluid properties due to temperature increase unless a heat exchanger were built into the tunnel.

Another difficulty with a liquid tunnel would have been the rapid growth of wall boundary layers at very low Re. In addition to reducing the cross-section dimensions of the uniform flow within the test section, the growing boundary layer would have accelerated the uniform core flow unless the test section were designed to compensate for this growth. However, it would have been impossible to achieve such compensation over the wide range of Re to be studied in this experiment since boundary layer growth rate depends strongly on Re. An example of this sort of difficulty is provided by the test section velocity profiles shown by Shair, Grove, Petersen, and Acrivos[68] for their low Re oil tunnel. These profiles indicate that the flow is neither uniform across nor uniform along the test section. Finally, although it was a secondary consideration, the great difficulty of performing unsteady motion studies in a fluid tunnel influenced the decision.

One significant disadvantage inherent in the technique selected is the rather brief permissible duration of a test run imposed by the finite length of the fluid channel. In the present situation, the test body is limited to a translation of about 120 body diameters. This inhibits the study of unsteady flow phenomena occurring at low Re_d, where wake instability is slow to develop.

Once the decision to move the sphere or disk through a stagnant liquid had been made, a suitable tracking system was necessary to permit smooth one-dimensional motion. Instead of a conventional wheels on rails setup, a linear air bearing system was selected to provide the tracking.

Although more expensive than the former, it was hoped that the air bearing system would minimize jiggling and vibration of the translating carriage through elimination of all solid to solid contact. Also, a commercially available V-groove air bearing* was utilized in the system, so the expense of designing and fabricating such a unit was not encountered, although designing and building a simple secondary bearing was necessary.

The track system consisted of a 32 foot long V-groove air bearing and an equally long 2 inch square tube, parallel to the V-groove

---

*The Search Linear Air Trough, manufactured by the Search Corporation and distributed by the Macalaster Scientific Corporation.

unit and 9 inches to one side of it (Figs. 9 and 10). The carriage supported on these bearings was a triangular plate attached via pivots to three gliders, two of which rode in the V bearing. The V unit fixed the location of the carriage vertically and laterally and prevented pitching and yawing of the carriage. However, owing to the long moment arm of the model support strut, the V bearing was incapable of effectively counteracting roll. The incorporation of the square-tube bearing into the system permitted cancellation of rolling moments. The sixth degree of freedom of the carriage, translation along the track, was controlled by a motor and cable-loop arrangement.

The next design problem was the selection of a means of measuring the forces and moments acting on the test body. External, internal, and sting balance systems were studied; strain gages, piezoelectric crystals, and differential transformers were considered for use as transducing elements.

Two important factors eliminated an external (i. e., outside the fluid) balance from consideration. First, an external balance would have had a much lower natural frequency, and therefore much poorer frequency response, than the other balance types owing to the necessarily greater mass supported by the sensitive elements. The other factor was the very low sensible moments due to the long moment arms between the test body and the transducers in an external balance.

For the best mixture of simplicity, sensitivity, and good frequency response characteristics, a combination of internal and sting mounted transducers was selected. Since static measurements were required, piezoelectric devices could not be used. Strain gage units were chosen for the sensing elements because of the relative bulk and poor sensitivity of differential transformers.

Visualization of the flow past the sphere or disk was chosen over other means of studying the relationship between the flow field and the unsteady wake. Since the expense of the glycerol prevented repeated renewal of the working fluid, the visualization method had to be non-contaminating. This ruled out the use of dyes or dispersed particles such as fine aluminum powder. The hydrogen-bubble technique was finally settled upon. In this method a fine platinum wire moving through the fluid with the test model is used as the cathode in the electrolysis of water. The very small hydrogen bubbles which are produced along the wire are swept off to act as tracers in the flow.

C. MECHANICAL EQUIPMENT

1. Towing Channel

The towing channel (Figs. 9 and 10) in which all the experiments were performed is 31 feet 8 inches long, 24 inches wide, and 26 inches high and is normally filled to a depth of 24 inches. The channel itself, seemingly a very simple piece of equipment, actually called for a great deal of time and effort.

The original channel installation was made of formed galvanized steel sheets riveted and soldered together and supported externally by a framework of slotted steel angle. The initial soldering of the channel seams was not successful, with the result that the channel leaked badly. This leakage was worsened by flexing of the steel panels as the channel was filled, which tended to crack the seams open at weak points.

Considerable energy was expended in various attempts to eliminate the leaks in this metal channel, including repeated soldering, caulking, and taping of the seams. Finally, a liner of fiberglas cloth impregnated with epoxy resin was installed. However, even this last effort failed to stop leakage over a period of time due to failure of the epoxy-to-metal bond combined with leakage through pinholes left in the epoxy-fiberglas matrix. Therefore, the channel was torn out and scrapped, except for the steel supporting frame.

The second and final channel was started with the steel frame retained when the sheet metal channel was torn out. Side and end panels of 1/2 inch plywood were bolted to this frame, flush-head bolts being used to keep the inner surface smooth. The building floor itself formed the bottom of the channel; the corners between the floor and the side and end panels were filleted to approximately a two inch radius with concrete. Using this structure as a permanent form, two laminations of fiberglas cloth thoroughly impregnated with polyester resin were built up on the inner surface. Finally, a surface coat of resin was applied. Black pigment was dispersed in this batch of resin to provide a dark background surface for the flow visualization studies. This installation has proved to be very successful: in nearly a year of use, no leakage whatever has occurred.

Two 1000 gallon collapsible rubber tanks* are utilized for storage of the glycerol-water solutions. Fluid is transfered to and from the channel by an electric motor driven pump**. When ordinary tap water is used in the channel, filling is accomplished via the building water lines; the channel is emptied in such cases by simply siphoning the water into a nearby floor drain.

2. Air Bearings

As was noted above, the test model and carriage structure was supported on two parallel linear air bearings, one of these being a V-groove type and the other a simple square tube (Figs. 10 and 11).

---

*U. S. Rubber Company Sealdrum 1000.

**MP Pumps, Inc., model R 15303B.

The V-groove trough consisted of three Search Air Troughs, two of which were 12 feet in length while the third was 8 feet long.* A single 32 foot unit would have been better in many respects, but the Air Troughs were only available in lengths of 12 feet or less. Consequently joining mechanisms, one of which is visible in Fig. 11, had to be made; these allowed adjustments to be made to provide precise alignment of the units.

Each Air Trough consisted of three aluminum extrusions welded into a rigid unit (Fig. 12). Rigidity was provided by a 4 inch deep I beam. Atop this beam was mounted a special extrusion which includes the 90° V, each surface of which was backed up by a hollow chamber through which the air was supplied. Midway up each side of the V a series of small holes had been drilled and a narrow longitudinal milled slot connected all the orifices in the face of each half of the V-groove. The third extrusion in the structure was a simple 1/8 inch thick right angle which also had a string of holes drilled in each side of the V with the same spacing as the holes in the other V extrusion. The positioning of this piece was such that when it was welded into place the holes intersected the longitudinal slots in the first V mid-way

---

*These Troughs are essentially production versions of the laboratory demonstration unit devised and described by Neher and Leighton [69]. Search part numbers are 11001 (8 foot unit) and 11003 (12 foot units).

between the orifices in that extrusion. The purpose of this complex structure was to provide long, narrow air passages with concomitant large pressure drop to minimize the mass flow of air at a given operating pressure without having to resort to using extremely small diameter orifices, which are very difficult to drill. Air was fed into both ends of each manifold at 15-20 psig. At these pressures the flowrate was estimated to be 60-80 scfm. Air flow through the orifices in the center portion of the 32 foot Trough was not observably different from that at the ends of the unit based on a rough check of glider-floating ability.

The two gliders used with the V bearing were 7 inch long aluminum blocks, cut down to minimize weight, each with a deep vertical hole in the center into which the pivot support for the appropriate corner of the carriage was fitted. These gliders can be seen in Fig. 11. It was found necessary to place the pivot point of the load attachment as deep in the glider as possible. If the pivot were too high, i. e., above the center of pressure of the glider, instability occurred and, when floated, the glider oscillated in pitch and yaw, producing a noticeable "chatter" as the glider ends came into contact with the air bearing surfaces, and an equally noticeable increase in friction between the moving glider and the bearing.

The square tube outrigger bearing consisted of two 16 foot lengths of 2 inch square, 1/8 inch wall extruded aluminum tubing joined end to end with a fitting that maintained alignment and included a pressure seal. The top surface of the unit was carefully filed to eliminate surface irregularities. Two longitudinal rows of 0.018 inch diameter (#80 drill) holes were drilled in this surface. These rows were 3/4 inch apart, equidistant from the centerline of the tube surface. The holes in each row were spaced at 1 inch intervals and the rows were staggered by 1/2 inch. Air was fed into this unit at the mid-point of each 16 foot section; normal operating pressure was 5-10 psig, requiring a flowrate of about 25-50 scfm.

The glider for the corner of the carriage supported by the outrigger tube was a 4 inch long, 1 3/4 inch wide piece of 1/2 inch thick aluminum plate. A vertical hole was provided in the center for the carriage support pivot.

Support for both air bearings was provided by cantilever beams attached to the building wall at 6 foot intervals. Each bearing was mounted on each support by a pair of adjustable stud bolts which permit vertical and rotational adjustment of the bearing. Because of the flexibility of the square-tube unit, it was found necessary to support this bearing at more points along its length. To accomplish this, Unistrut steel beams were installed between the cantilever supports and parallel to the bearings. Additional pairs of studs were installed between these beams and the outrigger bearing so that that unit is now supported every 2 feet.

The air to operate both bearings was drawn from the 100 psi building air line and was passed through a large capacity porous-stone filter* and thence through a pressure regulator**, one of which was used for each bearing. One inch copper tubing then carried the air to the various bearing inlet fittings.

3. Carriage and Strut

The strut-sting-model assembly was attached to an aluminum carriage (Fig. 11) which was supported through ball and socket pivots by three gliders, two V-type and the other flat-bottomed. Each pivot included a screw thread vertical adjustment for leveling of the carriage. Attached to the carriage was a hairpin shaped spring which engaged a pin on the flat-bottom glider and maintained the alignment of that glider with the outrigger bearing.

The base (actually the top) of the carriage was a triangular aluminum plate, with the center removed to reduce weight. One of the supporting pivots was attached to each corner of the carriage base. Fas-

---

*R. P. Adams Co. Type TR Poro-Stone Air Filter

**Schrader no. 3468XG Air Pressure Regulator tened to the outside edge of the base, i. e., the edge away from the outrigger bearing, was a vertical frame to which the strut was affixed. Finally, a stiffener plate lying in a plane perpendicular both to the carriage base and the vertical frame was mounted to these pieces to increase the rigidity of the structure.

A horizontal arm extended under the I beam of the V-groove air bearing from the lower end of the vertical frame. To the end of this arm was attached the towing cable. This attachment point was selected as a compromise between eliminating the couple produced by drag on the strut and model and eliminating the couple caused by acceleration of the moving mass.

The upper end of the model-support strut was mounted to the carriage assembly with two screws. This strut, the leading edge of which had been finished to an approximately parabolic profile, was originally made of Plexiglas to minimize weight. However, the Plexiglas strut was discovered to be far too flexible, so an aluminum strut was installed. The lower end of the strut was a cylindrical aluminum housing, halved lengthwise, for the model-support sting.

Mounted atop the carriage base plate was an aluminum box which contained several solid-state amplifiers and circuitry for these, and some of the wiring for the strain gage transducer circuits. This box, referred to below as the amplifier box, also contained a linear accelerometer positioned to sense acceleration along the track system. The equipment carried in the amplifier box will all be described more fully in Part E of this Section.

4. Motor and Towing Cable

The carriage is propelled along the track by a continuous loop of stainless steel cable which passes around pulleys at each end of the track. One of these pulleys is driven, through a rubber coupling, by a 1/3 hp. electric motor equipped with a transmission which provides continuously variable output shaft speed in both rotations.* The setup is presently such that the maximum attainable carriage speed is approximately 6 feet per second. The locations of the motor and cable are indicated in Fig. 9.

Considerable attention has been given to the problem of isolating the carriage system from the Zero-Max electric motor vibration. The base plate to which the motor and the cable drive pulley were attached was mounted to the building wall and floor through a very rigid structure. The pulley housing was mounted directly on the base plate, but the motor was mounted on vibration-damping motor mounts and, as

---

* Zero-Max model JK3-M3.

mentioned above, was connected to the pulley through a rubber coupling. In spite of these precautions, however, considerable vibration, produced by rotational and translational oscillations of the cable drive pulley, was transmitted along the towing cable.

Originally, a loop of Mylar tape was used for towing in the hope that the vibrations noted above would damp out within the tape. However, the low elastic modulus of the Mylar allowed the tape to act as a weak spring, permitting low-frequency oscillations of the carriage. Also, the propensity of the tape to develop an electrostatic charge through friction caused it to cling to parts of the track system. This tended to produce slippage and jerkiness in the towing system.

Several means of connecting the towing cable to the carriage system in such a way that transmission of vibration from the cable to the carriage would be eliminated were tried. Though not completely successful, the best method devised was a very soft rubber spring between the cable and the carriage. This eliminates much of the vibration, but introduced several other undesirable effects.

The most serious of these was oscillation of the carriage relative to the cable; for constant-speed cable motion, any variation in the drag acting on the carriage system(including bearing friction and fluid drag on model and strut) changed the tension in the rubber spring and, therefore, changed its length. So, in effect, a low-frequency vibration, or at least the possibility of one, was substituted for one of high frequency.

Two techniques have been used for determining the carriage speed. The method originally employed utilized a precision 360^o potentiometer driven through a reduction mechanism by the idler pulley in the towing cable loop. The wiper of this potentiometer was connected to one of the two channels of a strip chart recorder and the slope of the resulting x vs. t trace gave U.

When both channels of the recorder were needed for other data, a microswitch riding on the rim of the drive pulley was wired to one of the event markers (a non-proportional pen) on the recorder. A depression was cut into the pulley rim so that the microswitch would make and break contact once for each revolution of the drive pulley.

In the course of this experiment it became evident that some of the mechanical unsteadiness originally attributed to towing cable vibration was actually being produced by non-uniformity of the rotation speed of the drive motor output shaft. This was discovered during the analysis of some test data and was confirmed by a strobe light check of the shaft speed.

A geared down, electronically controlled d. c. motor* was installed in place of the original drive motor. Strobe light tests showed that the shaft speed of this motor was constant within 1%. With this motor in use, steadiness of the drive system increased and it became possible to connect the towing cable directly to the carriage, thereby eliminating the oscillation permitted by the rubber spring.

Data records from drag tests with the revised drive system displayed a marked decrease in the magnitude of drag force fluctuations. Flow visualization results were also improved, and a puzzling pulsation of the disk wake disappeared with the change of drive motors.

D. MODELS AND STRAIN GAGE TRANSDUCERS

1. Sphere and Disk

The sphere and circular disk (Figs. 13 and 14, respectively) used in the present tests were both machined from Plexiglas. Each was 3 inches in diameter; the disk was 3/8 inch thick, giving a thickness to diameter ratio of 1/8. Each body was made in front and rear halves; the rear part, with a circular hole to clear the sting support, attached with screws to the internal strain gage balance, while the

---

*Gerald K. Heller Co. Model 6T60 Variable Speed Motor.

front half-body was slip-fitted into position over a lip on the rear piece.

The sphere was checked for sphericity; the results showed that diameter variation was less than 1%.

The disk was actually a very short segment of a right circular cylinder. The intersections of the front and rear disk faces with the cylindrical side surface were sharp edges. Earlier tests at low and high Reynolds numbers[63, 17] indicated that, as long as the disk axis remained nearly parallel to the free stream, there was no apparent difference in aerodynamic properties between a true plane disk and one of small, but finite, thickness.

2. Disk Balance

The d. c. -powered strain gage balance used with the disk was originally intended to be used with the sphere also. However, early test results pointed out the need for a separate strain gage balance for the sphere. Such a balance was designed and built, the original balance then being used exclusively with the disk. The original balance will be referred to below as the disk balance.

The disk balance consisted of two units, made of aluminum, one of which was to be the drag-sensing transducer and the other a combination pitching and yawing moment transducer (see Figs. 14 and 15).

The moment transducer consisted of a solid central disk and an outer ring which were connected by thin, flat, radial aluminum strips positioned at 90° intervals around the disk circle. These strips were 0.050 inch wide, 0.015 inch thick (dimension perpendicular to plane of disk), and were securely clamped into the central disk and outer ring, the exposed length being 0.250 inch. The Plexiglas disk mounted to the outer ring, while the sting support connected to the central disk. Consequently, all loads acting on the disk were transmitted through the aluminum strips, which acted as bending flexures. A pair of strain gages was cemented to each flexure, one each on front and back. Considerable attention was paid to positioning the front and back gages as nearly identically as possible.

Two types of strain gages were used, two beams being gaged with each type. One type was a U-shaped unbacked semiconductor (piezoresistive) strain gage;* the other, a conventional metal foil gage with epoxy film backing.** The former has the advantage of possessing a much larger gage factor (140 as opposed to 3 for the foil gage) but also has several shortcomings when compared with

---

*Kulite type VFP-500-090, 500 ohms resistance.

**Micro-Measurements gage no. MD-DY-050AH-350, with resistance of 350 ohms.

foil gages.*

Chief among these shortcomings is the comparative difficulty of installing semiconductor gages. Because each semiconductor gage is a single, thin, brittle crystal filament of silicon, these gages are extremely fragile. The gages must be handled very carefully during cementing and can not be clamped into place while the cement cures. A result of this is a variation from gage to gage in the condition of the cement bond, e. g., the thickness of cement between gage and metal surface might vary. This variation, in turn, causes a variation in the strain response and temperature sensitivity among the gages.

A second problem is that, because of the small size and single-crystal nature of the semiconductor gage, properties of the gage itself can not be controlled as closely during manufacture as can those of conventional foil strain gages. Consequently, gage-to gage variations in gage properties are greater with semiconductor gages.

Another disadvantage of the semiconductor gage is that there exists no simple means of trimming the resistances of four such gages, after they have been mounted, to balance the Wheatstone

---

*Definitions and significance of various strain gage characteristics are given in Section 2 of reference 70. Properties of semiconductor strain gages are extensively discussed by Dorsey[71].

bridge circuit into which they have been wired. * The resistance of a foil gage, on the other hand, can readily be increased simply by rubbing gently on the foil grid with powdered pumice.

A fourth, and quite severe, problem with semiconductor gages appeared in the course of this work. It is appropriate to note it here even though it was not recognized at the time the choice of gage types was being made. This problem was "creeping" of the semiconductor gages when a load was applied to the gaged specimen. By this it is meant that, when the surface to which the gage was cemented was strained quickly from zero to a constant non-zero strain level, the semiconductor strain gage initially followed the surface strain but immediately began to relax back to its unstrained length. This phenomenon occurred regardless of whether the surface strain was tensile or compressive. It is not known whether this effect was a plastic flowing of the cement itself or a slippage at the interface between the strain gage and the cement.

Several factors are felt to be possible causes of this problem, which did <u>not</u> occur with the foil gages: the necessity of using a

---

*The theory of the Wheatstone bridge circuit is discussed in Perry and Lissner[70], Chapter 4. Some basic concepts relating to the use of strain gages in transducers are put forth in Chapter 11 of that work.

different cement with semiconductor gages;* the very smooth surface of the semiconductor crystal (making a good cement bond difficult to achieve); larger elastic modulus of the semiconductor crystal, compared to that of metal foil; and the considerably smaller wetted surface area of the semiconductor gage.

Because of the combination of advantages and disadvantages, both types of gages were used in order to directly compare the two in operation. The result of this comparison has been that, in the present application, the sensitivity and performance of the foil gages were more than adequate. Consequently, when the sphere balance was designed and built, foil strain gages were used exclusively.

Initially, the eight gages on the disk moment transducer were wired into two circuits, the four gages on each diametral pair of flexures being connected together in a four-active-arm Wheatstone bridge in such a way that this bridge circuit would become unbalanced when a couple was applied about an axis perpendicular to both the disk axis and the diameter along which the flexures lay, but would remain balanced when a pure axial (drag) load acted on the disk. This wiring,

---

*A solvent-thinned epoxy compound, Bean Adhesive RP-43, was used with the foil gages. This cement was not compatible with semiconductor gages because the impervious nature of the gage material would not readily permit the evaporation solvent to escape, so Bean RTC, a room-temperature curing epoxy cement free of solvent, was used to bond these gages.

however, had to be altered when it became evident that performance of the originally-planned drag transducer was completely inadequate.

The failure of the original drag unit involved several factors, chiefly poor design and the use of semiconductor strain gages. The drag transducer, it might be noted, had been designed specifically for semiconductor gages and could not be modified to accept foil gages.

The first alteration of the moment transducer strain gage circuits to permit measurement of drag involved simply rewiring of the yawing moment gages into a bridge circuit sensitive to drag instead of yawing moment. This actually required only the transposition of two connections on a strip of solder terminals. The desirability of measuring both moments simultaneously with drag remained, however, so another modification was introduced.

In this second alteration, the four gages in the yawing moment circuit were separated into two half bridges, a single pair of precision fixed resistors serving to complete both Wheatstone bridges (See Fig. 16 for circuit diagram). Each active half bridge consisted of the two gages mounted on one of the yawing moment flexures. Using operational amplifier circuits to be described below, the outputs from the two bridges were added to produce a signal proportional to drag and subtracted to yield a yawing moment signal. The gages in these circuits were foil gages; the pitching moment balance, which utilized the semiconductor gages, was not involved in any of the modifications.

Lead-out wires for the strain gage circuits were carried through the hollow brass sting support; at the rear of the sting they entered a rubber tube which carried them up and out of the fluid along the rear edge of the strut. The entire installation was then carefully waterproofed with a flexible epoxy compound.*

The natural frequency of the disk balance as finally used was 96.7 Hz.

3. Sphere Balance

As was mentioned above, it was originally intended that the disk balance, measuring pitching and yawing moments and drag force, would be used in conjunction with the sphere as well as the disk. However, several factors combined to indicate that a separate sphere balance would be worth while.

First, whereas the moment acting on a disk is produced by pressure forces, when the wake is separated, and consequently can be quite large (approaching roughly the order of magnitude of the product of drag force and disk radius), the moment on a sphere in incompressible flow must necessarily arise entirely from azimuthal nonuniformity

---

*Bean Gagekote Number 5, a two-component material that cures at room temperature.

of viscous stresses at the sphere surface and is therefore much smaller in comparison. This means that accurate measurement of the moment on a sphere would be considerably more difficult than in the case of the circular disk.

Second, high Reynolds number tests of a two foot diameter Styrofoam sphere in the University of Michigan 5 foot by 7 foot Low Speed Wind Tunnel showed a very large correlation between yawing moment and side force and also that the side force coefficient, which is pressure produced, is much larger than the yawing moment coefficient[33]. Thus it appeared that, on a sphere, measurement of lift and side force would yield just as much information as measurement of pitching and yawing moments. Also, because of the greater magnitude of the side force coefficient, side force measurement could be accomplished with a larger ratio of signal to noise.

Finally, the elimination of the necessity of fitting the balance within a thin disk, coupled with the knowledge gained in the construction and operation of the disk balance, meant that a significantly more accurate and reliable drag force transducer could be devised.

The sphere balance (Figs. 13 and 17) was made up of two units, a drag force transducer and the supporting sting. The lift and side-force transducers were built into the sting.

The drag transducer was a simple one-piece aluminum parallelogram flexure in the form of two parallel rectangular bars connected at their ends by thin strips. One bar was connected to the sting while the other was attached through an aluminum yoke to the Plexiglas sphere. Therefore, the forces acting on the sphere were transmitted to the supporting structure through the thin strip flexures. Four foil strain gages* were bonded to these flexures and wired together in a Wheatstone bridge in such a way that the bridge output voltage was dependent only on the drag force. In operation, the resonant frequency of the drag transducer was 31 Hz.

The lift and side force transducers operate on the cantilever beam principle. The bending moment produced in a simple cantilever by a transverse force at the free end increases linearly with distance along the beam away from the free end. On the other hand, a pure couple applied to the free end of the beam gives rise to a bending moment that is constant along the beam. Thus, if the difference between bending moments at two stations along the cantilever is measured, it is proportional only to the transverse force at the end of the beam, whether or not a pure couple is also present.

The bending moment on the sting was measured at two stations by

---

*Micro-Measurements type MA-13-045AL-350.

mounting a pair of strain gages,[*] one on each side of the sting, at each station. These four gages were wired into a differential bridge, the output of which was linearly proportional to the transverse force acting at the center of the sphere. Two such units, oriented at right angles to one another, permitted measurement of lift and side force.

The sting was a hollow, circular, brass cylinder, the open center being necessary for the lead-out wires from the strain gage circuits. The cross-section of the sting at the strain gage stations was reduced to a square for two reasons.

First, the reduction in cross-section area at the strain sites increased the strain level of the strain gages, yielding greater sensitivity. At the same time the rest of the sting was kept stiff, which made the natural frequency of the sting high enough to allow good frequency response of the unit. Second, provision of flat surfaces on which to cement the gages considerably facilitated the accurate positioning and firm bonding of the gages.

When the sphere unit (model, transducers, sting, and strut) was assembled and submerged, the natural frequencies of the lift and side force transducers were 18 Hz and 8. 5 Hz, respectively. The lower natural frequency of the side force transducer resulted from coupling

---

[*] Micro-Measurements gage number MA-13-062AQ-350.

of sting bending with torsional deflection of the supporting strut.

The lead-out wires from the drag, lift, and side force transducers were carried through the sting and up out of the fluid through a rubber tube fastened to the trailing edge of the strut. As in the case of the disk balance, the sphere balance unit was completely waterproofed with the epoxy compound.

4. Accelerometer

The accelerometer mounted in the amplifier box on the carriage was originally constructed solely as a device on which to develop techniques for handling and installing semiconductor strain gages and with which to study some of their characteristics. When completed, the unit showed an appropriate combination of sensitivity and frequency response to be useful in the experiment, so it was incorporated into the equipment. However, the creeping effect associated with the semiconductor gages (and noted above in the discussion of the disk balance) was observed during the course of the experiment. Shortly thereafter, the accelerometer was damaged, one of the semiconductor gages being destroyed. This necessitated regaging of the unit, which was accomplished with foil gages to eliminate the creeping effect.

Measurement of acceleration was useful for two different reasons in this experiment. First, it provided a measure of the unsteadiness in the carriage propulsion system. The other use was cancellation of that component of the drag balance output which was due to acceleration of the sphere or disk mass when the carriage motion was unsteady. Whenever the carriage was accelerated, the sphere (or disk) and the fluid within it resisted the acceleration with a force equal to the total mass times acceleration. Because it acted along the line of motion, this force was sensed by the drag balance. Consequently, the output voltage from the drag balance was not proportional to drag under these conditions. This situation was corrected by using analog circuits to subtract the proper portion of the accelerometer signal (equal to the inertial force) from the drag balance signal to produce true unsteady drag.

A strain-gaged aluminum cantilever beam, with a lead mass on its free end, was the active element of the accelerometer. Four foil strain gages* were cemented to the beam, two on either side. These gages were wired together in the usual Wheatstone bridge circuit. Figure 18 shows a sketch of the accelerometer, which has a natural frequency of 238 Hz and a sensitivity of approximately $10\mu v/ft/sec^2$.

The accelerometer was mounted so that the beam hung vertically. When accelerated, the suspended mass exerted a transverse inertial

---

*Micro-Measurements type EA-09-050AH-120.

force on the end of the beam, thereby bending it and inducing strains of equal magnitude but opposite sign in the strain gages on opposite sides of the beam.

No attempt was made to damp the motion of the accelerometer beam, so a sharp peak existed in the accelerometer frequency response curve at the natural frequency of the beam. However, the influence of this resonance peak was minimized by passing the accelerometer output through a notch filter (described below).

E. ELECTRICAL EQUIPMENT

1. Amplifier Circuits

Since the output levels of the several strain gage circuits used in this work were on the order of a few millivolts or less, amplification was necessary to bring these voltages up to the magnitude required for recording or display on an oscilloscope. For this reason, and also because several operational amplifiers were required for compensation purposes (e. g. , removing inertial forces from the drag transducer signal, as referred to above) and for correlation and filtering of signals, it was decided to utilize inexpensive solid-state differential operational amplifiers, with appropriate attendant circuits, in the experimental setup. In addition to their very low cost, * these amplifiers possess the attributes of low noise (2 μv rms referred to input), great flexibility, and small size. **

As presently used, the basic solid-state amplifiers are wired into three types of circuits. The various circuit types are all labeled in the overall circuit diagram of Fig. 16. Four amplifiers operate as simple negative-feedback floating-input d. c. gain amplifiers, the gains of which are set by appropriate combinations of input and feedback resistors. These units amplify the output signals from the strain gage transducers.

Several other amplifiers, also operating with negative feedback, are used as unity gain adders. By proper adjustment of the level of several inputs with potentiometers, these amplifiers achieve compensation of the sort noted above. With a single input signal, one amplifier operates as a sign inverter, necessary in the process of summing and differencing two signals mentioned above in the description of the disk balance.

---

*At the time of purchase (mid-1966), the Philbrick PP85AU amplifiers selected cost $17 per unit.

**Five amplifiers and necessary circuitry were mounted in the 2x3x8 1/2 inch amplifier box.

One other amplifier is used in an active notch filter circuit, the design and characteristics of which are fully described elsewhere[72]. The very sharp notch of this filter is set at the resonant frequency of the accelerometer so that, when the acceleration signal is passed through the filter, the resonance component of the accelerometer output is greatly attenuated. This is necessary because of the combined effects of the large resonance peak in the accelerometer response and the fact that this resonance is readily excited by the mechanical vibrations that remain in the carriage towing system. The experimental results are not significantly influenced by this selective filtering due to the relatively high frequency involved. The filter frequency is 238 Hz, while the sphere or disk vortex shedding frequency, the dominant fluid-produced periodicity, is no greater than 5 Hz, almost two orders of magnitude lower.

The d. c. gain amplifier and notch filter circuits are all mounted in the amplifier box on the carriage. Several factors were involved in the decision to locate them there. Because of the great length of wiring between the strain gage transducer circuits and the external signal-handling equipment (approximately 80 feet via the overhead instrumentation cable and back to floor level), considerable pickup of hum and noise by these lead wires was expected. By placing the gain amplifiers very near the signal sources, the effect of these disturbances on the signals of interest was minimized. Another factor involved the construction of the carriage-strut-model assembly, which was such that the carriage was out of balance due to the center of gravity lying outside the V-groove air bearing. To remedy this condition, some additional mass was required near the outrigger bearing corner of the carriage to shift the center of gravity to a position between the bearings. Finally, little penalty was involved in locating the amplifiers on the carriage because they weigh very little and also because the necessary wiring was already present, used by the strain gage circuits.

Power for the amplifiers is provided by +15 vdc and -15 vdc lines from an external source through the overhead instrumentation cable. These voltages are also stepped down with dropping resistors to +3 and -3 vdc to power the strain gage circuits. Outputs from the strain gage transducers are fed directly to the inputs of the gain amplifiers; the amplified signals pass through the overhead instrumentation cable to the external equipment.

The operational amplifiers (summers and sign inverters) are mounted in a box similar to the one on the carriage but are not carried with the moving system. The wiring of these amplifiers is readily changed to provide the specific operations required by the test being performed. These amplifiers use the same ± 15 vdc power as the carriage mounted units.

2. External Units

Three pieces of electronic equipment in addition to those mentioned were generally used in conjunction with the force and moment measurements. These were a two-channel strip chart pen recorder,* a dual-beam oscilloscope,** and a regulated direct current power supply.*** The power supply was actually two identical but independent units in the same chassis, each of which had a floating output. Both outputs were adjusted to 15 ± 0.01 volts. The outputs were wired together to provide +15 v and -15 v, relative to a common ground, to power the amplifier and strain gage circuits.

---

*Moseley Autograf Model 7100B Strip Chart Recorder.

**Tektronix Type 502A Dual-Beam Oscilloscope.

***Trygon Dual Lab Supply DL40-1.

F. FLOW VISUALIZATION EQUIPMENT

The hydrogen bubble flow visualization technique has come into extensive use in hydrodynamic studies over the past several years. It is commonly used for observation of water flows, although Criminale and Nowell[73] recently reported using the technique in aqueous mixtures of up to 40% glycerol.* The many uses and refinements of the method are covered in detail elsewhere[74, 75]; only the application will be considered here. A sketch of the flow visualization equipment is included as Fig. 19.

Because distilled water and glycerol, the two constituents of the working fluid, are very poor electrolytes, the addition of sodium chloride was necessary to permit an adequate rate of hydrogen bubble generation at reasonable voltages, i. e., under 100 vdc. The basic glycerol-water mixture produced no noticeable bubbling even with 200 volts potential difference between anode and cathode. Only a small concentration of salt was required, typically 0.05-0.10% by weight of solution.

---

*To the author's knowledge, the experiment reported here marks the first application of the hydrogen bubble technique to high-concentration (>50%) glycerol mixtures.

Originally, the platinum bubble-generating wire was stretched between the tips of two insulated brass rods which were fastened to the ends of a plastic strut*. This strut was bolted at its center to the model-support sting in such a way that the wire was positioned ahead of the test body and lay in the horizontal plane which included the sting centerline.

A second wire was later added in the wake of the test body. This wire was actually two wires, the outer ends of which were soldered to the two brass rods supporting the original wire. The inner ends of these wires were attached to a semicircular ring which was, in turn, soldered to a third brass rod running parallel to the sting and fastened to the plastic strut. The semicircular ring was included to permit this second wire to lie in the appropriate plane without interferring with the operation of the sting balance used with the sphere.

Early flow visualization tests with the original bubble generator demonstrated the existence of a serious flow interference problem. Examination of sphere and disk flow photographs indicated that the plastic strut holding the wires had a strong stabilizing effect on the

---

*Bubble-generating wires were either completely bare or insulated in segments to produce streaklines. Commonly used "kinked" wires, made as described by Clutter et al [74] by rolling the wire through a pair of gears, did not work successfully in the highly viscous fluid.

wake because it was close enough to the sphere or disk to penetrate the tail of the separation bubble.

To circumvent this wake interference, a 1/8 in. diameter brass rod bent into the shape of an inverted "U" was employed to position the bubble-generating wire. The cross bar of this wire holder, which was above the fluid surface (see Fig. 19), was fastened to a plastic arm on the carriage. The wire was held in tension at the appropriate depth by the insulated vertical legs of the U-shaped holder.

A wire in the overhead instrumentation cable connected the bubble generator to the grounded negative terminal of a direct current power supply.* The positive terminal of the power source was connected to an aluminum strip attached to one wall of the towing channel below the fluid surface. This strip thus acted as the anode in the electrolysis process.

The sheet of hydrogen bubbles which streamed from the platinum wire as it moved through the fluid was illuminated by a horizontal plane of light over a 6 ft long section of the towing channel. Photo-spot lamps were mounted in aluminum housings on both sides of the towing channel. Light from the lamps in each housing passed through a pair of collimating slits (and a 45° mirror in one housing); the light

---

*Oregon Model A3A Variable Voltage Regulated Power Supply.

sheets so produced shone straight down into the fluid, parallel to the channel walls. These vertical light beams were reflected from mirrors attached to the channel walls at 45° angles, thereby producing a horizontal light sheet which illuminated the bubbles and the sphere or disk. Illumination from both sides was necessary to avoid loss of detail in shadow regions.

Optimum results were obtained when the collimating slits in the lamp housings were adjusted to produce a light sheet that was approximately 1/2 in. thick at the center of the channel. This thickness was required in order that the intensity of illumination be great enough to produce worthwhile photographic results. A thinner sheet would have been more desirable in that it would have reduced the time required for the hydrogen bubbles to rise out of the light sheet. With the 1/2 in. thick sheet, this time was of the order of one hour. Since it was not usually possible to proceed at the leisurely rate of one test run per hour, many of the flow visualization tests suffered somewhat from background scatter caused by bubbles from previous test runs remaining in the light sheet. (This will be evident in some of the results presented in Section IV.)

A Polaroid camera was attached to a frame fastened to the towing channel. The camera position is indicated in Fig. 19; the viewing direction was made as close to vertical as possible without allowing the air bearing to obscure part of the bubble field. One of the event markers in the strip chart recorder was wired to the flash triggering switch in the camera shutter so that flow field photographs could be related to the recorded forces and moments.

IV. EXPERIMENTAL RESULTS

A. EXPERIMENTAL TECHNIQUE

1. Fluid Measurements

Evaluation of the fluid properties needed to reduce the experimental data to coefficient form was accomplished in two ways, the choice of method depending on the type of working fluid in use.

When the channel fluid was water or a simple glycerol water mixture, values of μ and ρ were obtained by interpolation from the tables in reference 67 after T of the fluid had been measured to within 0.1°C with a mercury thermometer. In the case of glycerol water mixtures, the glycerol concentration in each such mixture was determined by measurement of the fluid specific gravity with a pycnometer and an analytical balance.*

Introduction of sodium chloride into the glycerol water mixtures meant that the tables of reference 67 could not be used for μ and ρ, despite the fact that the viscosity of a mixture appeared to be unaffected by the salt addition, because specific gravity measurement was no longer sufficient to determine the glycerol content of the mixture once the salt was added.

Consequently, when a glycerol-water-salt mixture was used,

---

*Hydrometers could not be used for this measurement because of the high fluid viscosity.

ν and ρ of the mixture were carefully calibrated as functions of T, using a Cannon-Fenske Routine Viscometer and a pycnometer, respectively, for the measurements. These calibrations were then used in conjunction with measurement of T of the fluid to determine ν and ρ for each run.

It should be noted that T of the fluid was always measured along the test model path in the channel, as it was found that T could differ by as much as 1°C between this path and the channel walls or fluid surface. Although the viscosity gradients resulting from this variation of T did not significantly affect the test results, accurate reduction of the experimental data required that ν (and therefore T) of the fluid passing over the test model be known as precisely as possible.

2. Balance Calibration and Circuit Adjustments

The sphere and disk balance systems were calibrated by simply hanging various brass weights at appropriate places on a balance and recording the system output on the strip chart recorder. Typical calibrations of the sphere balance are given in Fig. 20; clearly evident is the high degree of linearity of the transducer outputs. Not apparent in the calibration plots, but confirmed in the course of calibration tests, are the lack of interactions between transducers and the ability of the balance to accurately resolve an arbitrary force into its lift, side force, and drag components.

Transducer interactions were not absent in the disk balance and, therefore, several operational amplifiers were required to compensate for these interactions. The calibration and adjustment procedure for this balance became a trial and error cycle of applying weights, reading transducer outputs on the recorder, and adjusting the various potentiometers in the circuit (Fig. 16) to correct for the interactions that occurred. Although it was not possible to completely eradicate transducer interactions in this manner, the reduction achieved in degree of interaction was sufficient to permit reasonably accurate measurement of P and Y (to within 10 %).

To eliminate the force due to test body inertia from the drag measurements, the following technique was employed. The test body was filled with the working fluid and mounted on the carriage in its proper orientation, but in such a manner that the body was not submerged. The carriage was then accelerated up and down the track with the appropriate potentiometer being adjusted until no drag force was indicated on the recorder.

3. Operation of the Experiment

Once the calibrations and fluid property measurements had been performed, operation of the experiment was straightforward. After allowing at least 1/2 hour for the electronic equipment and strain gage transducers to warm up to thermal equilibrium, the remaining equipment was activated (air bearings, chart recorder, voltage on bubble generator, and flow visualization lights). The actual test run was controlled entirely from the drive motor, which was manually operated. This was done to avoid the possibility of accidentally damaging the strain gage balances.

When the flow visualization equipment was being used, test runs were made at night, since normal daytime light in the building provided far too much background illumination in the channel. This background light was intense enough that, even on a cloudy day, the light reflected from the hydrogen bubbles was indistinct to the eye and did not register at all on film. Even at night and with high-speed Polaroid film,* an exposure duration of 1/30 second at the maximum camera aperture (f/4.7) was required to produce a worthwhile photograph. This meant that run speeds had to be restricted to approximately one foot per second or less, because at higher speeds the photographic image became too blurred to be meaningful.

Since the camera shutter was tripped manually, the experiment generally required two operators when flow visualization studies

---

*Polaroid Polascope, with an equivalent ASA speed of 10,000.

were made, the second operator handling the camera and also acting as observer at the flow visualization section of the channel.

Upon completion of a test run, the carriage was backed up to the starting position and a period of 10-15 minutes was allowed to elapse before another test run was begun. This was done to permit the fluid disturbances to die out.

4. Data Reduction

Quantitative data for a test run consisted entirely of the traces on the strip chart record. Frequencies and magnitudes of forces and moments were measured on the strip chart and converted to the appropriate dimensions through use of the calibration data. Velocity was measured, either from the slope of the x-t trace if the position-indicating potentiometer was used, or from the period of the event marker pips if the microswitch on the cable drive pulley was in use. The values of U, ν, and ρ were used then to reduce the data to dimensionless coefficient form.

B. RESULTS OF SPHERE EXPERIMENTS

1. Sphere Drag

a. Steady Drag. Steady sphere drag was measured through most of the range $5 < Re_d < 120,000$. This data, reduced to coefficient form (C_D versus Re_d), is plotted in Fig. 21. The solid curve in Fig. 21 is a mean curve drawn through the data of Fig. 7. The general overall agreement between the data from these tests and the previously existing data serves both to corroborate the existing data and to indicate the accuracy of the system used for the tests reported here.

The greatest data scatter occurs at high subcritical Re_d (5500 to 120,000), where it also appears that the C_D values are consistently higher than the curve. Two comments regarding the data in this range are pertinent.

First, the actual spread of the C_D - Re_d data through which the curve of Fig. 21 was drawn is worth noting. This data spread is evident in Fig 7. When the data of Fig. 21 is compared directly with that of Fig. 7, most of the points fall within the band of data points in Fig. 7.

The second point to be noted is the fact that almost all of the data in this Re_d range was obtained in what amounted to a shakedown test of the experimental apparatus. A great deal of mechanical unsteadiness existed in the system at that time, resulting in drag force records that were difficult to evaluate with accuracy, particularly at the lower Re_d values in this range. The experience gained in this early testing led to considerable refinement of the experimental equipment.

Tests in this Re_d range with the refined apparatus would yield results with much less scatter. However, such tests have not been performed because attention was focused on lower Re_d (< 1000), chiefly because the flow unsteadiness at lower Re_d is more regular.

Some scatter also exists in the rest of the data ($Re_d < 2000$), although no consistent deviation from the curve is evident here. An interesting feature of this data is the greater consistency of points for $400 \leq Re_d \leq 2000$. Data in this range was obtained solely with the balance designed specifically for the sphere, whereas the rest of the data in Fig. 21 came from tests with the sphere mounted on the disk balance. It became very evident in the course of these experiments that the disk balance was not as capable of producing repeatable drag results as was the sphere balance. To some extent this is attributable to the interactions among the tranducers in the disk balance. Another factor was the nonlinearity of the disk drag transducer at drag loads greater than about 0.45 pound.*

b. Unsteady Drag. The principal result of the attempt to study the unsteady component of drag during steady sphere motion is that it is very small. In all cases the unsteadiness in the measured drag was no more than about 5% of the total drag, regardless of whether or not vortex shedding occurred. This, of course, does not include

---

*Wall effects were not studied directly; however, the close agreement of the drag results with existing data led to the conclusion that such effects were negligible.

the early stages of wake buildup, where large drag fluctuations sometimes existed. The magnitude of the first two or three fluctuations depended greatly on the acceleration imparted to the sphere at the start of a run. In general, more nearly impulsive starts produced greater fluctuations.

Once the sphere wake had built up to its quasi-steady configuration (usually after two or three cycles of vortex shedding), the drag unsteadiness remained small and did not demonstrate a clear relationship to the vortex shedding process. Figure 22 is a copy of the drag and side force recorded during a typical test run at $Re_d = 532$.* Despite the large (though irregular) fluctuations in side force, which indicate vigorous unsteadiness in the sphere wake, very little related unsteadiness appears in the drag record. In fact, the variation in drag is small enough that it may be due entirely to mechanical unsteadiness in the experimental apparatus. Other run records have been obtained which display even less drag fluctuation (at similar Re_d) than exists in Fig. 22.

A noteworthy feature of the data record in Fig. 22 is the gross difference in the nature of the development of unsteadiness in drag and side force. The drag force had built up to its maximum value and

---

*It should be pointed out that high frequency oscillations attributable to mechanical unsteadiness were smoothed out in the process of tracing all data records presented in this paper.

passed through three cycles of oscillation before the side force built up into its first (and largest) significant peak. This feature, a characteristic of all data records in which drag was combined with either side force or lift, indicates that the first few cycles of vorticity shedding in the sphere wake are nearly axially symmetrical and are apparently unrelated to the lateral wake oscillations which develop later in the process of vortex loop shedding.

c. Drag During Acceleration. For the purpose of studying acceleration effects, a number of test runs were made wherein the carriage was disconnected from the towing cable and attached instead to a long rubber band, the other end of which was fastened to the track system. The carriage was then drawn back along the track, held in place against the tension in the rubber band until the channel fluid became still, and then released, with drag and acceleration being recorded during the ensuing run. A data record from one such test run is given in Fig. 23.

The run which produced the record of Fig. 23 was made in water so that high Re_d was reached: the maximum value of Re_d, corresponding to the instant when the acceleration trace passed through zero, was 66,000. Velocities at several instants were determined by graphical integration of the acceleration record. Re_d values were computed from these velocities and used to obtain appropriate C_D values from Fig. 7, these in turn being used to calculate the D values making up the dotted curve in Fig. 23. As may be seen, the measured drag is closely approximated by the "steady-state" drag curve except at three points.

By far the most interesting of the three points of difference is the one at startup of the run, where a non-zero flat spot occurs in the measured drag. The constant value of D existing during this initial portion of the run, where the acceleration is also essentially constant, is within 3% of the D value computed according to the apparent mass concept discussed in Part B. 4. of Section II. Nearly identical results were obtained from several other test runs in which a_{max} varied from 3.0 to 6.4 ft/sec^2; calculations of sphere displacement revealed that the sphere travelled a distance approximately equivalent to one sphere diameter before the wake had grown large enough to destroy the potential flow about the sphere.

An important comparison can be drawn between the above result and theoretical calculations of the flow about an accelerated sphere. Although no such calculations have been made for the case of constant acceleration, Chow[76] recently studied the flow past an impulsively started sphere. Using the method of matched asymptotic expansions in a boundary layer type of analysis, he determined that, at high Re_d, flow separation would appear at the rear stagnation point on an impulsively started sphere after the sphere had travelled 0.21 of a diameter.

A more correct comparison can be made by considering the corresponding results for a circular cylinder: calculations[21, p. 214 and p. 221] show that separation on a cylinder occurs after a travel of 0.26d for constant acceleration from rest compared to 0.16d for an impulsive start. If it is assumed that the result for constant acceleration of a sphere bears the same relationship to the impulsive-start result as exists in the case of the cylinder, Chow's result scales up to 0.34d for the distance covered by a constantly accelerating sphere before separation appears. Since the sphere travels 1d before the apparent mass concept becomes invalid, it is evident that considerable growth of the separation bubble must occur before the pressure distribution about the sphere becomes significantly different from the potential flow pressure distribution.

Similar acceleration tests were attempted in a glycerol-water mixture which reduced the maximum value of Re_d to about 300, but the low values of Re_d existing during the early stages of these test runs meant that the vorticity about the sphere diffused so rapidly that no period of potential flow could be observed. Also, incorrect drag compensation precluded the type of drag comparison shown in Fig. 23.

The other two points at which the measured and calculated D values in Fig. 23 differ significantly are probably related to the shedding of vortices in the sphere wake. This would correspond to the measurements by Schmidt[50] of the velocity of a sphere dropped from rest in a vertical column of fluid. He found that fluctuations in sphere velocity during acceleration coincided with the shedding of vortex loops.

A similar phenomenon occurred during startup of most of the normal sphere drag test runs: the drag force measured during a rapidly-started drag test would exceed, or "overshoot", the steady value. Some drag overshoot is evident in the low Re_d drag record of Fig. 22, but the effect was much more pronounced in high Re_d runs, where the overshoot was as much as 30% above the steady drag.

Corresponding phenomena for impulsively-started circular cylinders and flat plates were recently studied by Sarpkaya[77]. Flow visualization enabled him to relate the drag overshoot to the growth and shedding of the initial vortex.

What probably happens is that, when the sphere is put into motion very rapidly at high Re_d, vorticity is slow to diffuse and, therefore, accumulates rapidly in the growing separation bubble behind the sphere. Although this bubble of trapped vorticity soon reaches unstable proportions, the growth of the bubble is so rapid that the bubble becomes much larger than its steady-state size before instability succeeds in causing a vortex loop to be cast into the sphere wake. During this period the pressure drag on the sphere rises above its steady value both because the separated flow area is temporarily larger than it should be and because the enlarged wake bubble forces the outer flow aside, reducing the base pressure below its eventual steady value.

2. Transverse Force on a Sphere

Transverse forces (lift and side force) acting on a sphere constrained to rectilinear motion were studied at values of Re_d up to 2000. In general, the results of these tests serve only to provide order of magnitude estimates of forces and frequencies. The principal factor behind the lack of consistency in these results was flow interference produced by the structure employed to support the sphere. The extent of the flow interference effects will become evident in the discussion of the test data below.

The conventions for lift (L) and side force (S) used in this discussion are indicated in Fig. 24.

a. Magnitude of the Force. Magnitudes of the transverse forces measured in these tests are shown in Fig. 25. Although normal practice is to use the root-mean-square coefficient form to present data of this nature, these results are given in peak-to-peak coefficient form ($C_{F_{PP}}$) for two reasons. First, the test runs were of such short duration that meaningful time averages of the transverse force could not have been obtained in most cases. Consequently, the strip chart records were analyzed to provide this data. Then, because the data records for L and S were generally quite irregular, it was not possible to directly reduce the peak-to-peak measurements to root-mean-square values. Only occasionally did anything approximating a sine wave appear in the L and S data records.

It should be noted that the coefficient values plotted in Fig. 25 are for the total transverse force rather than for L or S alone. Willmarth and Enlow[33], as noted in Section II, found that $\sqrt{\overline{C_L^2}} \cong .062$ at super-critical values of Re_d. Comparing this number with the data in Fig. 25, it is apparent that the nondimensional transverse forces are weaker by a factor of three or four at these low Re_d.

Where it could be determined, the dimensionless frequency of the transverse force was calculated; these values are noted in Fig. 25. The data appears to indicate that the stronger force fluctuations are associated with lower frequencies.

b. Frequency of the Unsteady Force. Many test runs were made in which L and S were not both recorded. Although values of $C_{F_{PP}}$ could not be determined from such runs, it often was possible to measure the frequency of L or S alone. As a consequence, frequency data is more abundant than is the force data. All dimensionless frequency (f*) data obtained with the sphere is plotted against Re_d in Fig. 26. For comparison, the results of Kendall's[28] hot wire experiments are shown, as are the results of the falling-sphere tests performed by Magarvey and Bishop[22, 25].

As was the case with the $C_{F_{PP}}$ data, this frequency data, taken as a whole, makes little sense. In addition, the data subset that seems most consistent, that obtained with the side sting, can not be considered as truly representative for reasons to be discussed below.

Much of the scatter in the data can be explained by two features evident in the original data records. One of these features was the fact that whenever a very low frequency ($f^* < .05$) appeared in a data record, a higher frequency fluctuation was superimposed on it, although the higher frequency could not always be determined because of irregularity in the record. Figure 27 is a reproduction of a data record in which this low-frequency phenomenon appeared. Because the wave-length of these low-frequency oscillations was a large fraction of the total run length, it was not possible to investigate this phenomenon in any detail.

The second feature noted in a number of data records at Re_d above 500 was a breakdown of regular L and S oscillations (with f^* in the vicinity of 0.15) into irregular fluctuations at roughly half the original frequency. The end of the L record in Fig. 28 illustrates this. Although the evidence was not conclusive, this phenomenon was taken to indicate a transition from strictly planar vortex loop shedding into a helical mode of shedding. In this connection it is worth recalling the work of Preukschat[53] noted in Section II, in which he noted that the unsteady motion of a freely rising sphere was invariably two-dimensional at first, but often evolved into a helical motion after a few cycles.

Because of the effect of these two phenomena on the frequency data, it is justifiable to consider the group of data points above fd/U = .12 in Fig. 26 as being most reliable. If this is done, it is apparent that the data defines a smooth curve joining the high and low Re_d data given by Kendall[28].

c. Flow Visualization Results—Sting Interference. The minimum Re_d for flow unsteadiness to occur, sometimes termed the lower critical Re_d, varied with the sting orientation. Early tests with the short sting in its normal position aft of the sphere indicated a value of 290 for $Re_{d_{min}}$. This unexpectedly high value, combined with the fact that the unsteady transverse forces were quite irregular when they did occur, was somewhat of a puzzle at first (recalling the discussion of sphere flows in Section II).

Since it was already known at this point that the Plexiglas bar originally used to hold the hydrogen bubble wire had profoundly stabilized the sphere wake through its interference with the tail of the separation bubble,* the possibility existed that the supporting strut was stabilizing the wake and preventing the regular shedding of vortex loops. As can be seen in the flow visualization photograph of steady flow ($Re_d = 269$) in Fig. 29a, the leading edge of the strut was indeed in close proximity to the tail of the separation bubble.

To test this hypothesis, then, a 15 in. extension was added to the sting. However, repetition of the short-sting tests produced nearly identical results. The correct solution to the puzzle was discovered after one of these tests when the strip chart recorder was inadvertently left on while the carriage was being backed up to its starting position. The resulting data record showed a very regular oscillating transverse force. The obvious conclusion was that the sting itself, an inherent part of the experimental apparatus, was interferring with the sphere wake flow.

The existence of significant sting interference was proved in a series of test runs in which the sphere was removed from the strut-sting support, weighted, and suspended from the carriage by two threads. Flow visualization tests with this setup revealed vortex loop shedding with a high degree of regularity. In addition, $Re_{d_{min}}$ in the absence of sting interference was found to be approximately 215.

---

*With the Plexiglas bar in place, one test run at $Re_d = 500$ produced no noticeable unsteady transverse force!

Photographic results from several of the flow visualization tests with the suspended sphere are presented as Fig. 29b, 30, and 31. Figure 29b is a photograph from a test run at $Re_d = 192$.* The flow was steady and, except for the difference in length of the separation bubble, appears very similar to the flow in Fig. 29a.

Figure 30 is a sequence of three flow photographs, taken at the same position along the towing channel, illustrating the rolling up that occurred in the sphere wake when vortex loops were being shed in the L (lift) mode (i. e. the loops were being alternately shed toward and away from the camera, which was looking down into the channel). The Re_d for this test run was 295.

Visual observation during this (Fig. 30) and other runs with the suspended sphere at low Re_d disclosed the fact that most of the wake activity stems from the tail of the separation bubble, rather than from the vicinity of the sphere itself. The tail of the separation bubble appeared to pulsate longitudinally. Whether the bubble was actually stretching and shrinking or simply oscillating laterally into and out of the light beam is not known. It is interesting to recall that Taneda [20] also observed this pulsation, but as he, too, used a sheet of light

---

*The random bright streaks appearing in this and several other flow visualization photographs are produced by hydrogen bubbles remaining in the illuminated region from previous test runs.

to illuminate a plane through the wake, the question is not resolved. It was very evident, however, that at low Re_d the vortex loops that were carried into the sphere wake were drawn out from the tail of the separation bubble.

This explains why the presence of the sting had such a profound effect on the wake unsteadiness. By tying down the tail of the wake bubble through the no-slip condition at the sting surface, the sting prevented oscillation of the tail of the wake bubble and thereby hindered the process of vortex loop shedding. The separation bubble had to become more unstable than it would have been in the absence of the sting to overcome the damping effect of the shear stresses at the sting surface, and consequently $Re_{d_{min}}$ was raised above its normal value.

Vortex loop shedding in the S mode is clearly in evidence in Fig. 31, a flow visualization photograph taken during a run at $Re_d = 377$. Here the lateral oscillations of the wake were somewhat more pronounced than if the sphere had been rigidly held because the sphere was free to sway from side to side in response to the transverse forces produced by the vortex shedding.

In contrast to the very evident vortex loop shedding of Fig. 30 and 31 are the flow photographs in Fig. 32, taken during a run with the short sting at $Re_d = 332$. Also included in Fig. 32 is a portion of the data record from this run, showing a high degree of regularity compared with most of the test data. The first photograph, taken at the point indicated on the data record, is nearly identical with the steady flow photograph of Fig. 29a. Closer inspection reveals a slight curvature of the wake behind the strut and an apparent thickening on the lower side of the separation bubble. The second photograph is of the same section of the towing channel at a later time and shows the distortion of the wake by the shedding process. In spite of the magnitude of the unsteady side force (close to 20% of the magnitude of D), the wake appears relatively calm and displays no evidence of discrete vortices. This absence of clear, distinct vortices was characteristic of all the flow visualization tests with the sting-supported sphere.

One other data record is included here as Fig. 33. This run, at an Re_d of 715, is presented to illustrate the high degree of irregularity normally demonstrated by the transverse forces at higher values of Re_d. Clearly, it was impossible to obtain reliable frequency and force level data from such data records as this.

Because vortex loop shedding was never clearly evident in the tests of the sting-mounted sphere, firm conclusions could not be drawn regarding the relationship between the unsteadiness in the wake and the unsteady forces. However, it was possible to obtain some insight into this relationship by studying the data from the few flow visualization test runs in which the fluctuations in S were relatively regular.

Considering Fig. 32, for example, it can be seen that two events occurred simultaneously when the sphere was about five diameters back from its position in the first photograph: the sphere wake was deflected slightly toward the top of the photograph, and S passed through a negative peak, corresponding to a force acting toward the bottom of the picture. This suggests that whenever the separation bubble behind a sphere shifts laterally away from the wake axis, a transverse force acts on the sphere in the opposite direction. Although the evidence is not very strong, it also appears that the magnitude of the transverse force depends directly on the extent of the lateral deflection of the separation bubble.

This relationship between wake fluctuations and the transverse force can be explained quite simply. When the separation bubble moves to one side of the wake axis, as in Fig. 34, it retards the fluid flowing past that side of the sphere and accelerates the flow on the other side, producing what can be thought of as circulation (Γ) about the sphere. This circulation moves around the sphere away from that side of the sphere toward which the separation bubble has shifted. The interaction of Γ with the mean flow produces the transverse force. Evidently the magnitude of Γ , and therefore the magnitude of the transverse force, is proportional to the deflection of the separation bubble.

d. Side Sting Results. Once it had been definitely established that the presence of a sting exerted a profound influence on the sphere wake, other means of supporting the sphere were sought in an effort to obtain meaningful data on the unsteady flow. The tests with the sphere suspended on threads have already been noted. However, as it was not possible to obtain unsteady force data with the suspended sphere, several test runs were made with the sting-mounted sphere held perpendicular to the direction of motion. That is, the sting was removed from the strut and attached directly to the carriage so that it hung down vertically.

These tests yielded very regular oscillating L data; magnitudes and frequencies of the L oscillations are indicated in Fig. 25 and 26 respectively. In spite of the regularity of the L oscillations and the fact that $Re_{d_{min}}$ for this configuration was only 220, flow visualization tests failed to reveal any clear indication of vortex loop shedding. Two photographs from one such test at $Re_d = 304$ are shown in Fig. 35; the only distinct feature observed in this and the other tests was a strong upward flow in the wake, indicated by the bright-edged dark streak in the first photograph. (The dark streak resulted from the upflow carrying the hydrogen bubbles out of the light beam.) This upflow was evidence that the side sting produced a serious disturbance in the flow about the sphere. The extent of this disturbance became apparent with the calculation of average lift coefficients ($\overline{C}_L$) for several of the side sting test runs. For $270 < Re_d < 550$, values of $\overline{C}_L$ ranged from -.18 to -.14. The upflow in the sphere wake suggested the existence of flow circulation about the sphere; the negative values of $\overline{C}_L$, meaning that the lift force acted downward, confirmed this idea.

C. RESULTS OF DISK EXPERIMENTS

1. Disk Drag

a. Steady Drag. Coefficients of steady drag for a circular disk were measured through most of the range $5 < Re_d < 70{,}000$. The results of these measurements are given in Fig. 36, where they are compared with a curve that represents the data of Fig. 8. The most obvious feature of Fig. 36 is the disagreement between the new data and existing data for $100 < Re_d < 1000$. This lack of agreement stems from the fact that all previous data in this Re_d range was obtained with disks that were free to oscillate, whereas the disk used in the tests reported here was rigidly constrained to one-dimensional motion. The cause of the increase in C_D due to oscillation of a disk is not understood, but may lie in the ability of the disk to generate lift when it executes translational oscillations.

Another interesting feature of the data in Fig. 36 is the rather abrupt flattening out of the curve indicated by the data at Re_d slightly below 200. This phenomenon cannot as yet be explained, but the fact that $Re_{d_{min}} = 160$ for the one-degree-of-freedom disk is probably involved.

The primary factor in the general scatter of the data is the rather poor repeatability of the disk drag transducer; this was pointed out above in the discussion of sphere drag results.

As was the case with the sphere, the disk drag results for $9000 \leq Re_d \leq 70,000$ were obtained early in the course of the research. Considerable mechanical unsteadiness existed in the experimental apparatus at the time, and this showed up in the drag measured during these early tests. The resultant uncertainty in the determination of D is responsible for the values of C_D being a bit high.

The C_D data at low Re_d also appears high in comparison with the curve in Fig. 36. However, a look at Fig. 8 reveals that the existing data in the range $0 < Re_d < 50$ is not extensive, and so it is believed that the data presented here is essentially correct.

b. Unsteady Drag. The drag data record shown in Fig. 37 is typical of the disk tests. Except for the unsteadiness during the wake development period, very little fluctuation exists in D in spite of the vortex shedding indicated by the oscillations in yawing moment (Y). Analysis of many disk drag data records showed that, during the steady state portion of a test run, the unsteadiness in D never exceeded 3% of D.

2. Moment on a Disk

The moment acting about an axis in the plane of a circular disk was extensively studied in this experiment. Although the data derived from many test runs exhibited considerable scatter, enough consistency appeared that the results are considered to be reliable. In contrast with the sphere results, the uncertainty in the disk data did not seem to be caused by sting interference, but was a result of the fact that in a large number of the tests a steady state was not achieved. This situation will be discussed in the presentation below of specific results.

Sign conventions for pitching moment (P) and yawing moment (Y) are shown in Fig. 38.

a. Magnitude of the Moment. Coefficients ($C_{M_{PP}}$) of the peak-to-peak value of the total moment measured at various Re_d are presented in Fig. 39. The reasons given above for expressing the sphere transverse force results in peak-to-peak form also apply to $C_{M_{PP}}$.

A rather large spread in $C_{M_{PP}}$ values is apparent. However, the two points connected by an arrow give a clue to the cause of this data spread. The two values of $C_{M_{PP}}$ were both taken from the same data record, the high value from early in the test run and the low value from near the end of the run. This decrease in the magnitude of the unsteady moment appeared in almost every run in which regular oscillations occurred, although the variation in magnitude was not generally as severe as these values indicate.

The clustering of data points at $C_{M_{PP}} \approx .007$ in Fig. 39 suggests that this value is approximately correct for the steady state $C_{M_{PP}}$. In comparison, Willmarth, Hawk, Galloway, and Roos[17] reported that $\sqrt{\overline{C_M^2}} = .0047$ for a disk at Re_d between 10^5 and 10^6. Taking into consideration the fact that their moment was measured about a fixed axis and the difference between r.m.s. and peak-to-peak values, it is seen that the dimensionless moment at high Re_d is larger by roughly a factor of three than it is for $Re_d < 500$.

Data in Fig. 39 does not extend above $Re_d = 500$ simply because the moment records have become too irregular to permit a justifiable estimation of the moment magnitude.

b. Frequency of the Unsteady Moment. The frequency of moment oscillations was determined from a number of moment data records. In nondimensional form, this data is plotted in Fig. 40.

At several values of Re_d a pair of data points is connected with an arrow. This serves to illustrate the fact that the frequency, as well as the magnitude, of the unsteady moment decreases during the course of a test run. The individual points on the plot each represent an average value of f* over that portion of a run during which the moment oscillated regularly. Although most of the data is quite consistent, the trend indicated by the arrows raises the question of what the steady-state value of f* should be. The answer to this question has yet to be determined; however, it seems likely that the correct value of f* is approximately .10 for $Re_d < 500$.

The reduction in density of data points for $Re_d > 320$ attests to the fact that the moment fluctuations become increasingly irregular as Re_d increases above 320. Above $Re_d = 500$ the moment records are so irregular that f cannot be determined. Data records for $Re_d < 320$ exhibit very regular oscillations.

Shown on Fig. 40 is $Re_{d_{min}}$ for the disk; its value is 160. This is considerably higher than the accepted value of 100 (noted in Section II). The cause of the discrepancy is not definitely known, but it is probably a combination of sting and strut interference effects. An attempt was made to assess the role of sting interference alone by doubling the sting diameter; $Re_{d_{min}}$ increased only slightly to 175.

c. Flow Visualization Results. Flow visualization tests with the disk provided much insight into the processes of vortex formation and shedding in the disk wake and into the relationship between these processes and the unsteady moments on the disk.

The first disk flow visualization photograph, that in Fig. 41, clearly shows the ring vortex within the separation bubble behind the disk in steady flow at $Re_d = 157$. The close proximity of the tail of the separation bubble to the strut leading edge suggests that some strut interference may indeed have existed.

Figure 42 presents flow visualization results from a test run at $Re_d = 318$ which featured regular vortex shedding in the Y mode (i. e. alternate loop shedding in the horizontal plane). The portion of the wake shown in the photograph was about 12 disk diameters aft of the disk. In contrast with the sphere results, vortices are clearly seen here.

Apparent in the Y data record of Fig. 42 is the decrease in magnitude and frequency of Y during the course of the run. Also evident is a characteristic feature of the disk moment records, the very large moment fluctuation marking the shedding of the first vortex loop of the run. This initial fluctuation was always much greater than the succeeding oscillations.

Vortex loops cast into the disk wake are very strong. That this is so can be seen in two features of the photograph in Fig. 42. One of these features is the considerable difference in the extent to which two successive vortices (center bottom and upper right), shed slightly more than one second apart, have rolled up. The other important feature is the pronounced lateral motion of the vortices.

Regular vortex loop shedding from the disk is demonstrated in the photograph in Fig. 43. The vortices are not as distinct here as in Fig. 42 because, as the moment record shows, the plane of the loop shedding was not horizontal. The fact that the amplitude of the P oscillations fell off rapidly while the Y amplitude remained constant indicates that the loop-shedding plane rotated toward the horizontal as the run progressed.

It should be noted that the photograph in Fig. 43 is somewhat misleading in that it appears to show two vortex loops shed in succession on the same side of the wake axis. This is not the case, of course: there is a vortex loop on the other side of the wake axis, but it is obscured by the strut.

Figure 44 is included here because it illustrates the initial shedding from an almost-impulsively started disk. The intensity of the initial vortex ring generated by the startup of the disk is much greater than that of succeeding vortices. This is not obvious in the photograph, although it is suggested by the rapidity with which the first vortex loop is moving away from the disk axis.

The great intensity of the initial vortex is explained by the following argument. Once the disk is set into motion and flow separation occurs, the ring vortex within the separation bubble must grow to a certain size before instability can set in to start the loop-shedding process. Even after the vortex has reached unstable proportions, however, the instability takes some time to develop. If the growth rate of the vortex is very high, as it is for a rapidly accelerated disk, the intensity of the vortex increases greatly during the time taken for the instability to develop. Since the flow instability is already present when the succeeding vortices are generated, they do not have the extra growth time and consequently are less intense than the initial vortex.

The relationship between the vortex loop shedding process and the unsteady moment can be determined by considering the photograph and the Y record of Fig. 44 together. The first vortex loop to be shed came from the part of the disk nearest the bottom of the photograph; the initial fluctuation in Y was positive, corresponding to a Y vector coming out of the photograph (by the right-hand rule).

This relationship between the moment and vortex shedding agrees completely with the disk flow field model proposed by Willmarth, Hawk, Galloway, and Roos[17]. The key to their model is the idea that the moment is produced by the upstream flow in the center of the wake. A sketch of the model is shown in Fig. 45; it is self-explanatory.

V. CONCLUSIONS

The research program that is the subject of this paper had two principal objectives. The first of these was the establishment of an experimental facility suitable for the study of sphere and disk flows over a wide range of Reynolds numbers; the second objective was the utilization of this facility in an experimental study of the unsteady flows about spheres and disks and the relationships between the flows and the forces acting on these bodies. Both objectives were met: a towing channel was developed and used in conjunction with strain gage equipped models and flow visualization to shed considerable light on the nature of unsteady sphere and disk flows.

Specific conclusions that may be drawn from the results of this research program are listed below.

1. The hydrogen bubble flow visualization technique was successfully adapted for use in glycerol-water mixtures with glycerol concentrations as high as 91%.
2. Sphere drag results for $5 < Re_d < 120,000$ agreed closely with previously existing data.
3. Results for the drag on a circular disk constrained to rectilinear motion reproduced existing data except for

$100 < Re_d < 1000$. In this range the measured drag coefficient for the non-oscillating disk was as much as 50% smaller than that indicated by existing data, which was obtained with oscillating disks.

4. The drag on a sphere or disk moving rectilinearly at constant speed is not significantly affected by vortex shedding in the wake; maximum drag unsteadiness was less than 5% of the total drag on the sphere and less than 3% of the total disk drag.

5. Drag on a sphere accelerated from rest to a constant velocity exceeds the steady state drag by as much as 30% at high Re_d, until vortex shedding becomes established.

6. The potential flow apparent mass concept is valid for the first diameter of motion of a sphere undergoing constant acceleration such that $Re_d \approx 30,000$ when the sphere has moved one diameter.

7. Asymmetrical unsteadiness in the wake of a sphere normally commences at $Re_{d_{min}} \approx 215$; wake stabilization caused by a sting support delayed this unsteadiness until Re_d had reached 290.

8. Wake stabilization caused by a sting raised $Re_{d_{min}}$ to 160 from the value 100 characteristic of unsupported disks.

9. When a sphere or disk was accelerated from rest to a constant velocity, the first vortex loops to be shed were more intense than those shed later; correspondingly, the first fluctuations in unsteady force or moment were greater than later fluctuations.

10. The vortex shedding process in the wake of a sphere was materially impaired by the presence of a sting support; such impairment was not evident in the disk wake.

11. Peak-to-peak values of the total transverse force coefficient for a sphere moving at constant velocity were in the range .02 - .10 for $300 < Re_d < 600$; the dimensionless frequency of the unsteady force in this Re_d range increased with Re_d from .13 to .16. However, further study is required to verify and extend these results in the absence of support interference.

12. The peak-to-peak value of the moment coefficient for a circular disk moving at constant velocity in the direction of its axis was approximately .007 for $160 < Re_d < 500$; the dimensionless frequency of the moment was approximately constant at $f^* = .10$ for these Re_d.

13. The unsteady transverse forces on a sphere result from circulation about the sphere which is caused by lateral fluctuations of the separation bubble.

14. Unsteady moments on a disk are produced when the direction of the reverse flow in the disk wake is shifted during the shedding of a vortex loop.

REFERENCES

1. Cajori, F. Newton's Principia (University of California Press, Berkeley, California, 1946).

2. Torobin, L. B., and Gauvin, W. H. "Fundamental Aspects of Solids-Gas Flow, Part I: Introductory Concepts and Idealized Sphere Motion in Viscous Regime," Can. J. Chem. Eng., Vol. 37, p. 129 (August, 1959).

3. Torobin, L. B., and Gauvin, W. H. "Fundamental Aspects of Solids-Gas Flow, Part II: The Sphere Wake in Steady Laminar Fluids," Can. J. Chem. Eng., Vol. 37, p. 167 (October, 1959).

4. Torobin, L. B., and Gauvin, W. H. "Fundamental Aspects of Solids-Gas Flow, Part III: Accelerated Motion of a Particle in a Fluid," Can. J. Chem. Eng., Vol. 37, p. 224 (December, 1959).

5. Torobin, L. B., and Gauvin, W. H. "Fundamental Aspects of Solids-Gas Flow, Part IV: The Effects of Particle Rotation, Roughness, and Shape," Can. J. Chem. Eng., Vol. 38, p. 142 (October, 1960).

6. Torobin, L. B., and Gauvin, W. H. "Fundamental Aspects of Solids-Gas Flow, Part V: The Effects of Fluid Turbulence on Particle Drag Coefficient," Can. J. Chem. Eng., Vol. 38, p. 189 (December, 1960).

7. Torobin, L. B., and Gauvin, W. H. "Fundamental Aspects of Solids-Gas Flow, Part VI: Multiparticle Behavior in Turbulent Fluids," Can. J. Chem. Eng., Vol. 39, p. 113 (June, 1961).

8. Stokes, G. G. "On the Effect of the Internal Friction of Fluids on the Motion of Pendulums," Trans. Cambridge Phil. Soc., Vol. 9, part 2, p. 8, (1856).

9. Hoglund, R. F. "Recent Advances in Gas-Particle Nozzle Flows," ARS J., Vol. 32, No. 5, p. 662 (May, 1962).

10. Scoggins, J. R. "Aerodynamics of Spherical Balloon Wind Sensors," J. Geophys. Res., Vol. 69, No. 4, p. 591 (February 15, 1964).

11. Scoggins, J. R. "Spherical Balloon Wind Sensor Behavior," J. Appl. Meteor., Vol. 4, No. 1, p. 139 (February, 1965).

12. Scoggins, J. R. "Sphere Behavior and the Measurement of Wind Profiles," NASA TN D-3994 (June, 1967).

13. MacCready, P. B., Jr., and Jex, H. R. "Study of Sphere Motion and Balloon Wind Sensors," NASA TM X-53089 (July 27, 1964).

14. MacCready, P. B., Jr., and Williamson, R. E. "The Motion of Ascending and Descending Spheres," NASA CR-61102 (September 13, 1965).

15. Rogers, R. R., and Camitz, H. G. "Project Baldy: An Investigation of Aerodynamically-Induced Balloon Motions," Cornell Aeronautical Lab. Report No. VC-1912-P-1 (April 1, 1965).

16. Eckstrom, C. V. "Theoretical Study and Engineering Development of Jimsphere Wind Sensor," G. T. Schjeldahl Co. Report (July, 1965).

17. Willmarth, W. W., Hawk, N. E., Galloway, A. J., and Roos, F. W. "Aerodynamics of Oscillating Disks and a Right-Circular Cylinder," J. Fluid Mech., Vol. 27, part 1, p. 177 (January, 1967).

18. Lamb, H. Hydrodynamics (Dover Publications, New York, 1945), 6th ed.

19. Jenson, V. G. "Viscous Flow Round a Sphere at Low Reynolds Numbers (<40)," Proc. Roy. Soc. (London), Ser. A, Vol. 249, p. 346 (January 13, 1959).

20. Taneda, S. "Studies on Wake Vortices (III): Experimental Investigation of the Wake Behind a Sphere at Low Reynolds Numbers," *Rep. Res. Inst. Appl. Mech.*, Vol. 4, No. 16, p. 99 (October, 1956).

21. Schlichting, H. *Boundary Layer Theory* (McGraw-Hill Book Co., Inc., New York, 1960), 4th ed.

22. Magarvey, R. H., and Bishop, R. L. "Transition Ranges for Three-Dimensional Wakes," *Can. J. Phys.*, Vol. 39, No. 10, p. 1418 (October, 1961).

23. Hawk, N. E. Unpublished data.

24. Magarvey, R. H., and MacLatchy, C. S. "Vortices in Sphere Wakes," *Can. J. Phys.*, Vol. 43, No. 9, p. 1649 (September, 1965). This paper contains some very revealing photographs of vortex formation and vortex loop shedding in the wake of a sphere.

25. Magarvey, R. H., and Bishop, R. L. "Wakes in Liquid-Liquid Systems," *Phys. Fluids,* Vol. 4, No. 7, p. 800 (July, 1961).

26. Möller, W. "Experimentelle Untersuchungen zur Hydrodynamik der Kugel," *Physik, Z.*, Vol. 39, No. 2, p. 57 (January 15, 1938).

27. Cometta, C. "An Investigation of the Unsteady Flow Pattern in the Wake of Cylinders and Spheres Using a Hot-Wire Probe," AFOSR-TN-57-760 (1957).

28. Kendall, J. M., Jr. "The Periodic Wake of a Sphere," Jet Prop. Lab., Cal. Inst. Tech., Space Programs Summary No. 37-25, Vol. IV, p. 251 (February 29, 1964).

29. Winny, H. F. "The Vortex System Generated Behind a Sphere Moving Through a Viscous Fluid," Aero. Res. Council R. and M. No. 1531 (September 19, 1932).

30. Schmiedel, J. "Experimentelle Untersuchungen über die Fallbewegung von Kugeln and Schieben in reibenden Flüssigkeiten," *Physik. Z.*, Vol. 29, No. 17, p. 593 (September 1, 1928).

31. Morkovin, M. V., "Flow Around Circular Cylinder —— A Kaleidoscope of Challenging Fluid Phenomena," Symposium on Fully Separated Flows (The American Society of Mechanical Engineers, New York, 1964), p. 102.

32. Fage, A. "Experiments on a Sphere at Critical Reynolds Numbers," Aero. Res. Council R. and M. No. 1766 (September 24, 1936).

33. Willmarth, W. W., and Enlow, R. L. "Aerodynamic Lift and Moment Fluctuations of a Sphere." (To be published).

34. Schiller, L. (ed.) Handbuch der Experimentalphysik (Akademische Verlags., Leipzig, 1932), Vol. 4, (Hydro-und Aerodynamik), part 2 (Widerstand und Auftrieb), pp. 342-345.

35. Maxworthy, T. "An Experimental Determination of the Slow Motion of a Sphere in a Rotating, Viscous Fluid," J. Fluid Mech., Vol. 23, part 2, p. 373 (1965).

36. Arnold, H. D. "Limitations Imposed by Slip and Inertia Terms upon Stokes's Law for the Motion of Spheres through Liquids," Phil. Mag., 6th Ser., Vol. 22, No. 131, p. 755 (November, 1911).

37. Oseen, C. W. "Über den Gültigkeitsbereich der Stokesschen Widerstandsformel," Ark. Mat. Astron. Fys., Vol. 9, No. 16, p. 1 (1913).

38. Goldstein, S. "The Steady Flow of Viscous Fluid Past a Fixed Spherical Obstacle at Small Reynolds Numbers," Proc. Roy. Soc. (London), Ser. A, Vol. 123, p. 225, (March 6, 1929).

39. Liebster, H. "Über den Widerstand von Kugeln," Ann. Physik, Vol. 82, No. 4, p. 541 (February 26, 1927).

40. Maxworthy, T. "Accurate Measurements of Sphere Drag at Low Reynolds Numbers," J. Fluid Mech., Vol. 23, part 2, p. 369 (October, 1965).

41. Allen, H. S. "The Motion of a Sphere in a Viscous Fluid," Phil. Mag., 5th Ser., Vol. 50, No. 314, p. 323 (September, 1900).

42. Wieselberger, C. "Weitere Feststellungen über die Gesetze des Flüssigkeits-und Luftwiderstandes," Physik. Z., Vol. 23, No. 10, p. 219 (May 15, 1922).

43. Shafrir, U. "Horizontal Oscillations of Falling Spheres," AFCRL-65-141 (February 1, 1965).

44. Lunnon, R. G. "Fluid Resistance to Moving Spheres," Proc. Roy. Soc.(London), Ser. A, Vol. 118, p. 680 (April 2, 1928).

45. Allen, H. S. "The Motion of a Sphere in a Viscous Fluid," Phil. Mag., 5th Ser., Vol. 50, No. 316, p. 519 (November, 1960).

46. Shakespear, G. A. "Experiments on the Resistance of Air to Falling Spheres," Phil. Mag., 6th Ser., Vol. 28, No. 167, p. 728 (November, 1914).

47. Millikan, C. B., and Klein, A. L. "The Effect of Turbulence," Aircraft Eng., Vol. 5, No. 54, p. 169 (August, 1933).

48. Flachsbart, O. "Neue Untersuchungen über den Luftwiderstand von Kugeln," Physik. Z., Vol. 28, No. 13, p. 461 (July 1, 1927).

49. Bacon, D. L., and Reid, E. G. "The Resistance of Spheres in Wind Tunnels and in Air," NACA Rept. No. 185 (1923).

50. Schmidt, F. S. "Zur beschleunigten Bewegung kügelformig Körper in widerstehenden Mitteln," Ann. Physik, Vol. 61, No. 7, p. 633 (April 15, 1920).

51. Jones, L. M., Peterson, J. W., Schaefer, E. J., and Schulte, H. G. "Upper Air Density and Temperature: Some Variations and an Abrupt Warming in the Meosphere," J. Geophys. Res., Vol. 64, No. 12, p. 2331 (December, 1959).

52. Sivier, K. R. "Subsonic Sphere Drag Measurements at Intermediate Reynolds Numbers." (Unpublished Ph. D. dissertation, University of Michigan, 1967).

53. Preukschat, A. W. "Measurements of Drag Coefficients for Falling and Rising Spheres in Free Motion." (Thesis for Aeronautical Engineer degree, California Institute of Technology, 1962).

54. Willmarth, W. W. Private communication.

55. Goldstein, S. *Lectures on Fluid Mechanics* (Interscience Publishers, Inc., New York, 1960), p. 46.

56. Bugliarello, G. "La Resistenza al Moto Accelerato di Sfere in Acqua," *Ricerca Sci.*, Vol. 26, p. 437 (1956).

57. Lunnon, R. G. "Fluid Resistance to Moving Spheres," *Proc. Roy. Soc. (London), Ser. A*, Vol. 110, p. 302 (February 1, 1926).

58. Ingebo, R. D. "Drag Coefficients for Droplets and Solid Spheres in Clouds Accelerating in Air Streams," NACA TN-3762 (September, 1956).

59. Selberg, B. P., and Nicholls, J. A. "Drag Coefficient of Small Spherical Particles," *AIAA J.*, Vol. 6, No. 3, p. 401 (March, 1968).

60. Stanton, T. E., and Marshall, D. "Eddy Systems Behind Disks," Aero. Res. Council R. and M. No. 1358 (January, 1930).

61. Michael, P. "Steady Motion of a Disk in a Viscous Fluid," *Phys. Fluids.*, Vol. 9, No. 3, p. 466 (March, 1966).

62. Simmons, L. F. G., and Dewey, N. S. "Wind Tunnel Experiments with Circular Disks," Aero. Res. Council R. and M. No. 1334 (February, 1930).

63. Willmarth, W. W., Hawk, N. E., and Harvey, R. L. "Steady and Unsteady Motions and Wakes of Freely Falling Disks," *Phys. Fluids*, Vol. 7, No. 2, p. 197 (February, 1964).

64. Oseen, C. W. "Über den Widerstand gegen die gleichmässige Translation eines Ellipsoids in Einer Reibenden Flüssigkeit," *Ark. Math. Phys.*, *3rd Ser.*, Vol. 24, p. 108 (1915).

65. Knight, M. "Wind Tunnel Standardization Disk Drag," NACA TN-253 (December, 1926).

66. Shoemaker, J. M. "Resistance of a Fifteen-Centimeter Disk," NACA TN-252 (December, 1926).

67. Anon. *Physical Properties of Glycerine and Its Solutions.* Booklet compiled by the Soap and Detergent Association (available from the Dow Chemical Co.).

68. Shair, F. H., Grove, A. S., Petersen, E. E., and Acrivos, A. "The Effect of Confining Walls on the Stability of the Steady Wake Behind a Circular Cylinder," *J. Fluid Mech.*, Vol. 17, part 4, p. 546 (December, 1963).

69. Neher, H. V., and Leighton, R. B. "Linear Air Trough," *Am. J. Phys.*, Vol. 31, p. 255 (April, 1963).

70. Perry, C. C., and Lissner, H. R. *The Strain Gage Primer* (McGraw-Hill Book Co., Inc., New York, 1962), 2nd ed.

71. Dorsey, J. *Semiconductor Strain Gage Handbook* (Baldwin-Lima-Hamilton Corp., Waltham, Mass., 1965).

72. Cowles, L. G. "The Parallel-T Resistance-Capacitance Network," *Proc. IRE*, Vol. 40, No. 12, p. 1712 (December, 1952).

73. Criminale, W. O., Jr., and Nowell, R. W. "An Extended Use of the Hydrogen Bubble Flow Visualization Method," *AIAA J.*, Vol. 3, No. 6, p. 1203 (June, 1965).

74. Clutter, D. W., Smith, A. M. O., and Brazier, J. G. "Techniques of Flow Visualization Using Water as the Working Medium," Douglas Aircraft Division Rept. No. ES 29075 (April 15, 1959).

75. Schraub, F. A., Kline, S. J., Henry, J., and Runstadler, P. W. "Use of Hydrogen Bubbles for Quantitative Determination of Time Dependent Velocity Fields in Low Speed Water Flows," Rept. MD-10 of the Thermosciences Div., Stanford University Dept. of Mechanical Engineering (February, 1964).

76. Chow, R. "On the Initial Development of Incompressible Flow Past an Impulsively Started Sphere," Grumman Research Department Report Re-317 (January, 1968).

77. Sarpkaya, T. "Separated Flow About Lifting Bodies and Impulsive Flow About Cylinders," AIAA J., Vol. 4, No. 3, p. 414 (March, 1966).

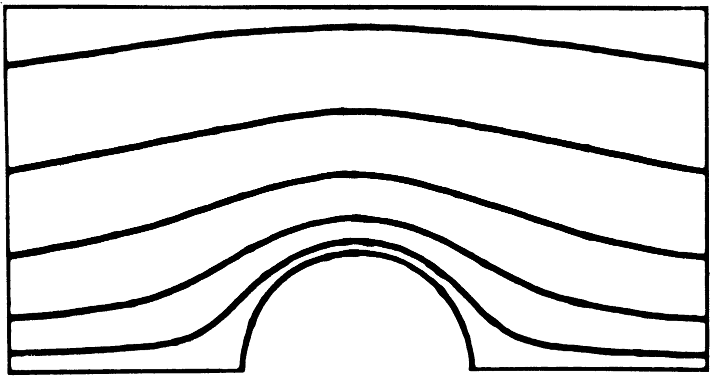

Figure 1. Sphere streamlines for $Re_d \rightarrow 0$.

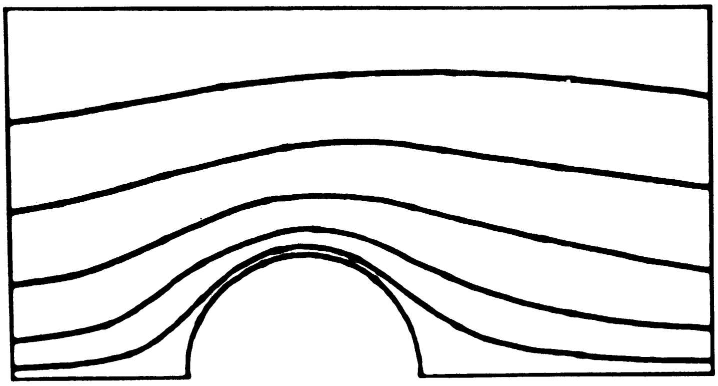

Figure 2. Sphere streamlines for $Re_d = 5$.

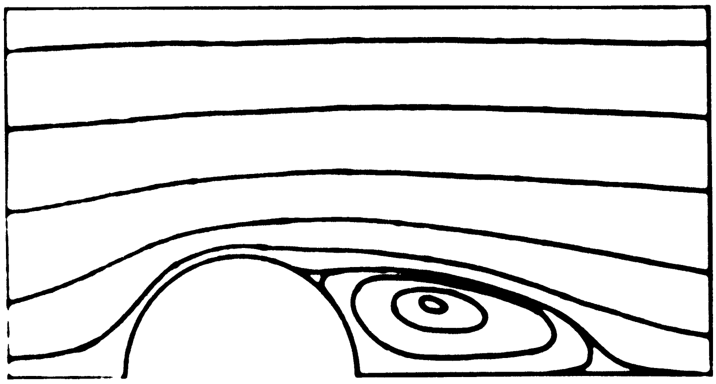

Figure 3. Sphere streamlines for $Re_d \approx 100$.

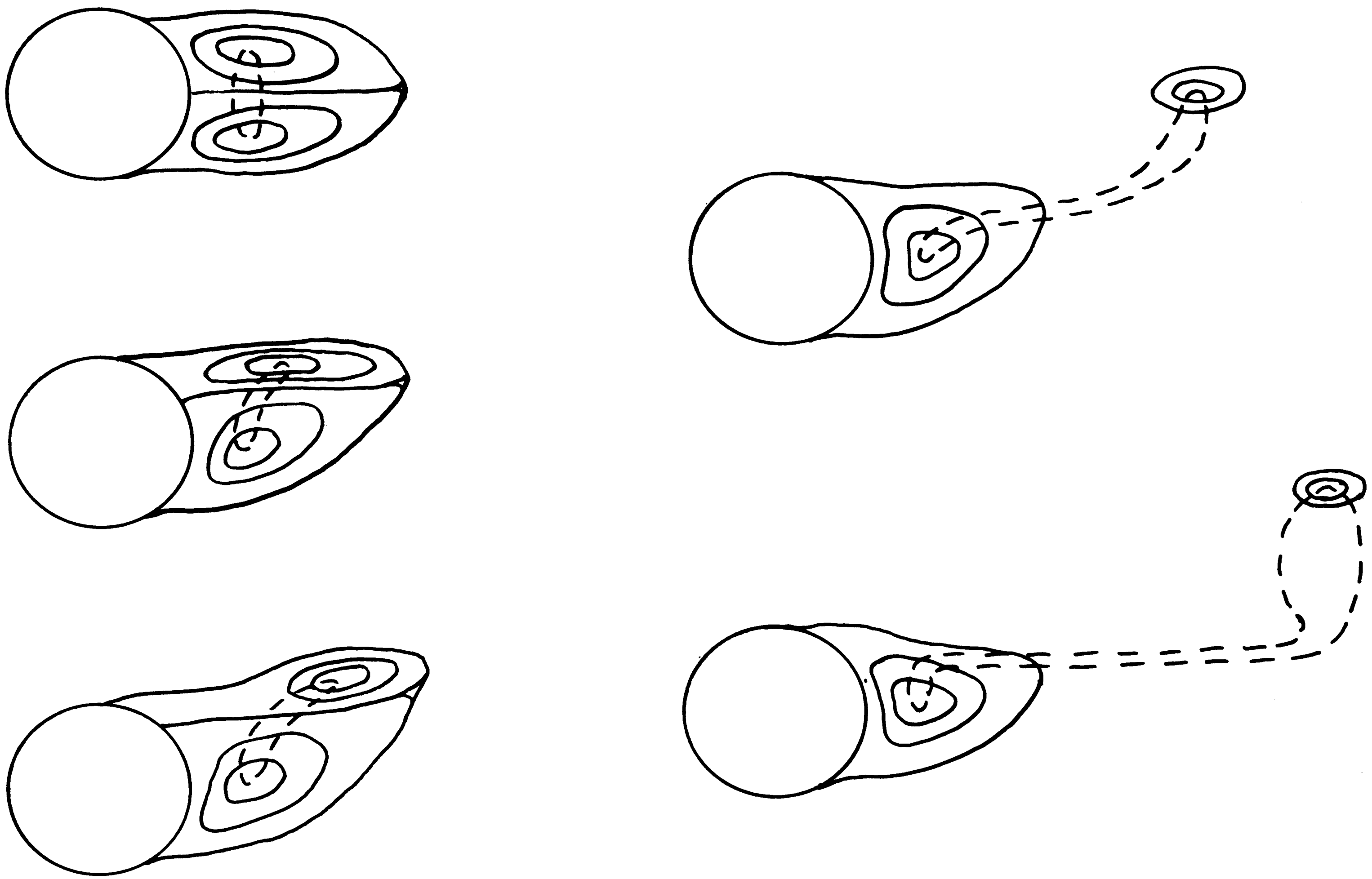

Figure 4. Stages in loop shedding process for a sphere. Wake is shown in cross-section; dotted line indicates position of vortex axis.

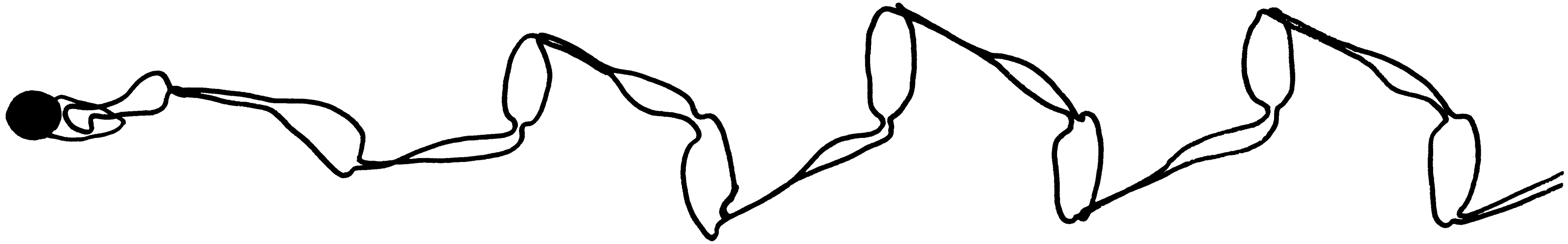

Figure 5. Alternate loop shedding by a sphere at $Re_d \approx 350$.

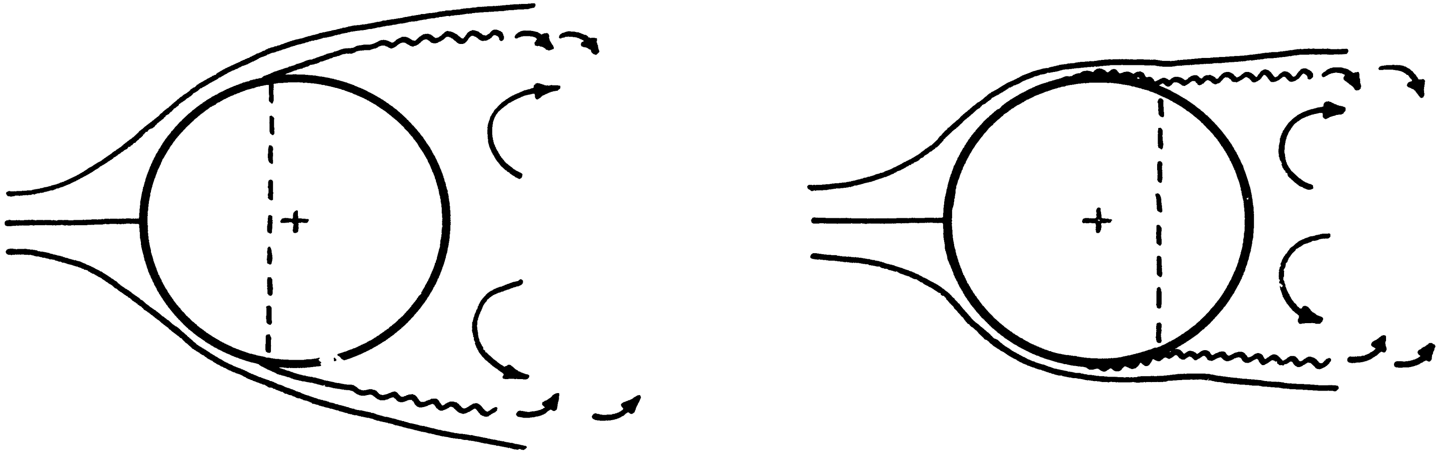

a. Laminar separation.

b. Turbulent separation.

Figure 6. Effect of boundary layer transition on flow separation from a sphere.

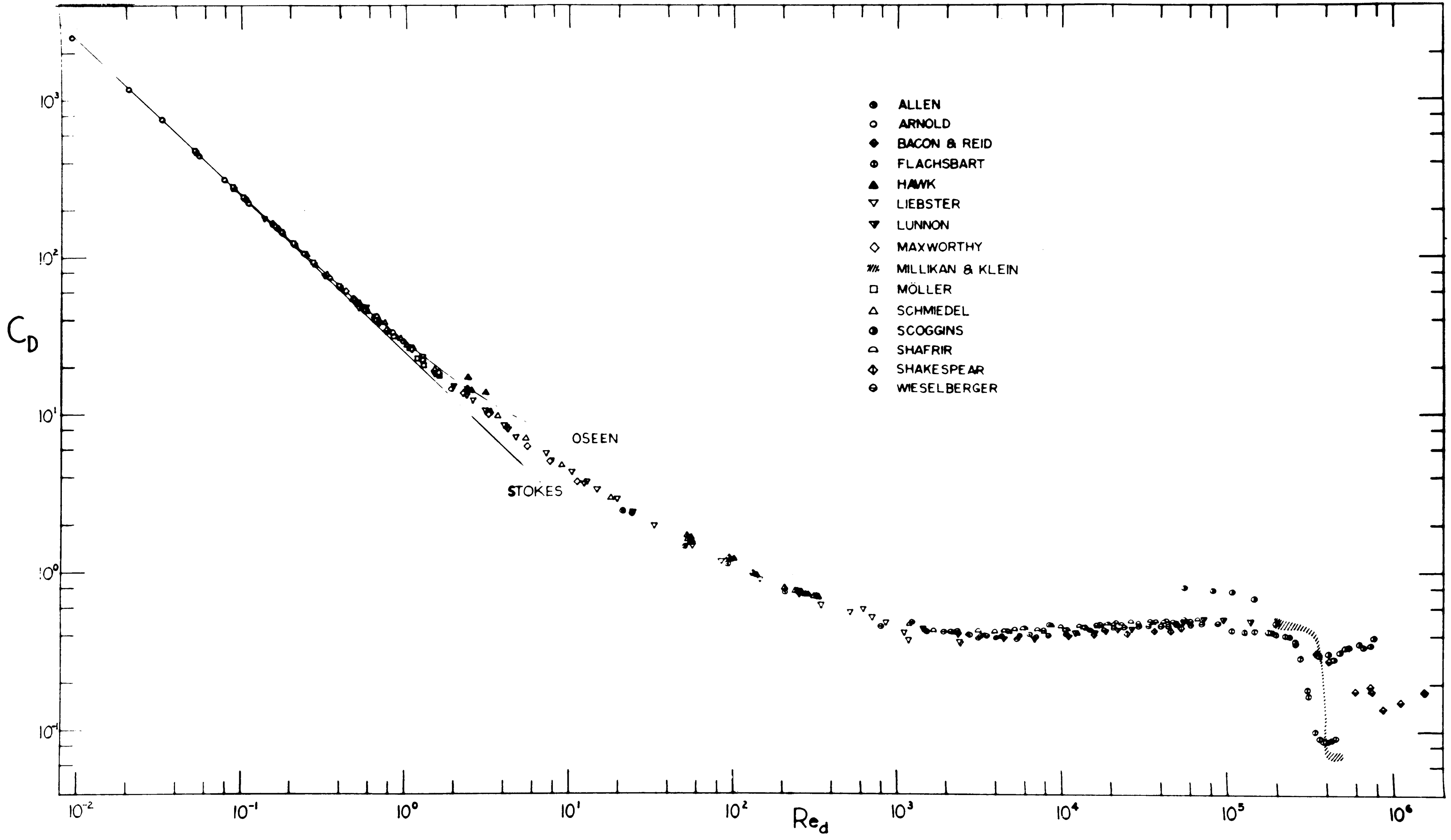

Figure 7. Sphere C_D - Re_d relationship according to existing data.

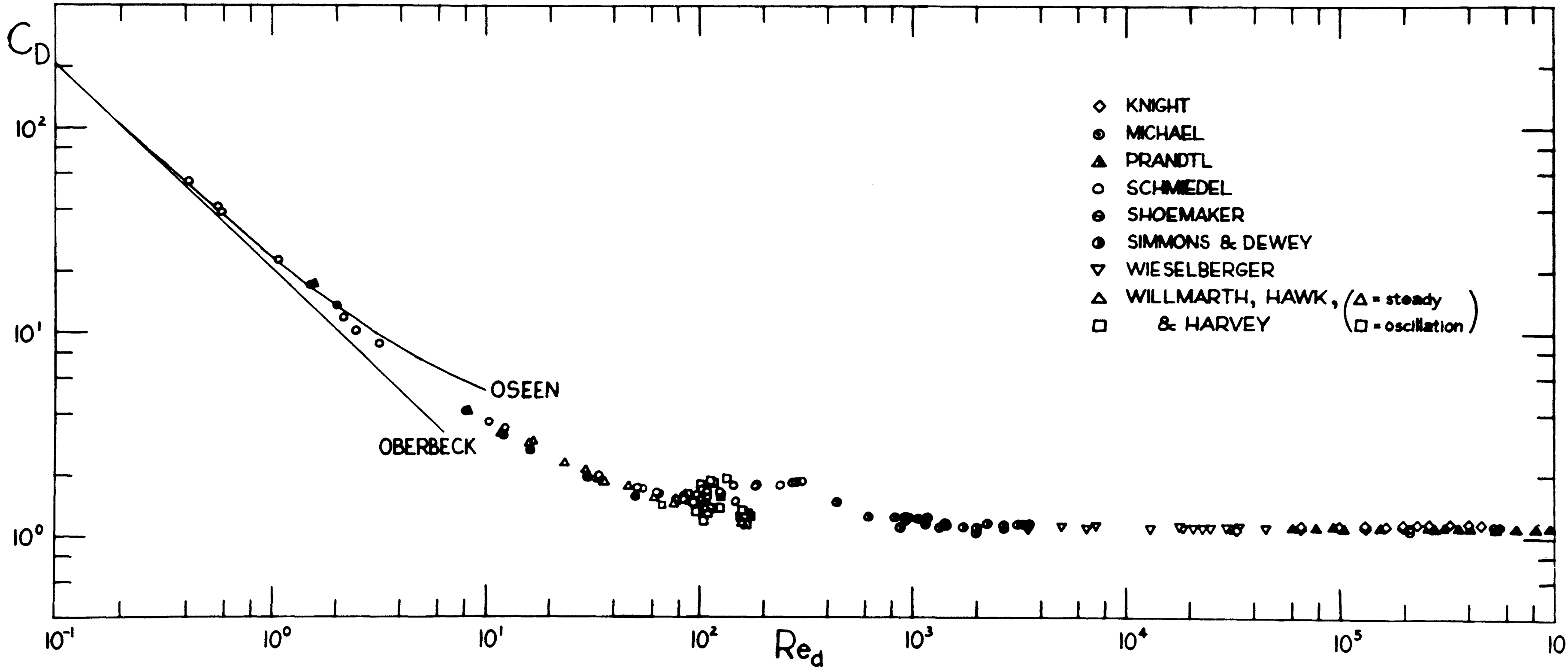

Figure 8. Disk C_D - Re_d relationship according to existing data.

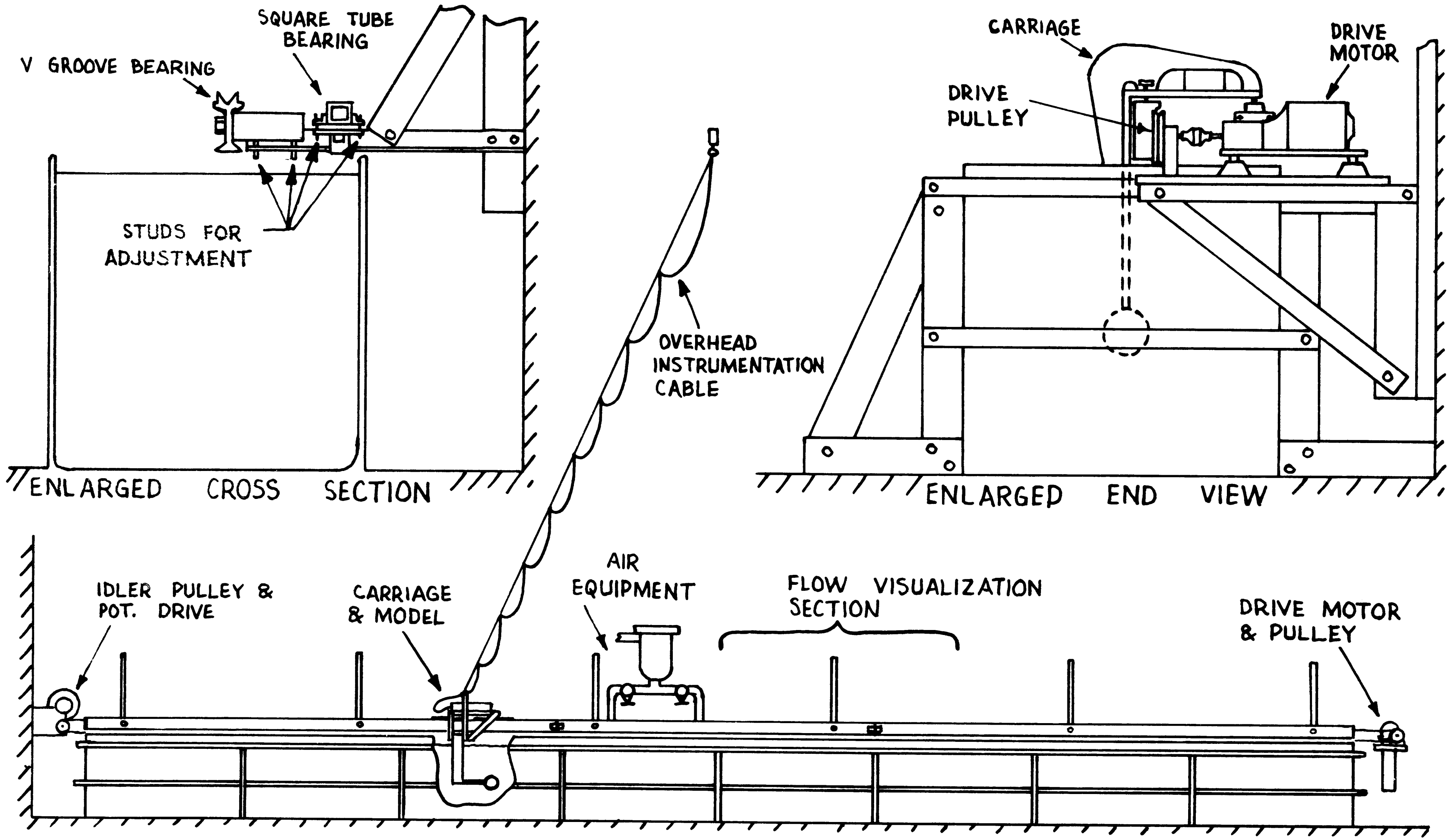

Figure 9. Towing channel installation.

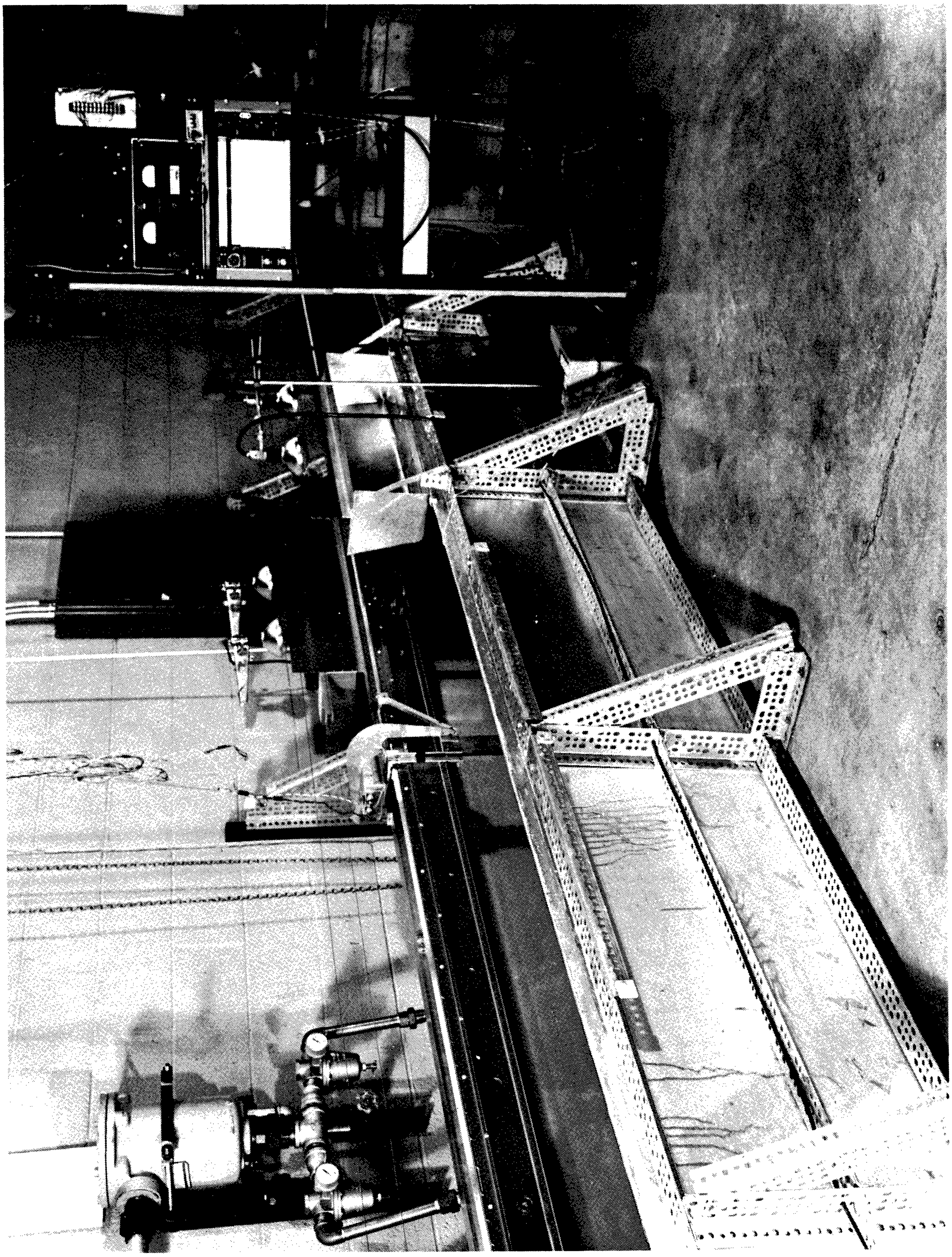

Figure 10. Photograph of towing channel facility.

Figure 11. Photograph of carriage with disk mounted on balance.

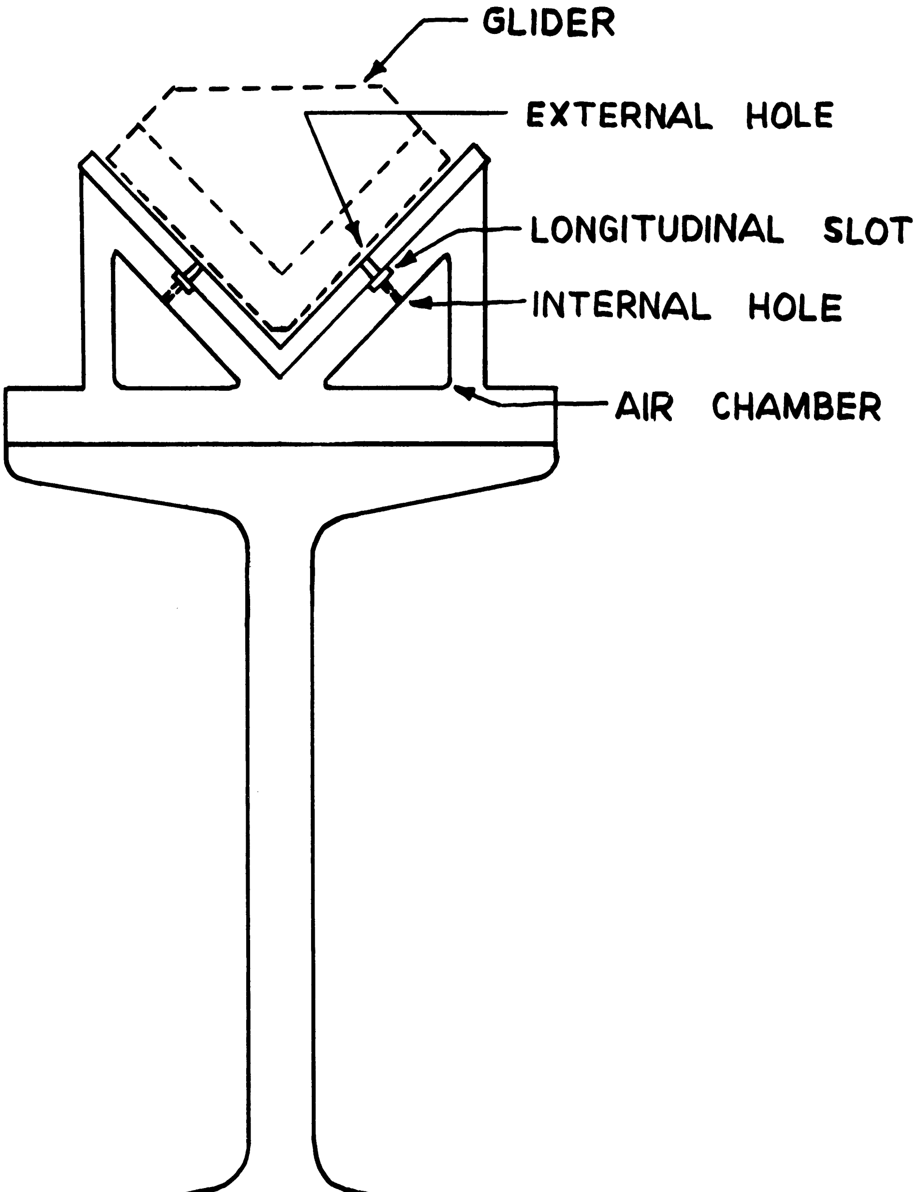

Figure 12. Cross-section of V-groove air bearing.

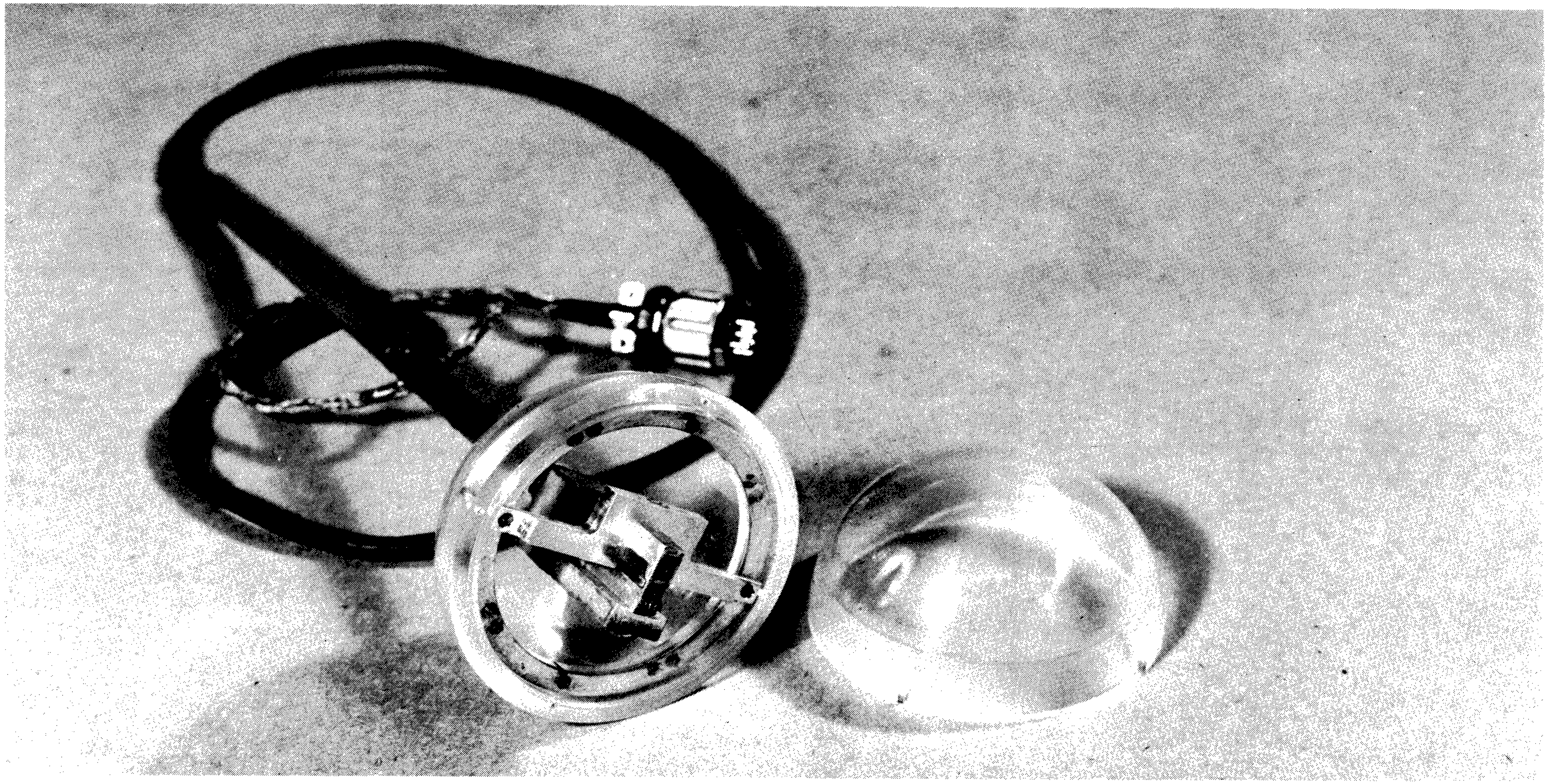

Figure 13. Photograph of sphere balance (before application of protective coating to drag transducer).

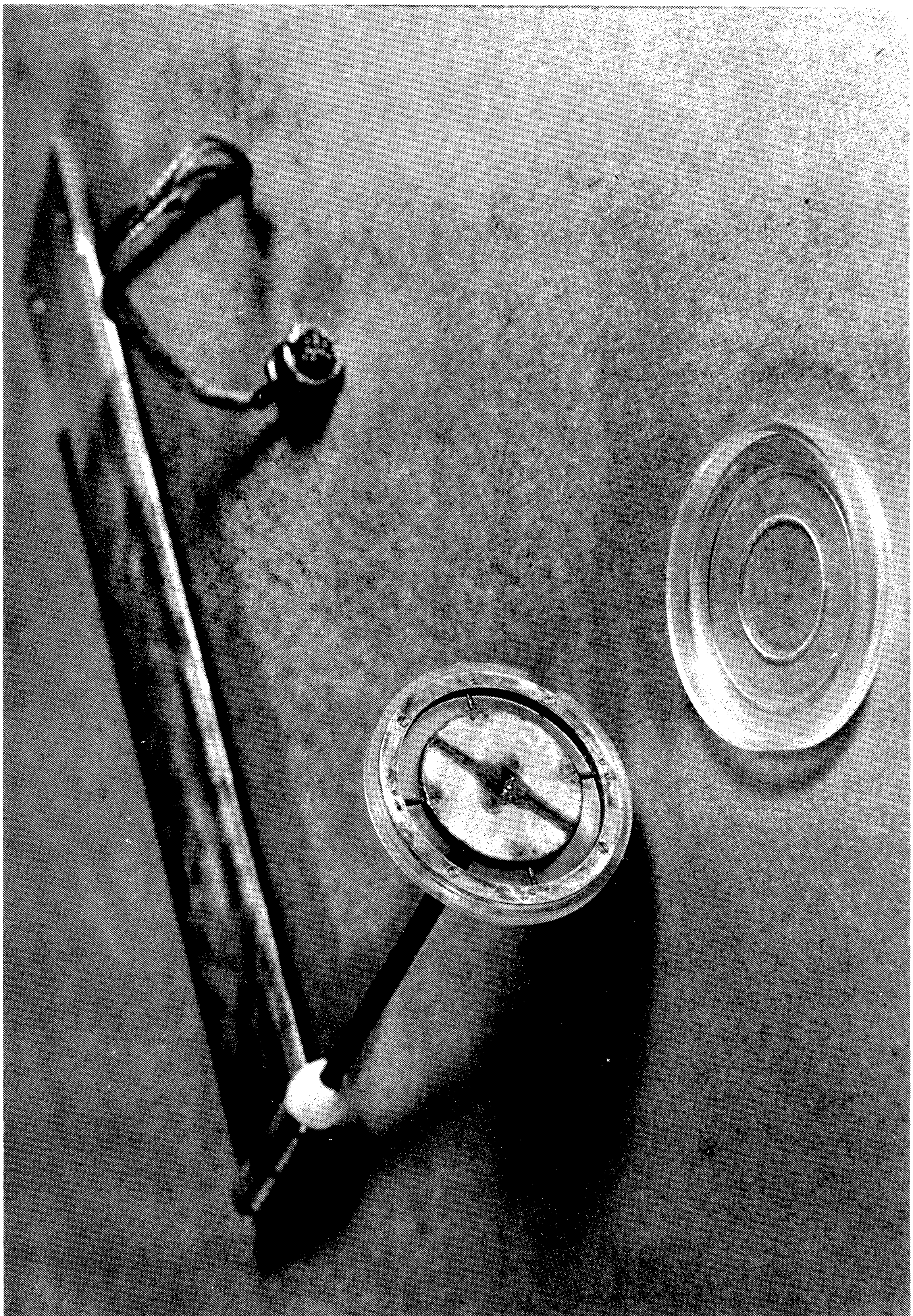

Figure 14. Photograph of disk balance mounted on sting and strut.

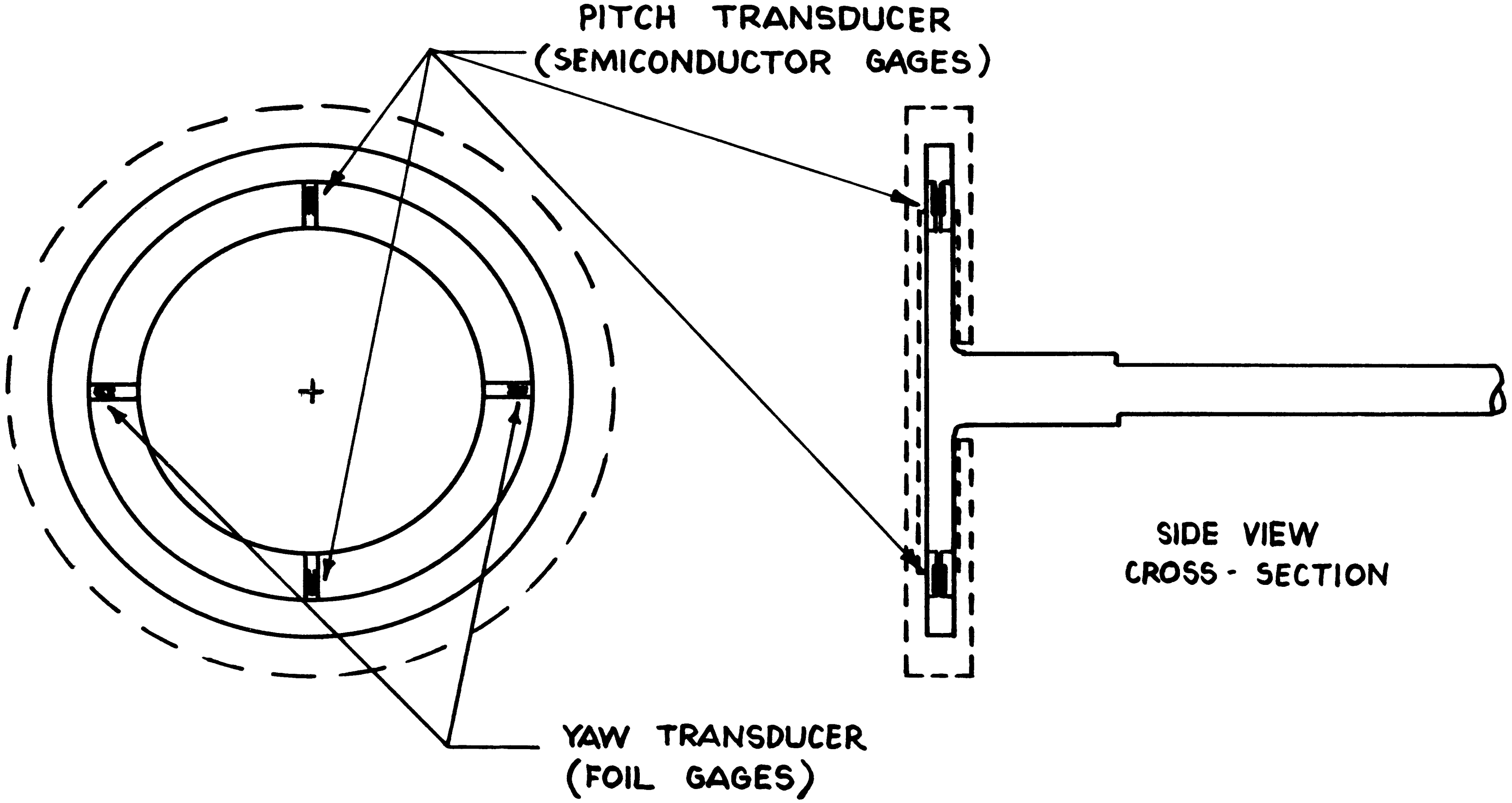

Figure 15. Drawing of disk balance.

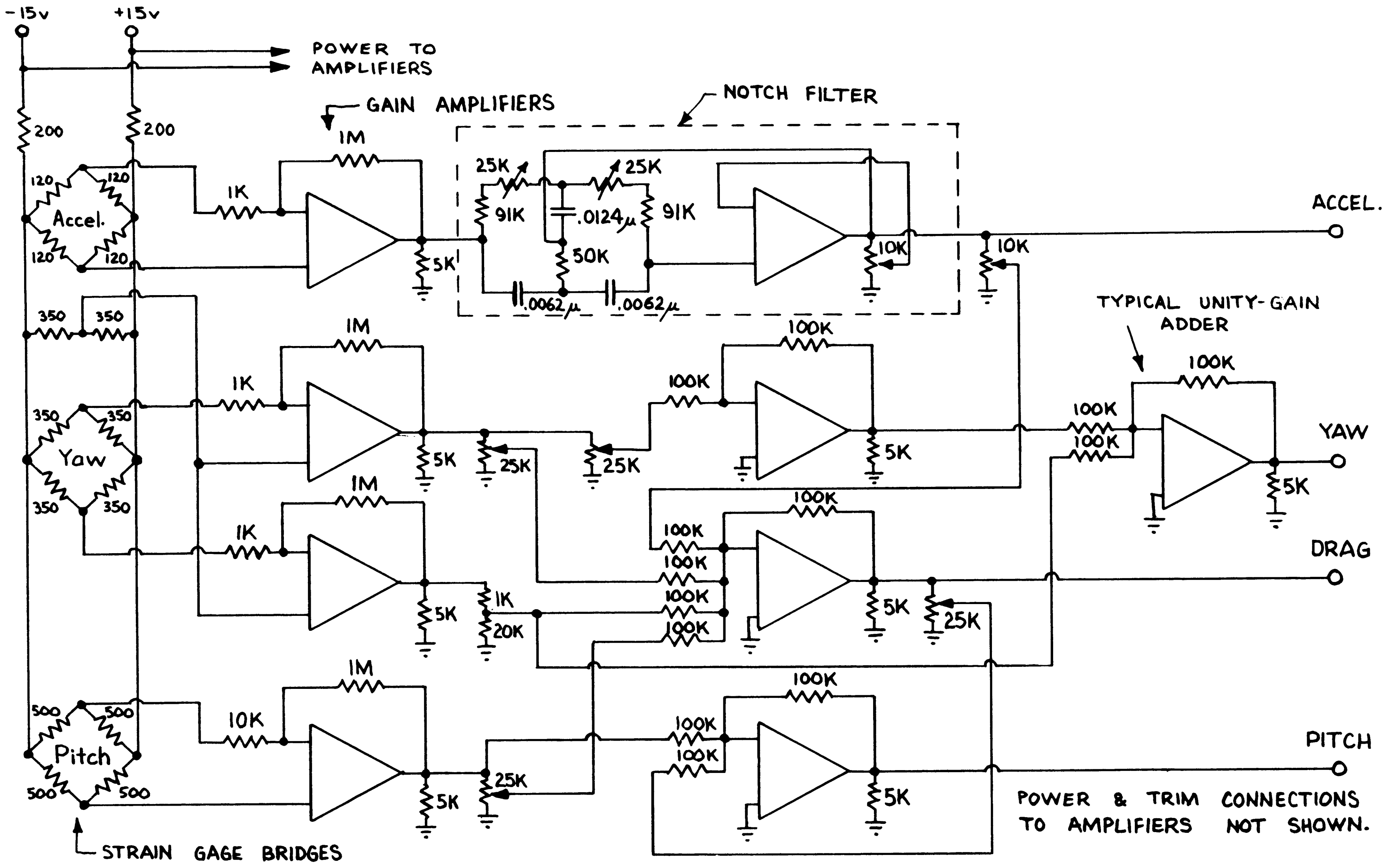

Figure 16. Diagram of circuit used with disk balance.

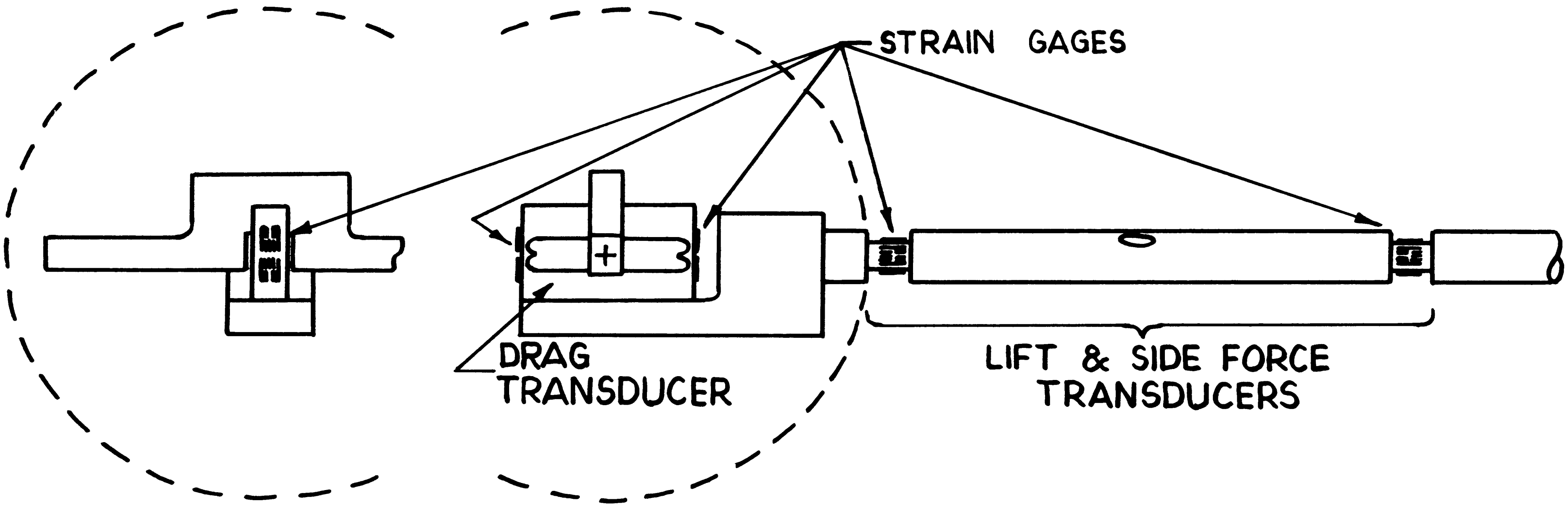

Figure 17. Drawing of sphere balance.

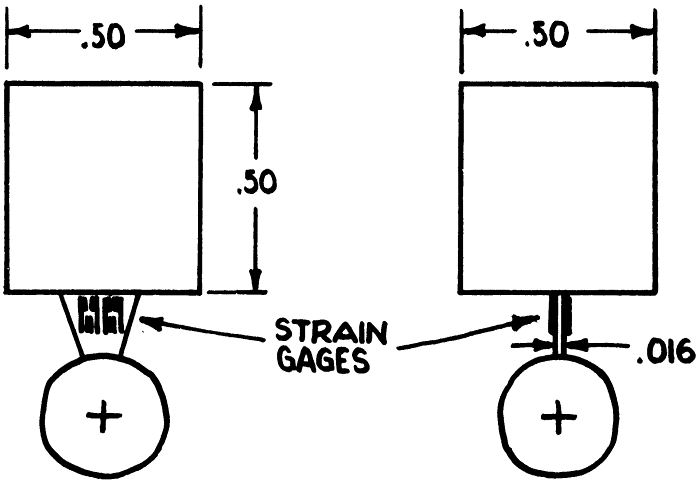

Figure 18. Drawing of accelerometer.

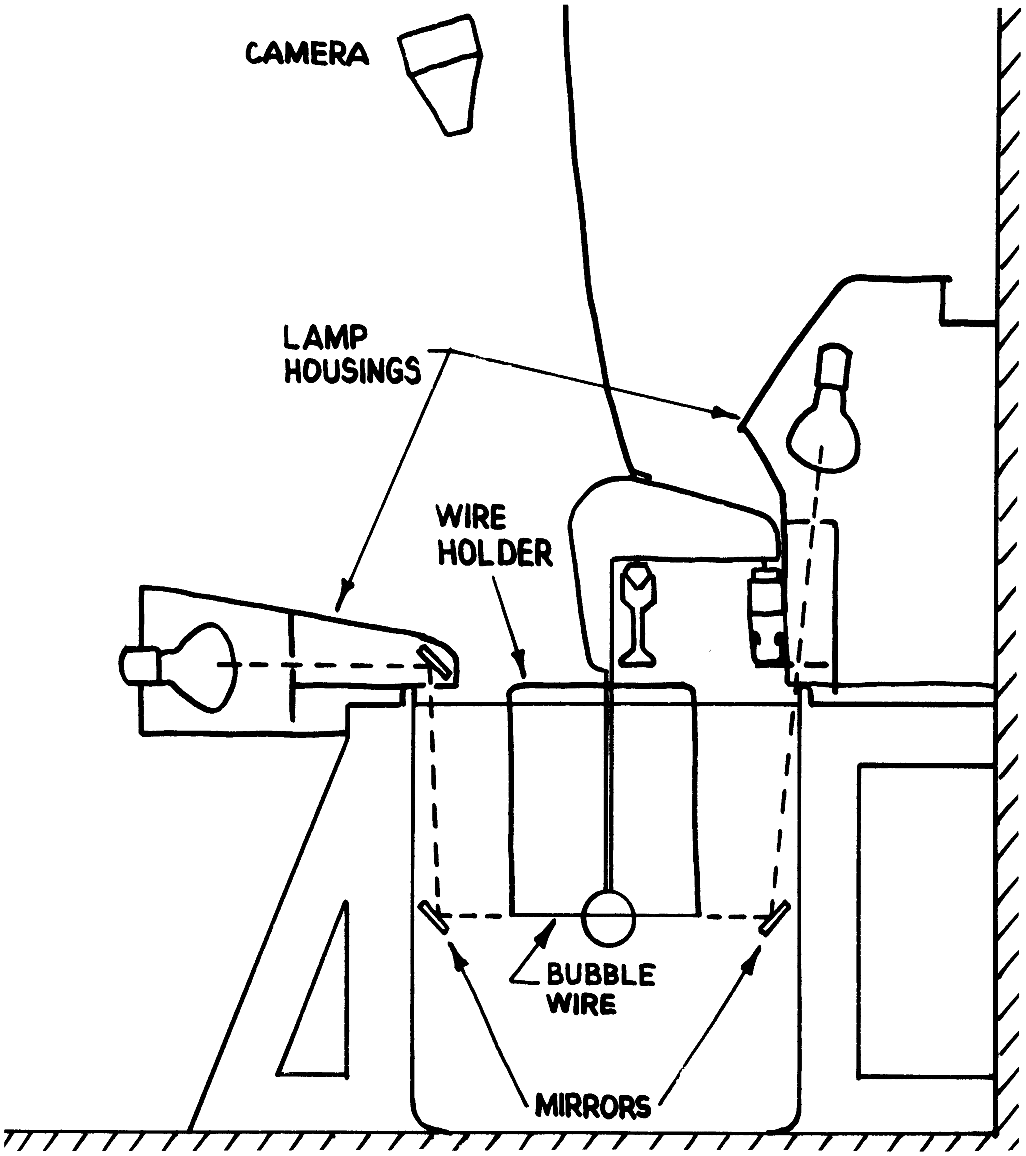

Figure 19. Flow visualization equipment.

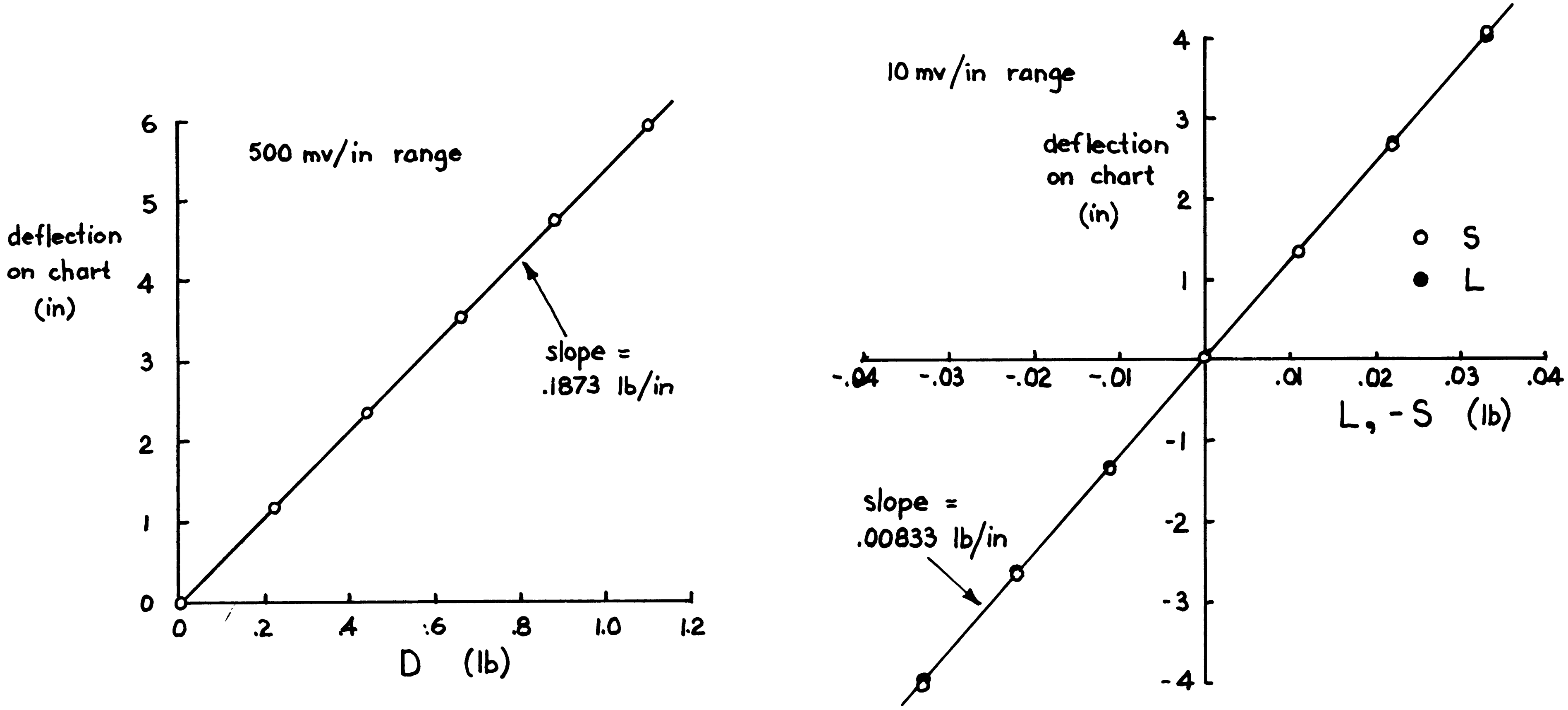

a. Drag transducer.

b. Lift and side force transducers.

Figure 20. Typical sphere balance calibration.

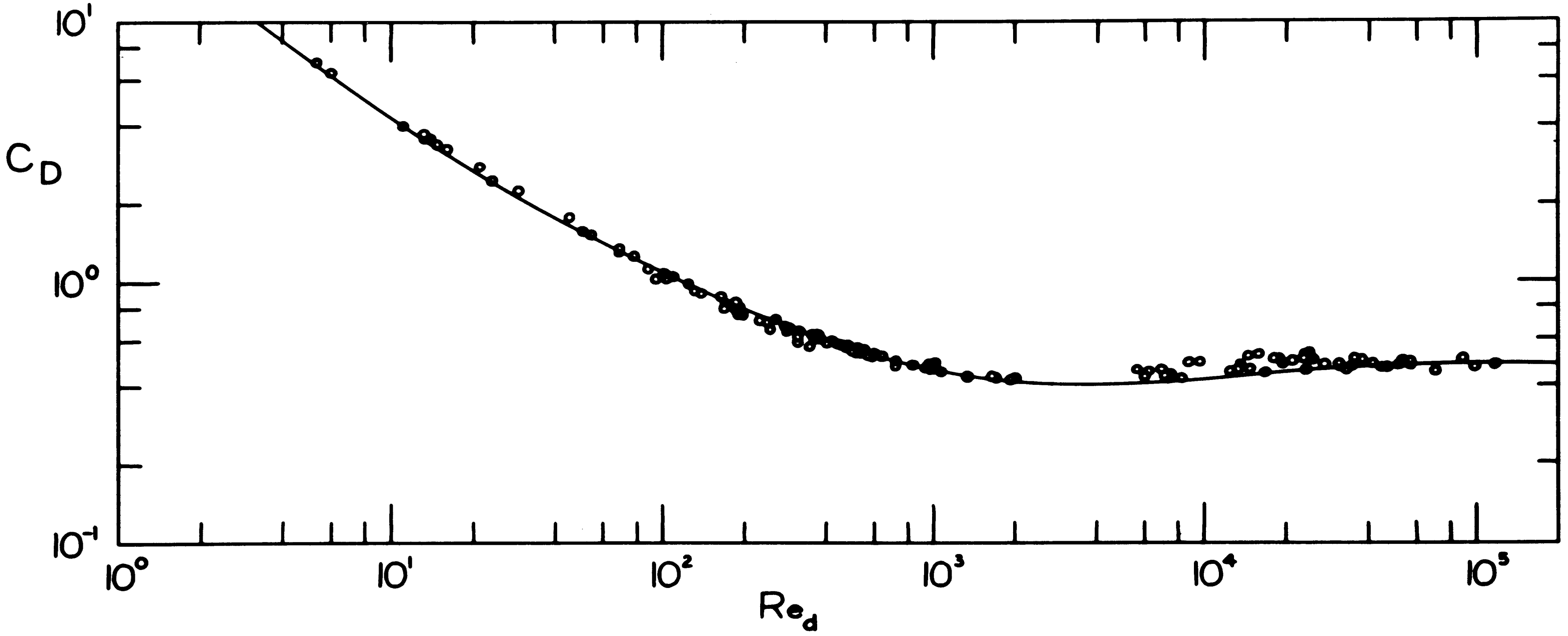

Figure 21. Sphere drag coefficient data from this experiment.

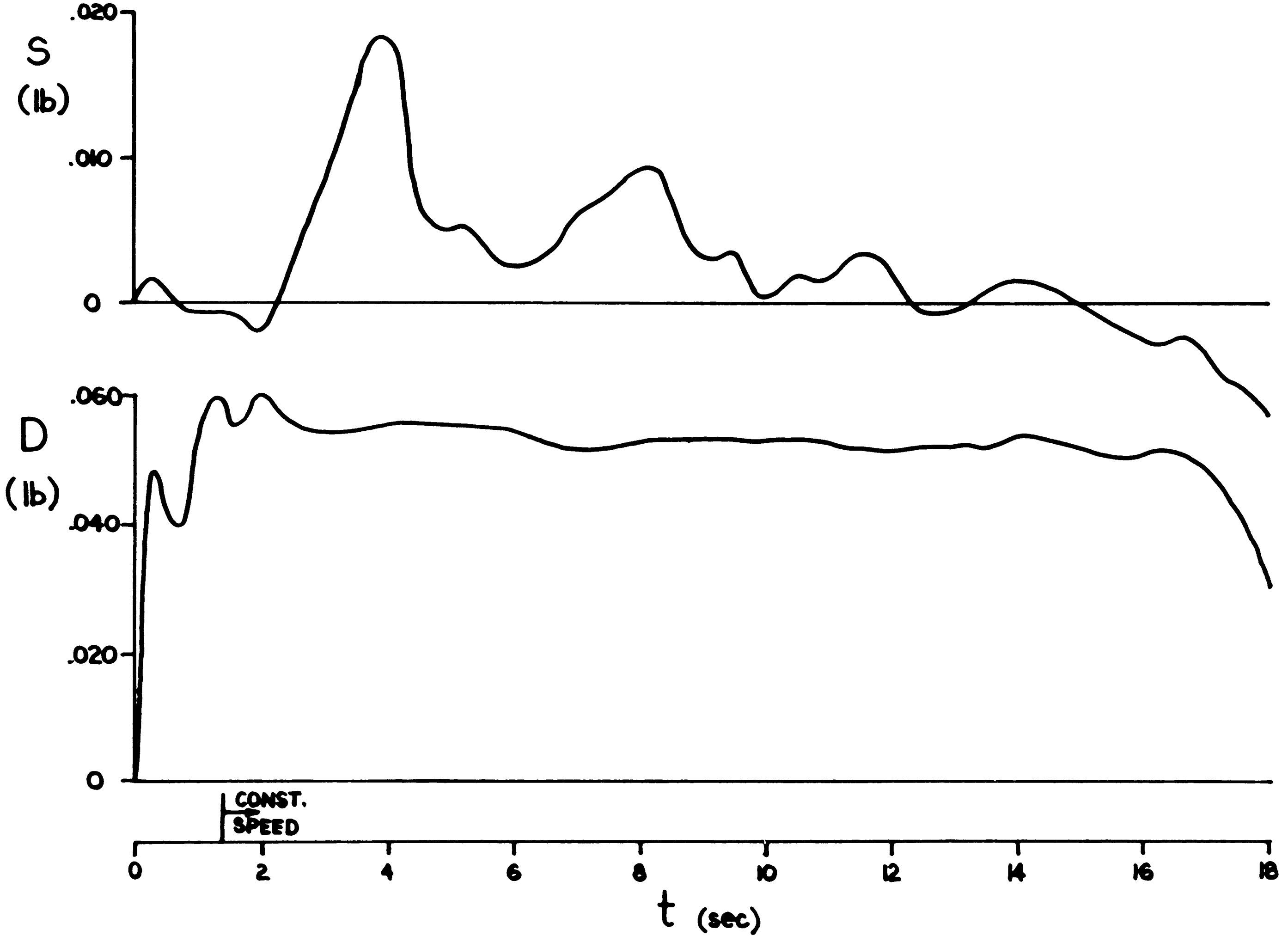

Figure 22. Typical sphere drag data record ($Re_d = 532$).

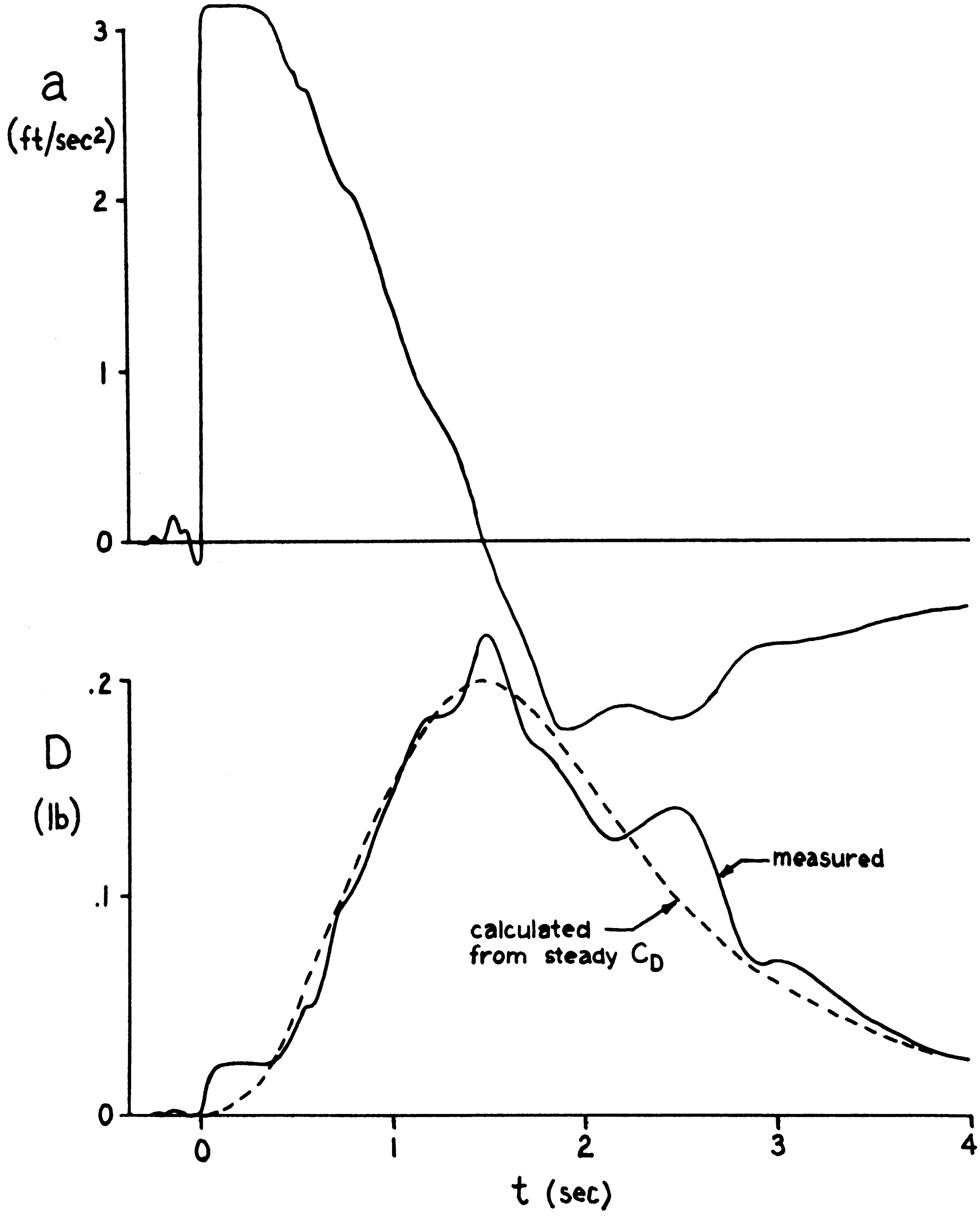

Figure 23. Data record of sphere drag during acceleration from rest.

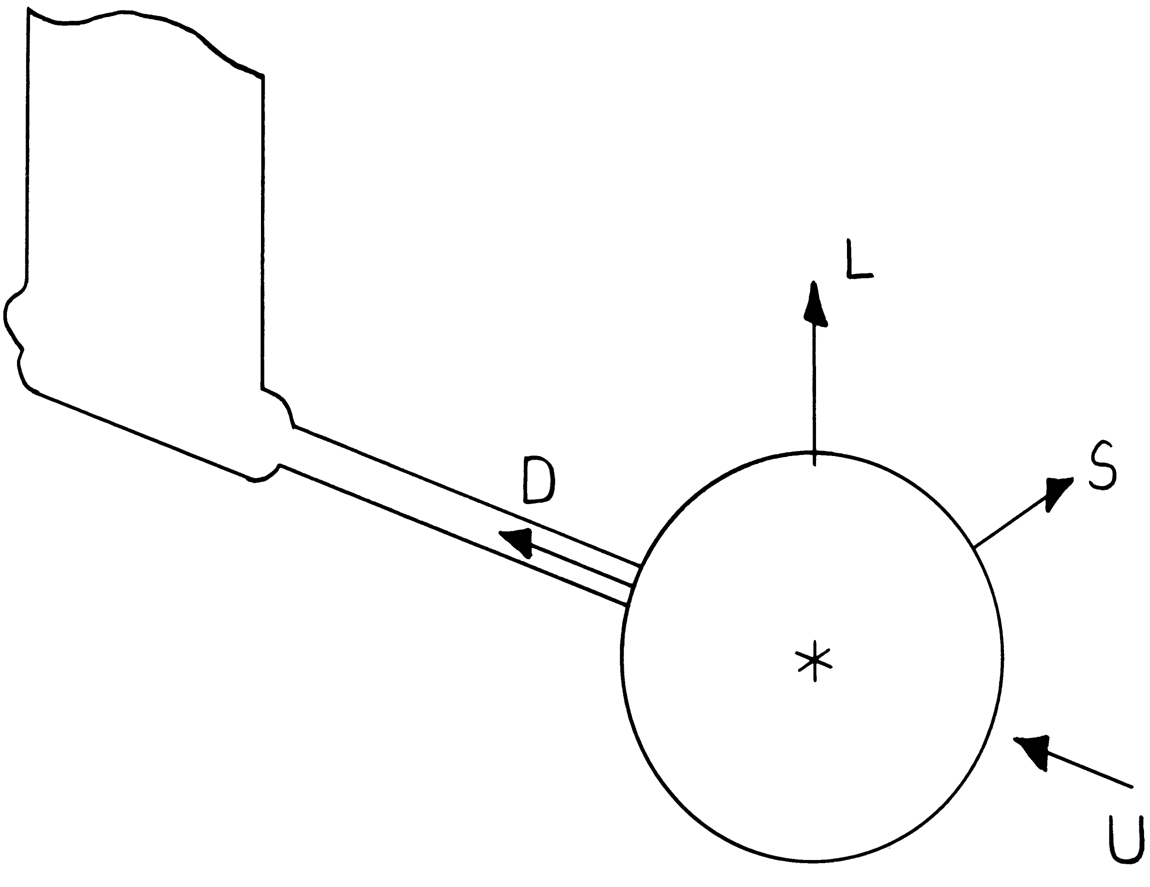

Figure 24. Sign conventions for forces on a sphere.

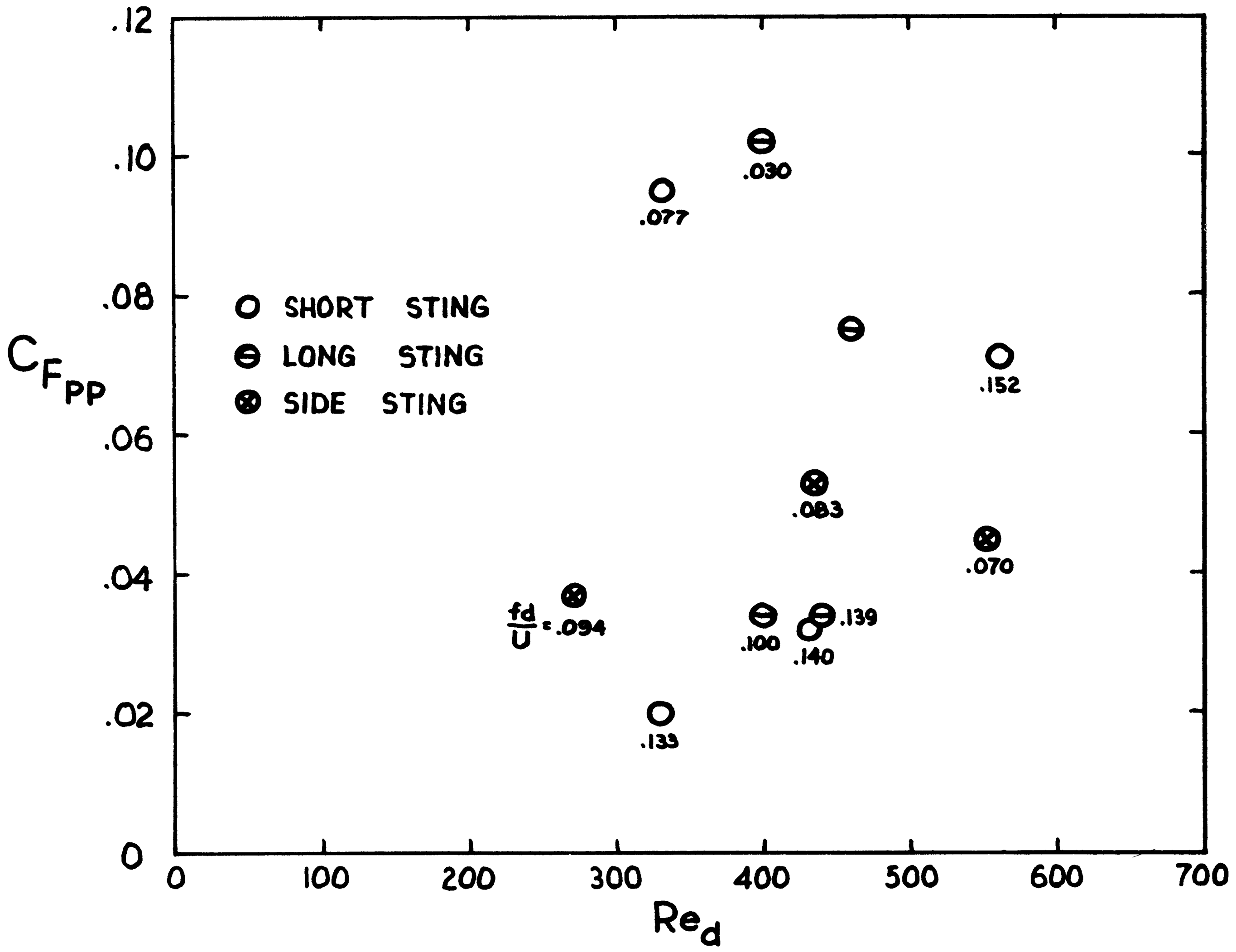

Figure 25. Transverse force coefficient for a sphere.

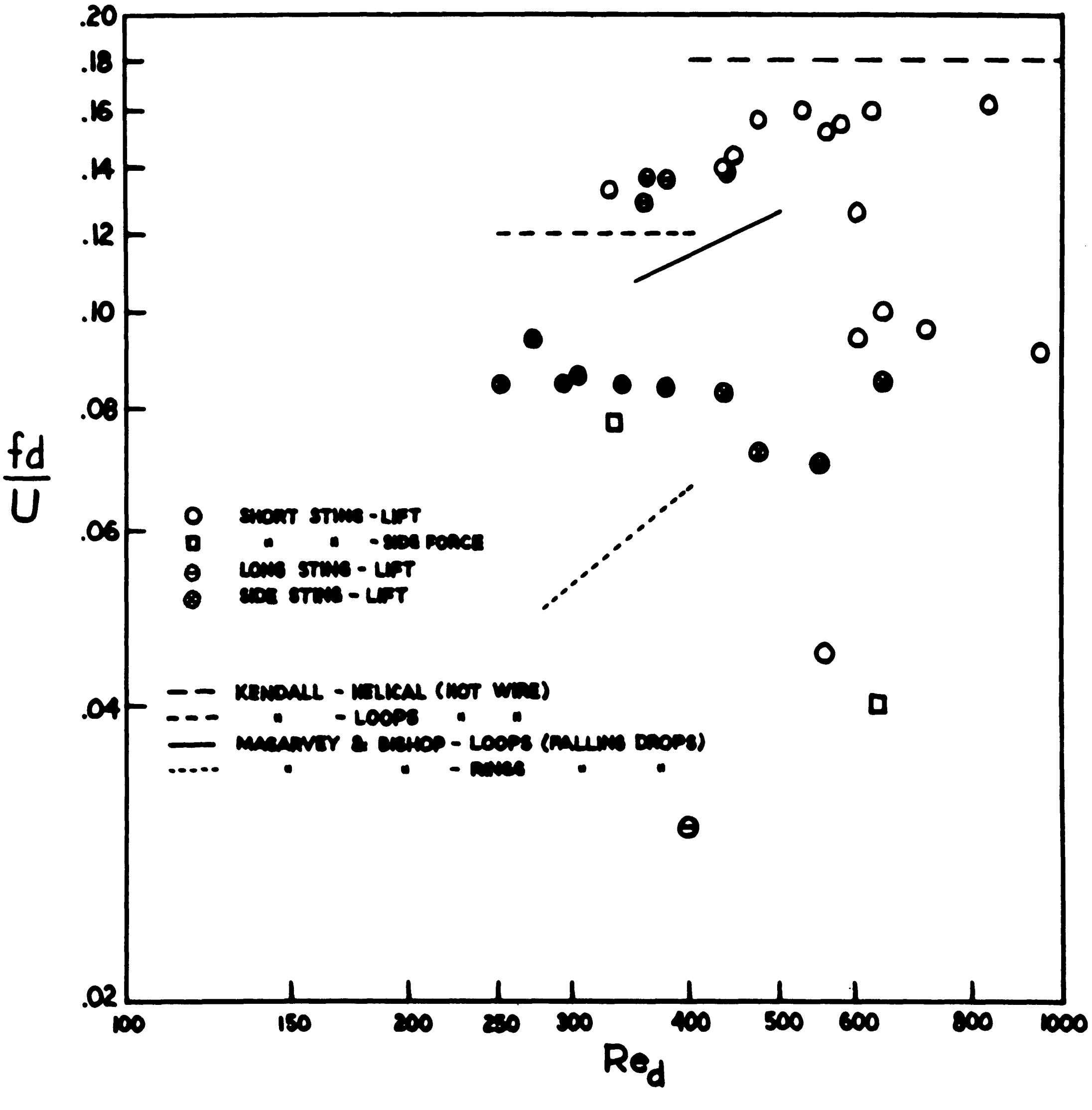

Figure 26. Frequency of oscillation of transverse force on sphere.

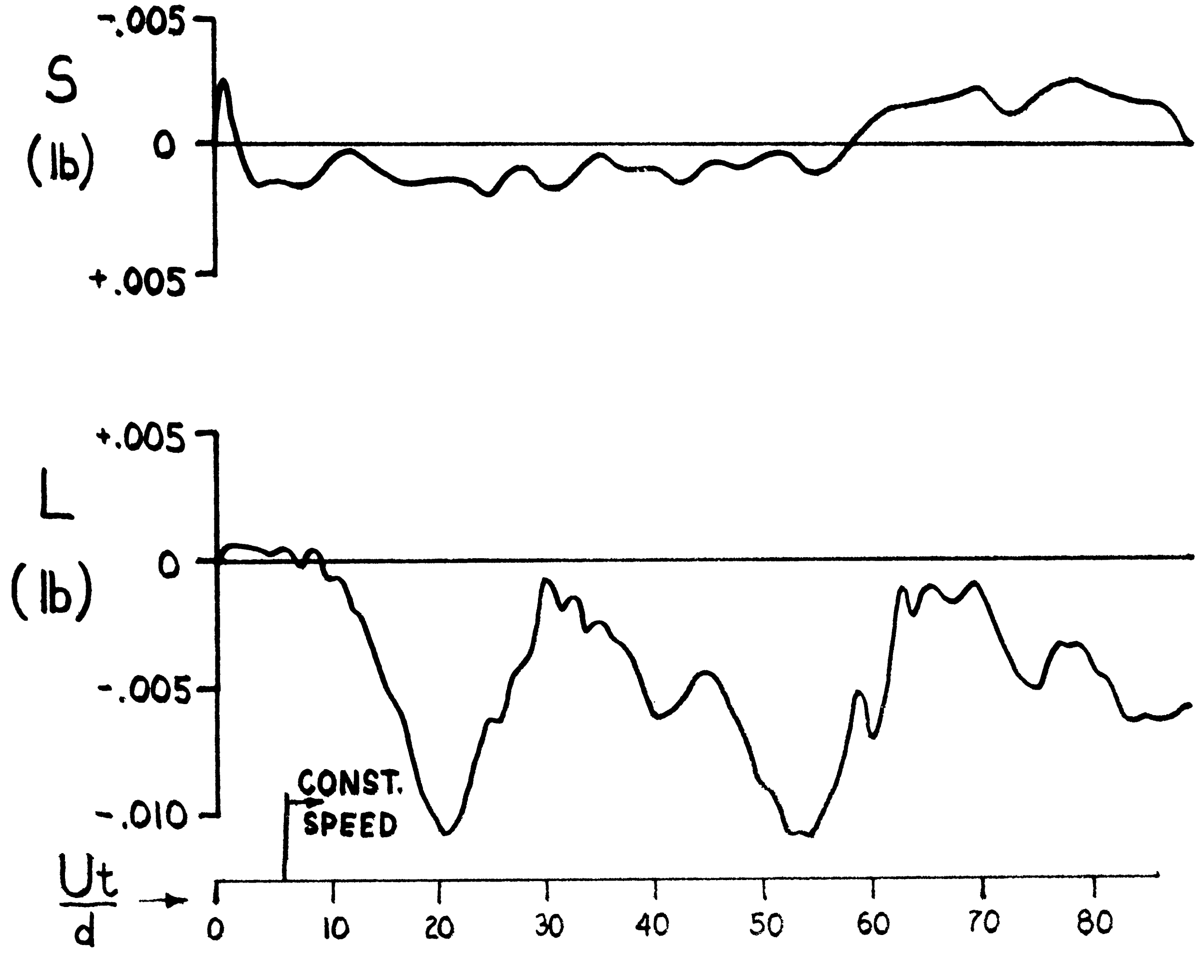

Figure 27. Data record of sphere lift and side force showing low-frequency oscillation. Long sting; $Re_d = 399$.

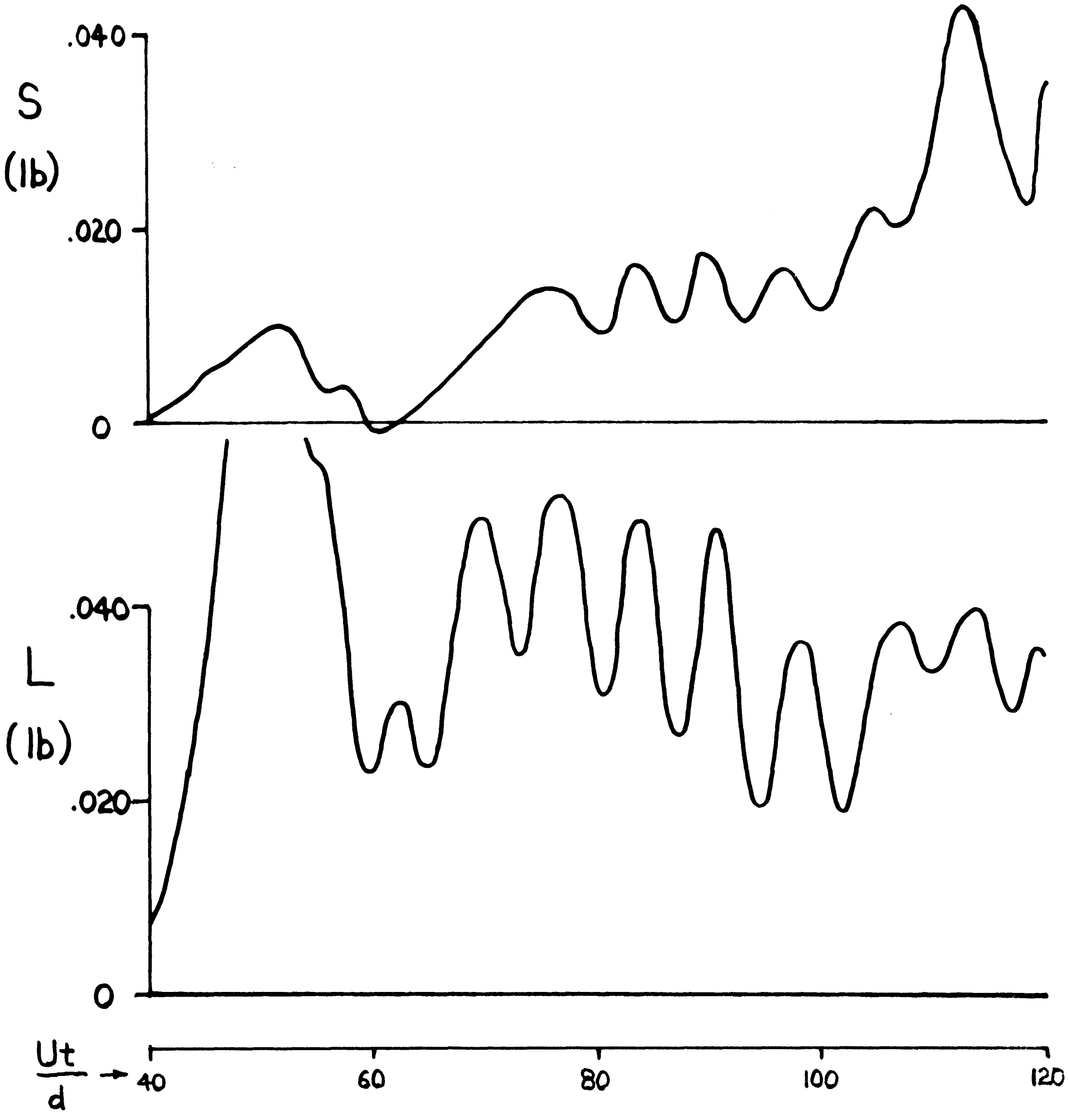

Figure 28. Sphere data record showing transition of fluctuation from lift to side force ($Re_d = 433$).

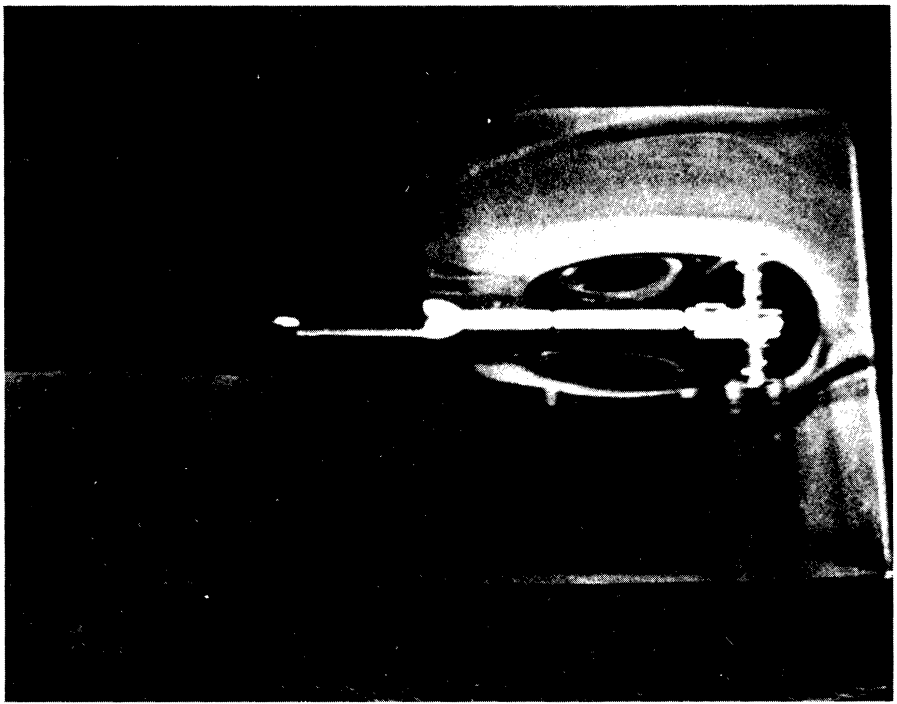

a. Sphere on sting ($Re_d = 269$).

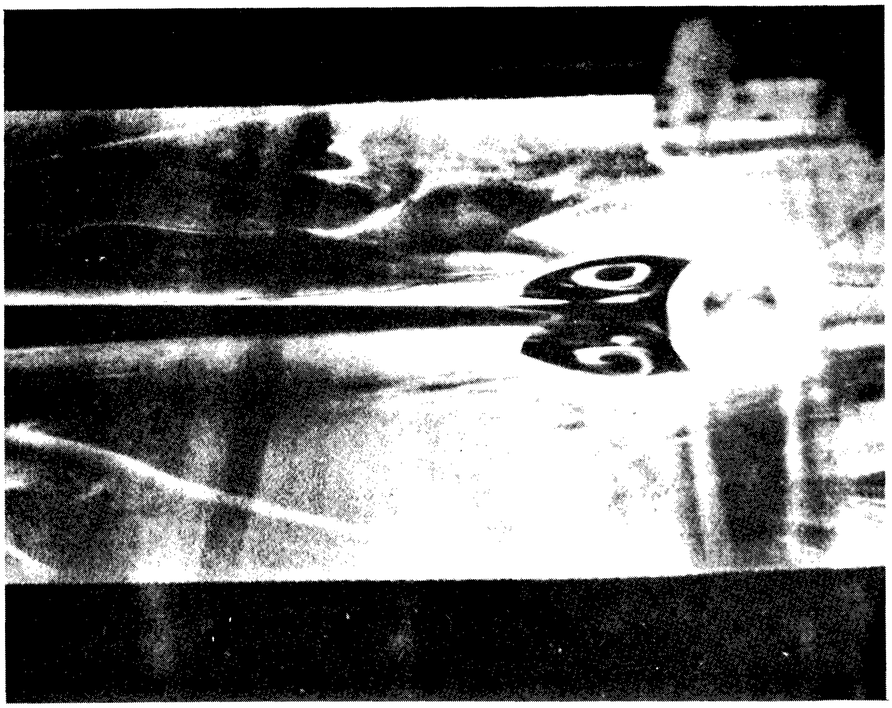

b. Sphere suspended on threads ($Re_d = 192$).

Figure 29. Photograph of steady flow about a sphere.

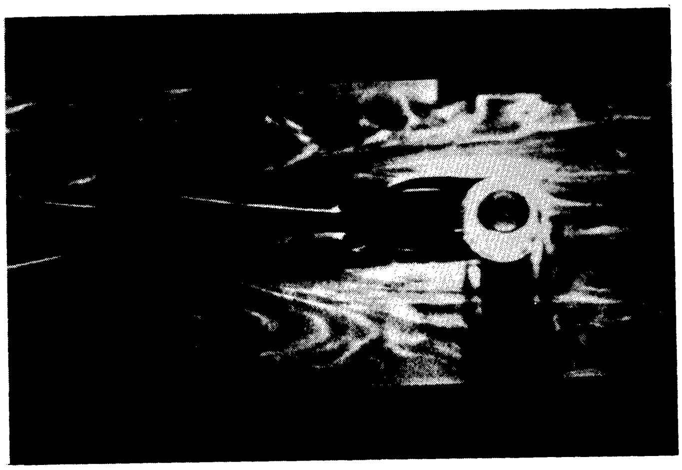

a. Sphere shedding a vortex loop.

b. Same segment of wake after 16 sec.

c. Same segment of wake after 35 sec.

Figure 30. Vortex loop wake behind a sphere at $Re_d = 295$.

Figure 31. Sphere shedding vortex loops at $Re_d = 377$.

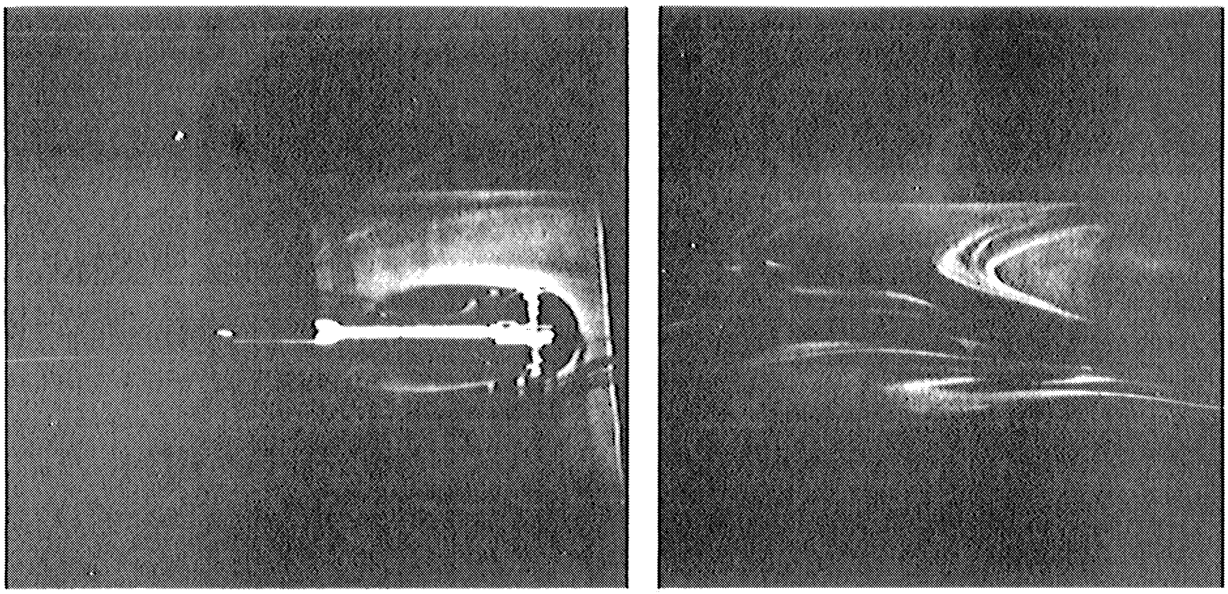

Flow about sphere.

Same position 15 sec. later.

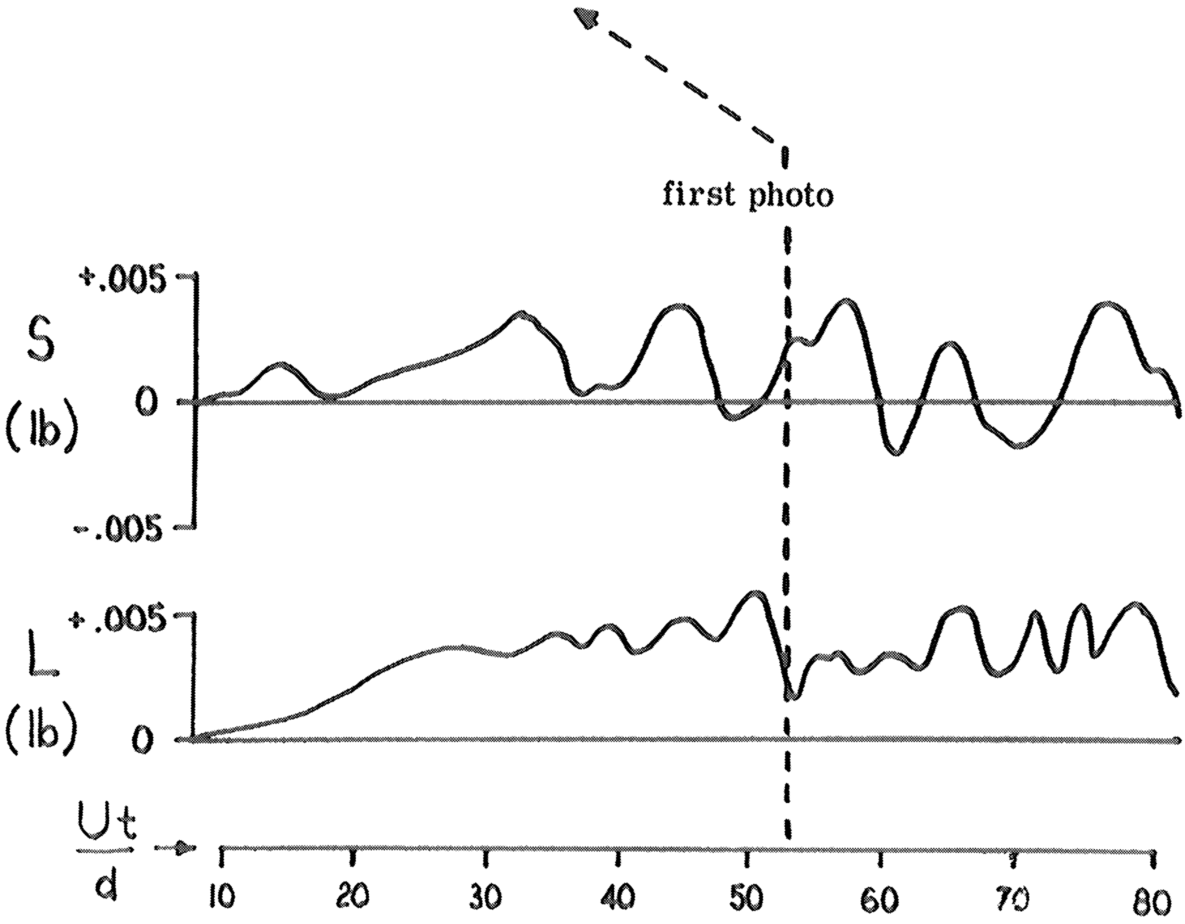

Figure 32. Data record and flow photographs of sphere--regular side force oscillations at $Re_d = 332$.

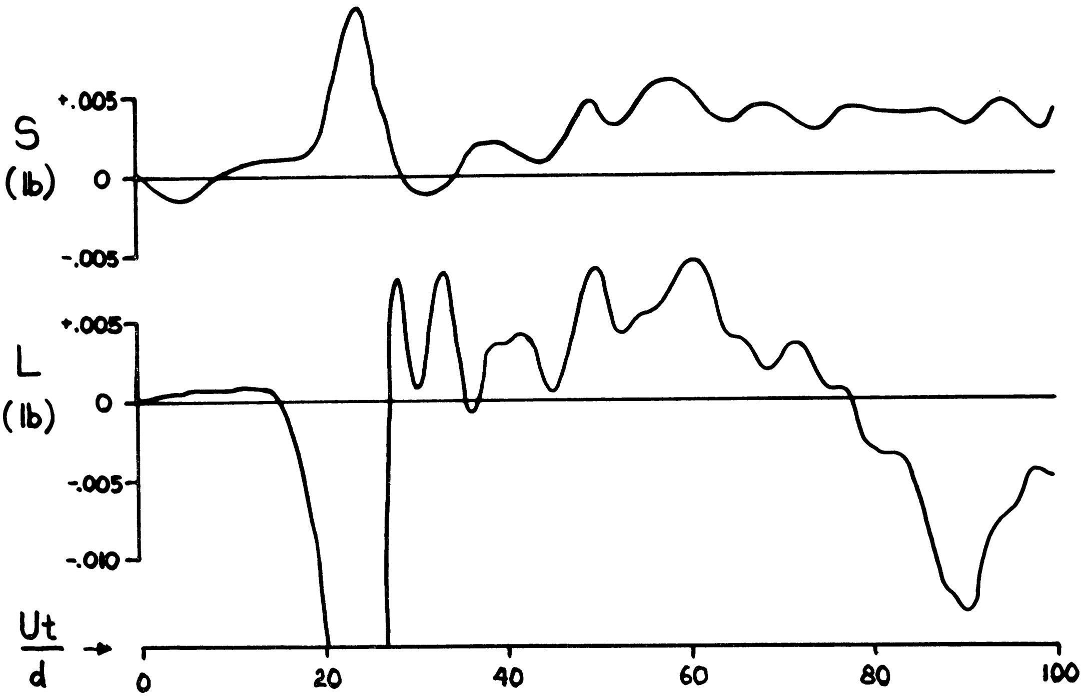

Figure 33. Sphere data record showing irregular fluctuations in lift and side force at $Re_d = 715$.

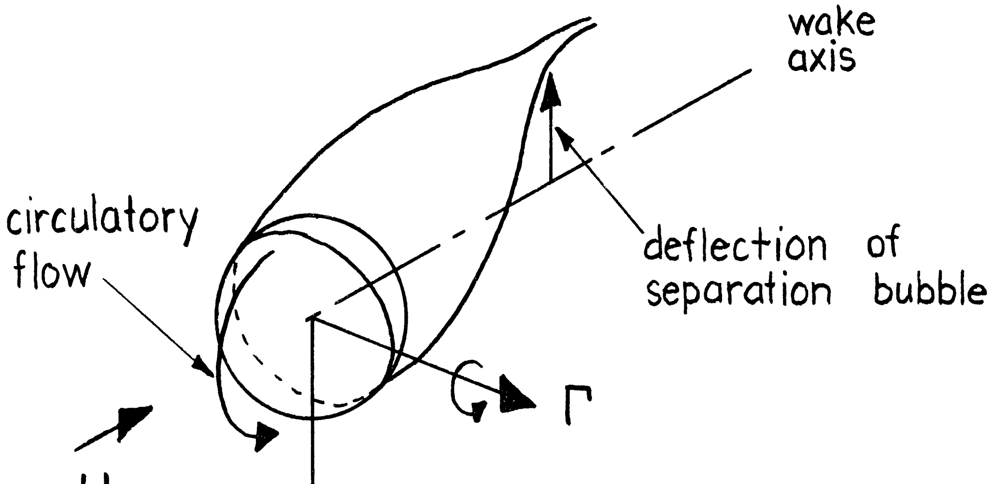

Figure 34. Model relating unsteady transverse force to sphere wake fluctuation.

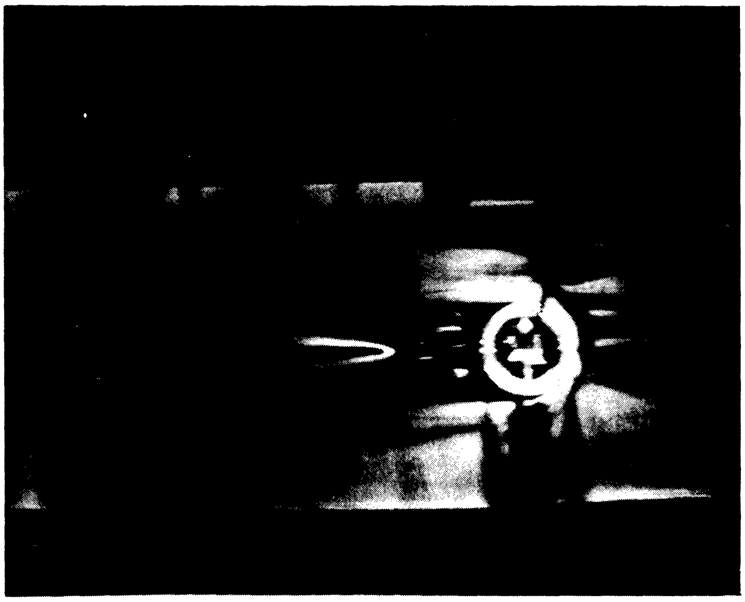

a. Wake immediately behind sphere.

b. Same segment of wake 15 sec. later.

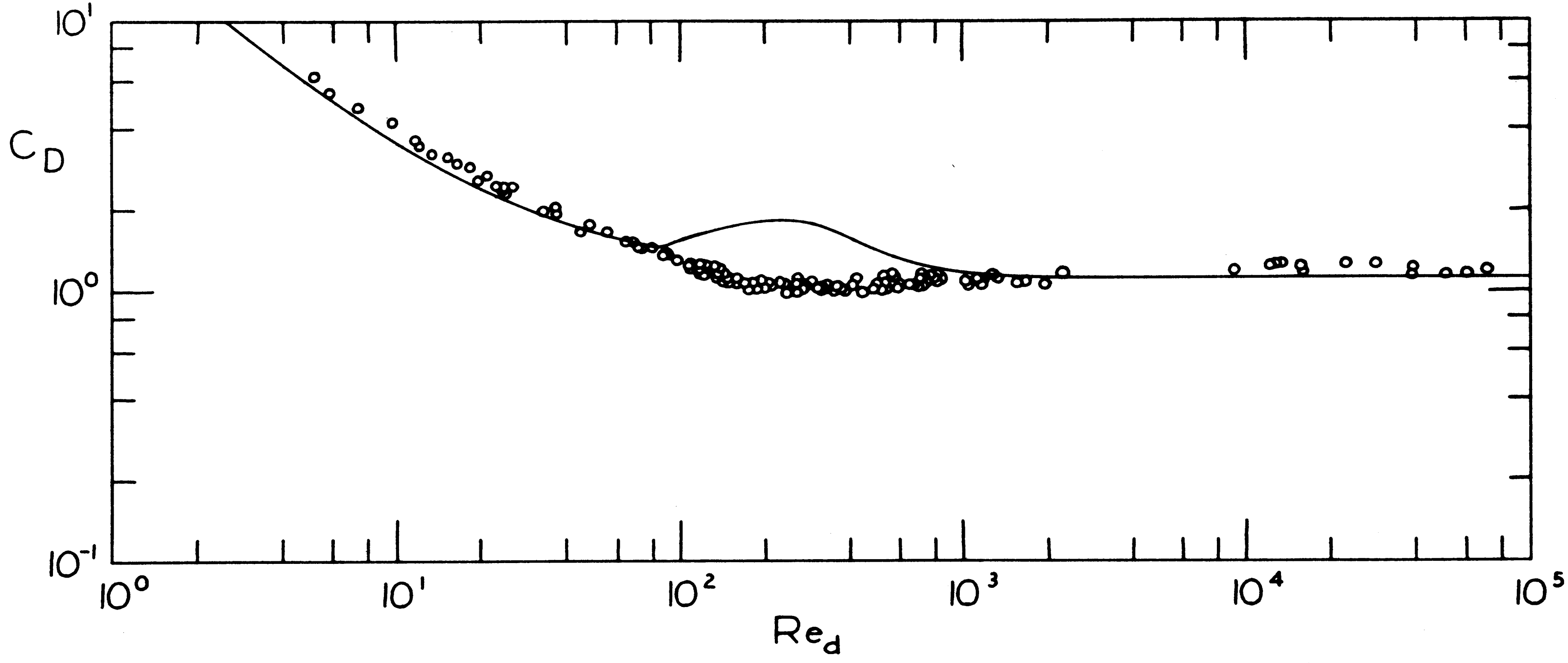

Figure 36. Disk drag coefficient data from this experiment.

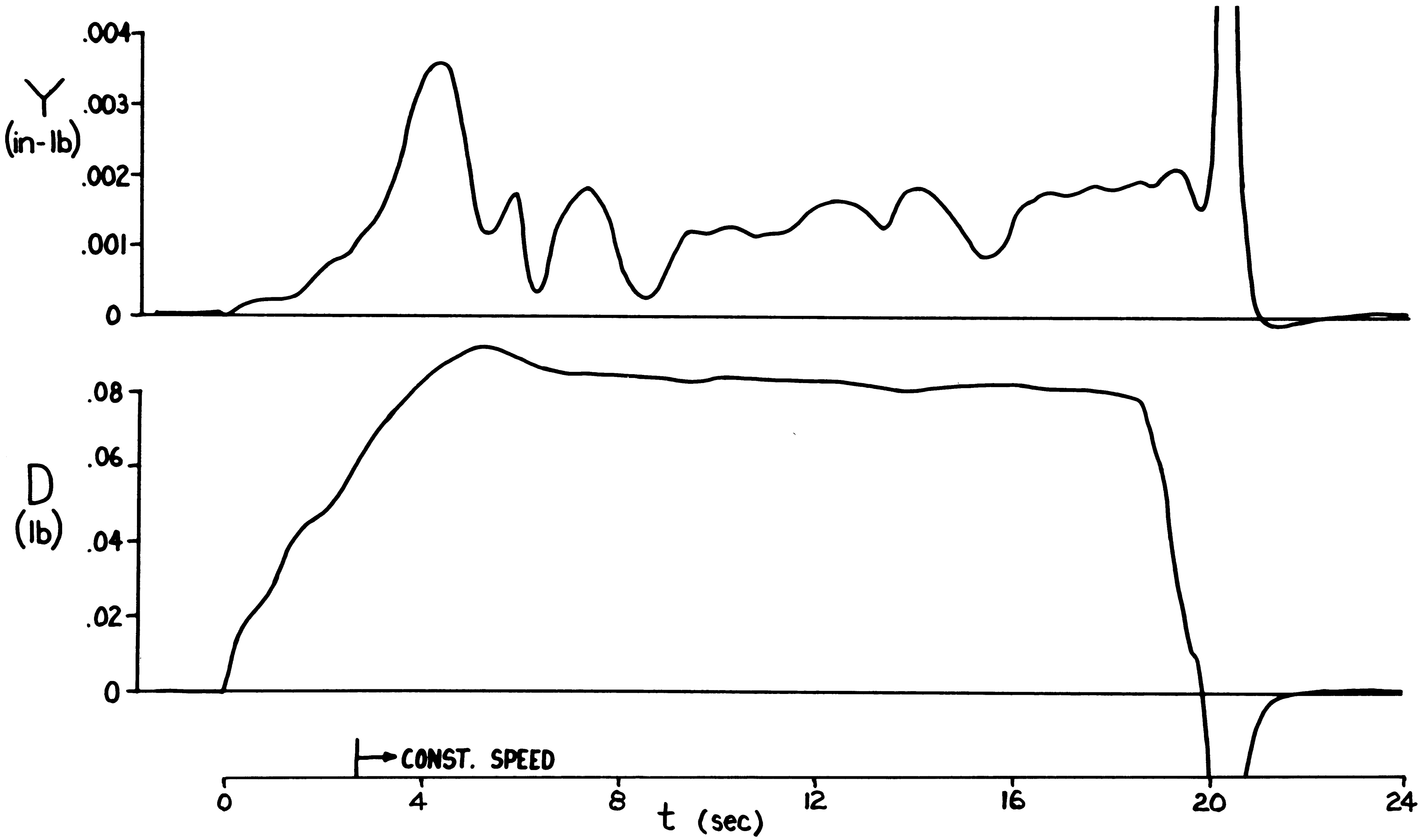

Figure 37. Typical disk drag data record ($Re_d = 530$).

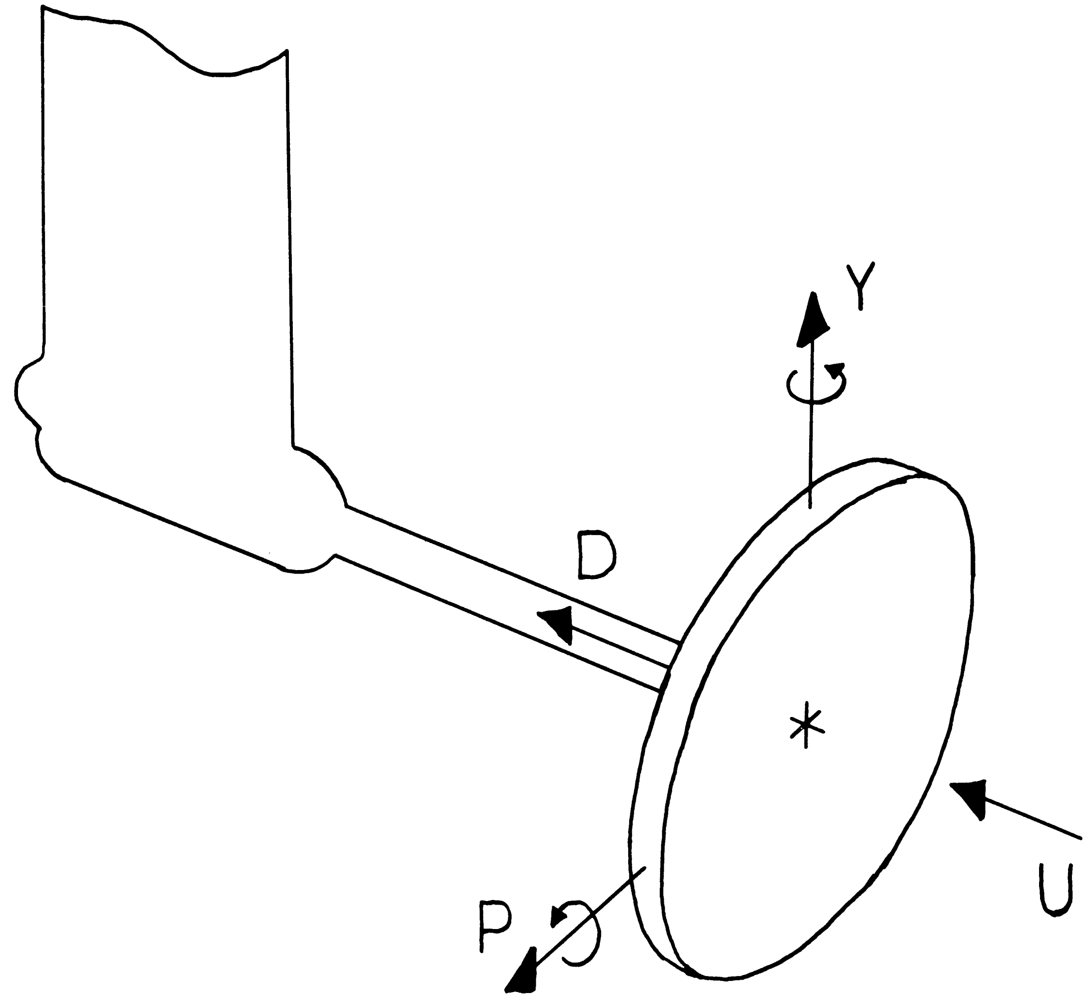

Figure 38. Sign conventions for drag and moments on a disk.

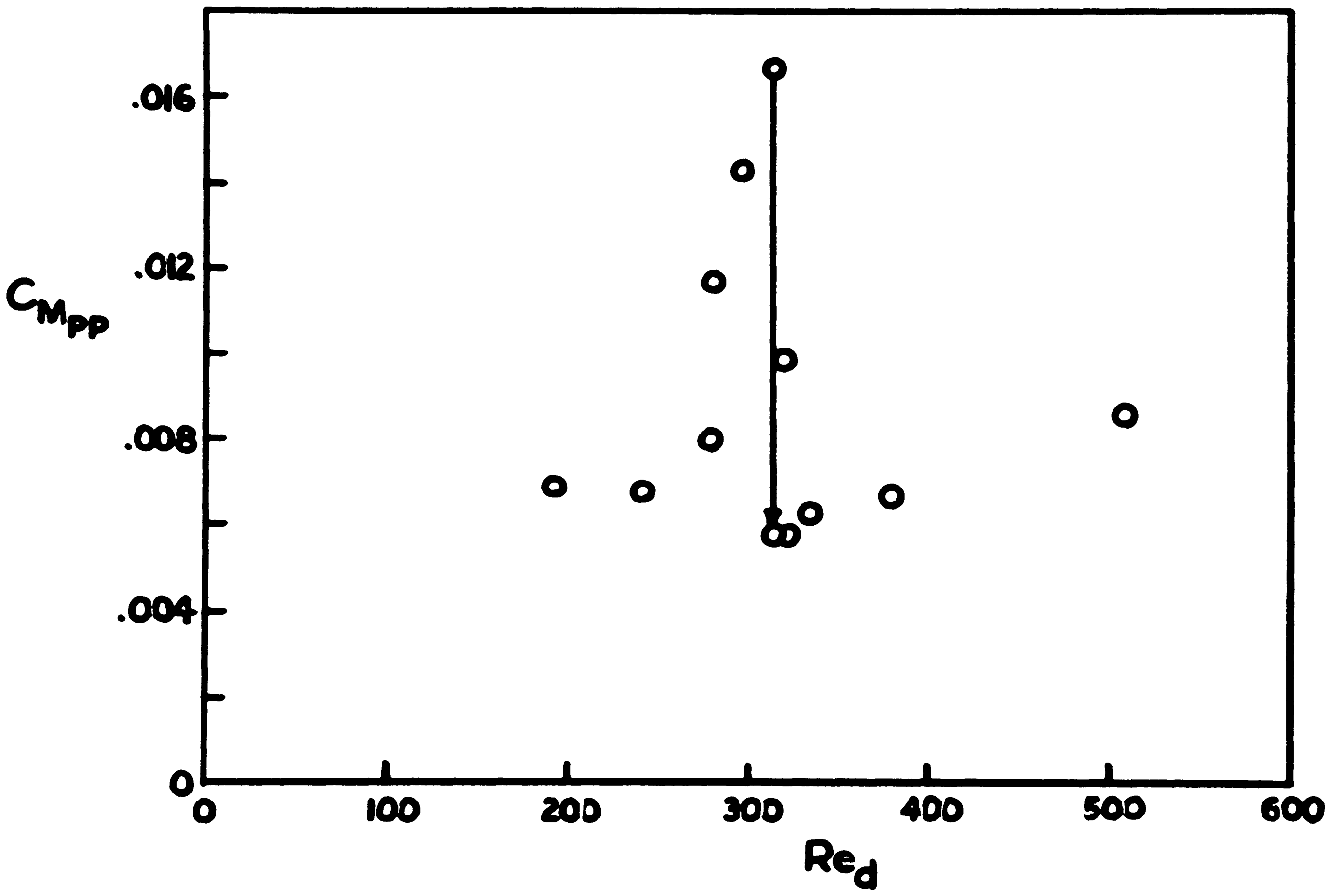

Figure 39. Moment coefficient for a disk.

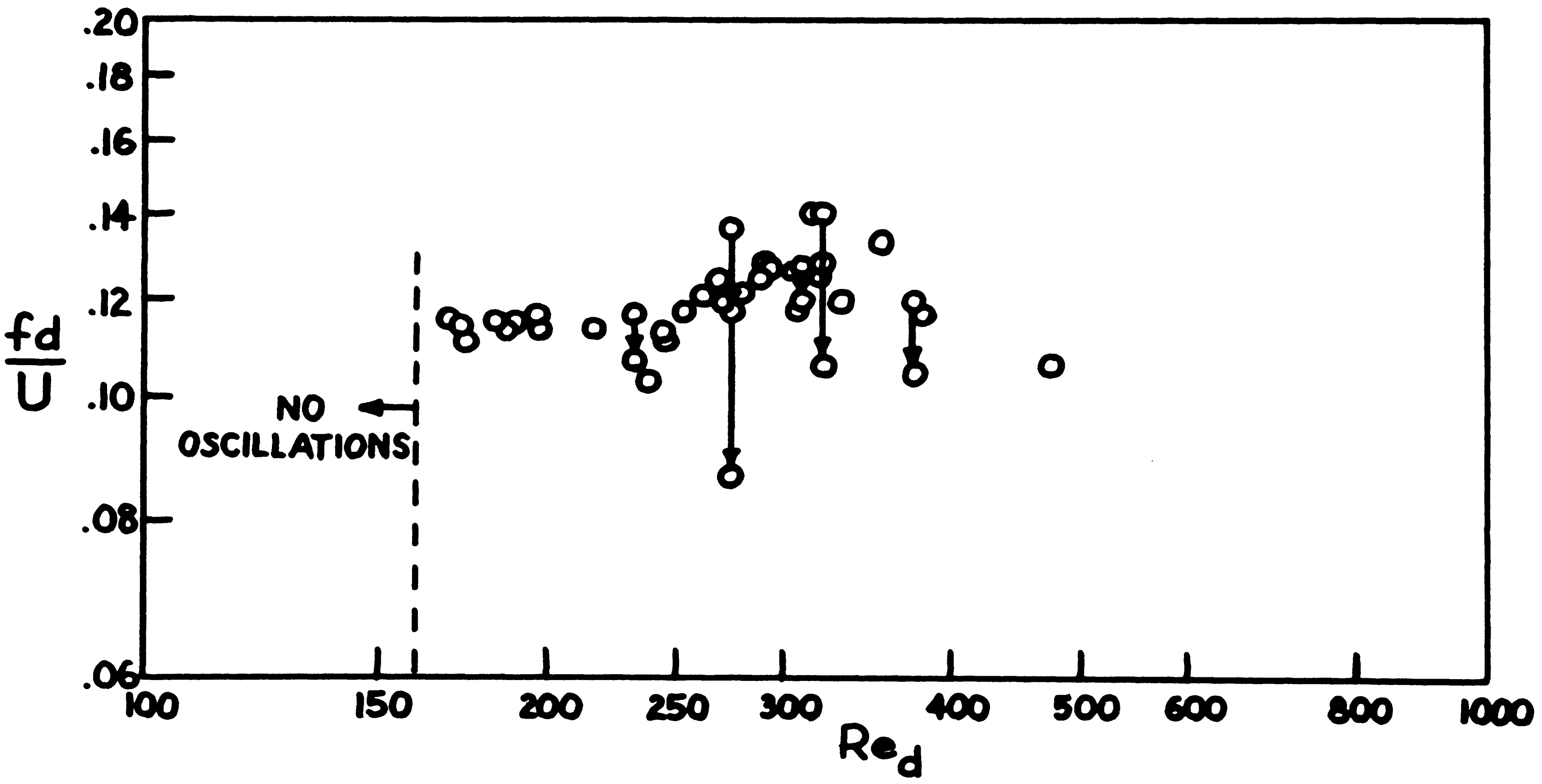

Figure 40. Frequency of oscillation of disk moment.

Figure 41. Photograph of steady flow about a sting-mounted disk at $Re_d = 157$.

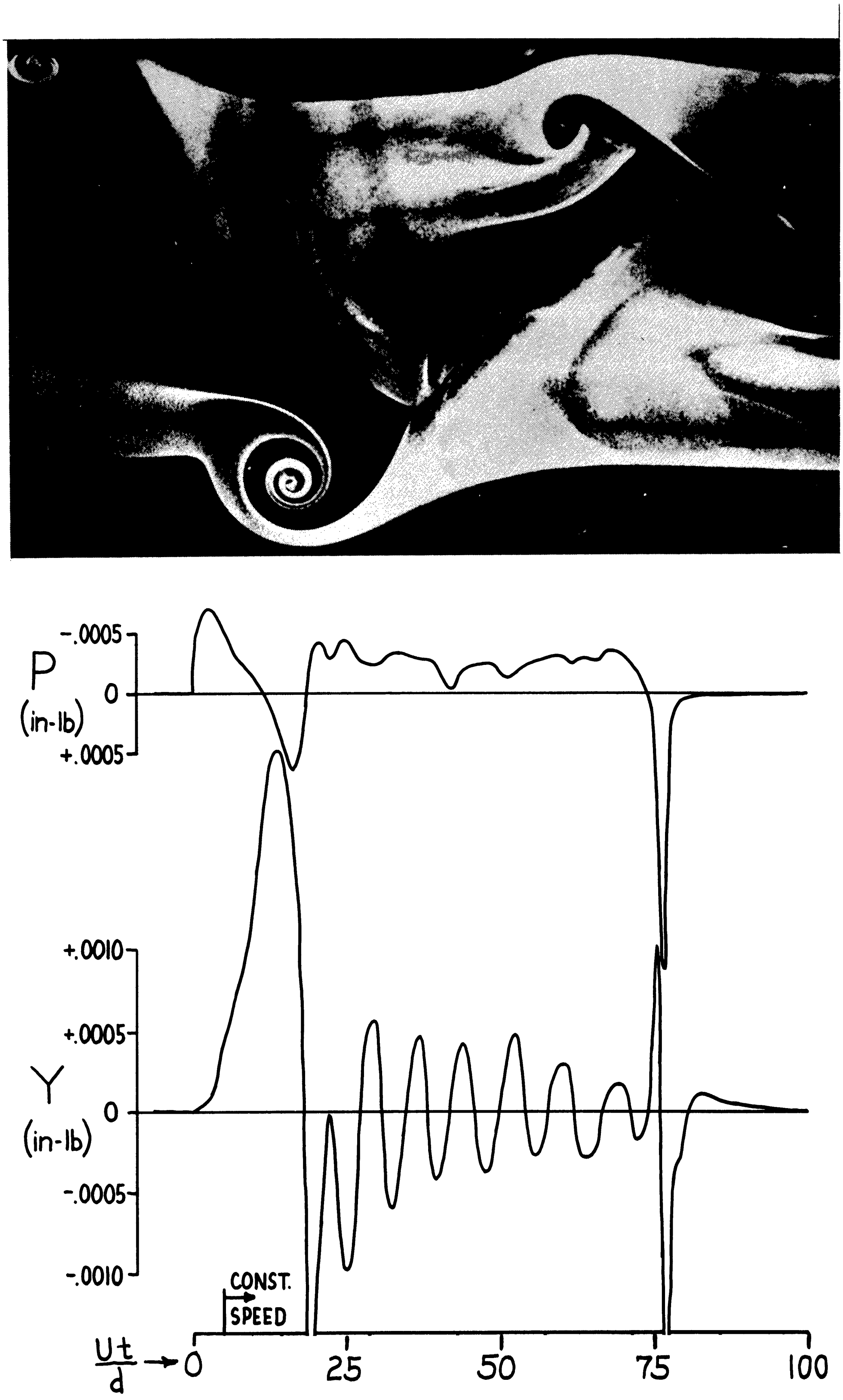

Figure 42. Data record and wake photograph for disk showing regular oscillations in yaw at $Re_d = 318$.

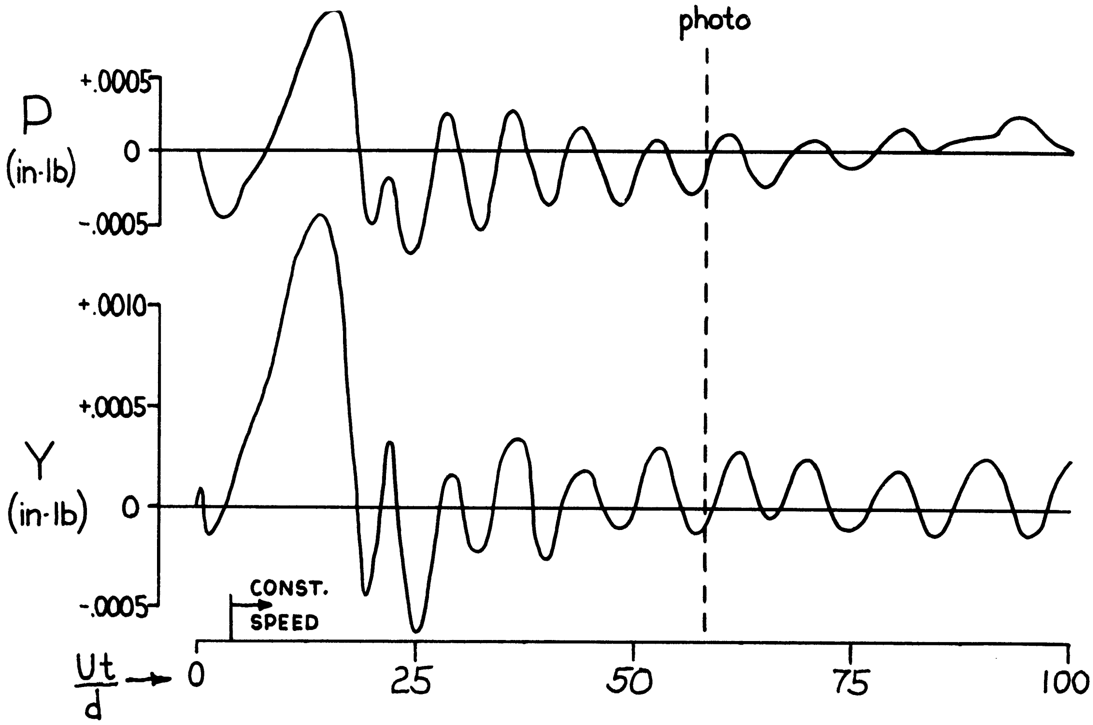

Figure 43. Data record and flow photograph for disk showing combined oscillation in pitch and yaw at $Re_d = 278$.

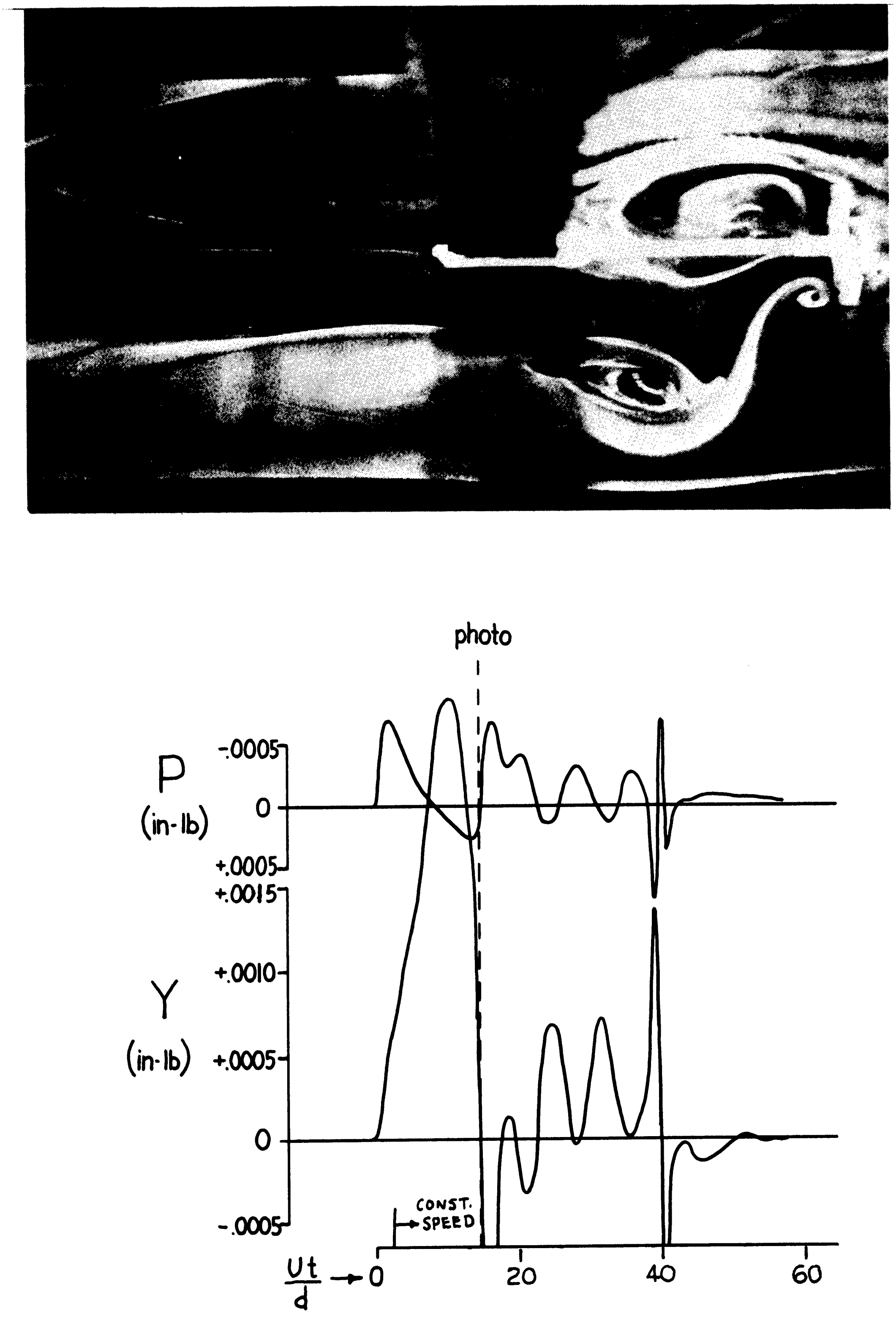

Figure 44. Data record and flow photograph for disk showing initial vortex shedding at $Re_d = 305$.

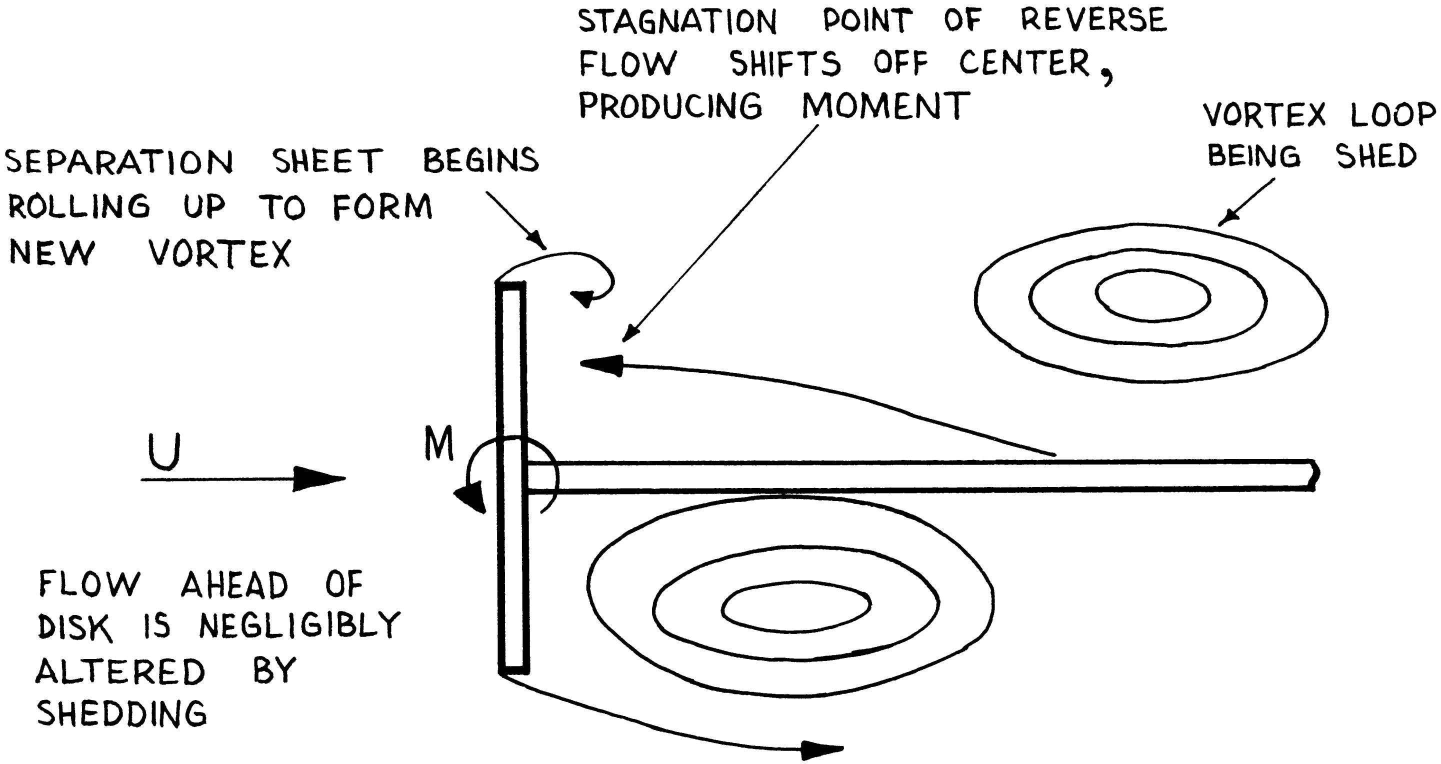

Figure 45. Model relating unsteady disk moment to vortex shedding.

DOCUMENT CONTROL DATA - R & D

(Security classification of title, body of abstract and indexing annotation must be entered when the overall report is classified)

1. ORIGINATING ACTIVITY *(Corporate author)*

Department of Aerospace Engineering
The University of Michigan
Ann Arbor, Michigan

2a. REPORT SECURITY CLASSIFICATION

Unclassified

2b. GROUP

3. REPORT TITLE

An Experimental Investigation of the Unsteady Flows About Spheres and Disks

4. DESCRIPTIVE NOTES *(Type of report and inclusive dates)*

Interim Technical Report

5. AUTHOR(S) *(First name, middle initial, last name)*

Frederick W. Roos
William W. Willmarth

6. REPORT DATE December, 1968	**7a. TOTAL NO. OF PAGES** 168	**7b. NO. OF REFS** 77

8a. ~~CONTRACT OR~~ GRANT NO.

DA-ARO-D-31-124-G711

b. PROJECT NO.

5590-E

c.

d.

9a. ORIGINATOR'S REPORT NUMBER(S)

01954-1-T

9b. OTHER REPORT NO(S) *(Any other numbers that may be assigned this report)*

10. DISTRIBUTION STATEMENT

Distribution of this document is unlimited.

11. SUPPLEMENTARY NOTES

12. SPONSORING MILITARY ACTIVITY

Department of the Army
U. S. Army Research Office—Durham
Durham, North Carolina

13. ABSTRACT

The various features of unsteady three-dimensional bluff body flow fields have been studied in a towing channel filled with glycerol-water mixtures and equipped with an air bearing supported model carriage. Steady drag coefficients for the sphere and disk agreed with existing data except for the disk in the range $100 < Re_d < 1000$ where C_D is as much as 50% lower than previous results. Peak-to-peak moment coefficients developed on a disk are of the order of 0.007 for $100 < Re_d < 500$ at non-dimensional frequencies of $0.10 < fd/U < 0.14$. The sphere wake was seriously disturbed by the sting model support, however, the unsteady side force coefficient is of the order of 0.02 to 0.10 for $270 < Re_d < 560$. Flow visualization studies using hydrogen bubbles were used to relate the unsteady forces to the shedding of vorticies in the wake.

14. KEY WORDS	LINK A		LINK B		LINK C	
	ROLE	WT	ROLE	WT	ROLE	WT
Unsteady flow	7	3				
Sphere flow	7	3				
Disk flow	7	3				
Separated flow	7	3				